Measurements of Differential Rotation in Line Profiles of solar-like Stars

Dissertation
zur Erlangung des Doktorgrades
des Fachbereichs Physik
der Universität Hamburg

vorgelegt von
Ansgar Reiners

aus Friesoythe

Hamburg
2002

Gutachter der Dissertation:	Prof. J.H.M.M. Schmitt Prof. D. Reimers
Gutachter der Disputation:	Prof. J.H.M.M. Schmitt Prof. P.H. Hauschildt
Datum der Disputation:	31. 01. 2003
Vorsitzender des Prüfungsausschusses:	Dr. habil. F.-J. Zickgraf
Vorsitzender des Promotionsausschusses:	Prof. G. Huber
Dekan des Fachbereichs Physik:	Prof. F.-W. Büßer

So muß ich auch allhie von etlichen andern Meteoris und Apparentiis etwas meldung thun / sonderlich daß man jetziger zeit in der Sonnen maculas oder schwartze bloitlein eygentlich gespürt und wargenommen / wie dann solches neben mir von meinem Filio M. JOHANNE FABRICIO Medicinae studioso im Jar 1611. den 27. febru. styl. vet. durch die Holländische Brill am allererſten ist observirt worden / davon auch für außgang deß Jars zu Wittenberg einen Tractatum latinum in 4. hat lassen außgehen. Es hat aber diese Speculation hernach APELLES ANONIMUS herrlich erweittert / unnd gentzlich geschlossen, daß die Lufft mit solchen corpusculis tenebrosis erfüllet sey / weil fast täglich unter der Sonnen solche maculae in alia atq: alia forma herlauffen und gesehen werden. Was es eygentlich sey / und zu welchem end solches von GOTT erschaffen / ist schwerlich zu ergründen.

D. Fabricius, 1615, Prognosticon astrologicum

Zusammenfassung

Der Vielzahl von Phänomenen solarer und stellarer Aktivität, die auf der Sonne direkt beobachtbar sind, und die auf anderen Sternen v.a. durch Röntgen- und CaII H & K Emission nachgewiesen werden, liegt nach heutiger Auffassung ein gemeinsamer Ursprung zugrunde. Ein stellarer Dynamo am Boden der Konvektionszone transformiert kinetische in magnetische Energie und verursacht dadurch Sonnen- und Sternflecken, die magnetische Topologie, koronale Phänomene und auch den Sonnenzyklus sowie stellare Zyklen. Ein für die magnetischen Dynamos unverzichtbarer und vermutlich bestimmender Mechanismus ist differentielle Rotation. Die magnetischen Feldlinien werden durch die verursachte Scherung aufgewickelt und verstärkt, nach dieser Vorstellung ist differentielle Rotation ausschlaggebend für das Funktionieren eines stellaren Dynamos. Abhängigkeiten stellarer Aktivität von (differentieller) Rotation können uns einen tieferen Einblick in die Physik sonnenähnlicher Sterne einschließlich ihrer Zyklen geben.

Während das Rotationsgesetz der Sonne durch Beobachtungen solarer Flecken leicht bestimmt werden kann, und die differentielle Rotation der Sonne heutzutage durch Helioseismologie sogar in radialer Richtung bekannt ist, können Oberflächen anderer Sterne wegen ihrer großen Entfernung nicht räumlich aufgelöst werden. Die Bestimmung differentieller Rotation gestaltet sich hier wesentlich schwieriger. Eine Möglichkeit stellare differentielle Rotation zu messen, ist, in Linienprofilen nach Deformationen zu suchen, die auf Abweichungen von starrer Rotation schliessen lassen. Diese ohnehin schon winzigen Abweichungen sind zudem durch zusätzliche Dopplerverbreitungen v.a. durch Turbulenzen verwischt. Das Zusammenspiel von Rotation, Turbulenz, Randverdunkelung und intrinsischer Linienverbreiterung verkompliziert die Profilform, und eine zeitaufwändige Modellierung der gesamten Sternatmosphäre mußte in früheren Studien zur Suche nach stellarer differentieller Rotation ausgeführt werden.

Im ersten Teil dieser Arbeit werden die Auswirkungen differentieller Rotation auf die Form der Linienprofile detailliert untersucht. Wie schon in früheren Arbeiten werden dabei die Vorteile der Fouriertransformation genutzt. In umfangreichen Profilmodellierungen differentiell rotierender Sterne wird gezeigt, dass die Nullstellen der Fourier-transformierten Dopplerprofile eindeutig definierte Indikatoren sonnenähnlicher – also mit höherer Rotationsgeschwindigkeit am Äquator – differentieller Rotation sind. Wählt man ausschließlich diese Nullstellen zur Bestimmung differentieller Rotation, so wird die Modellierung anderer Effekte sowie der Atmosphärenstruktur überflüssig. In weiteren Modellierungen des Einflusses von Flecken und Fleckengruppen auf dieses Verfahren ergibt sich, dass das Risiko, Signaturen von Oberflächenstrukturen auf starr rotierenden Sternen mit sonnenähnlicher differentieller Rotation zu verwechseln, extrem gering ist. Die Detektion sonnenähnlicher differentieller Rotation ist damit mit der Methode der Fouriertransformation in hochaufgelösten Spektren hohen Signal-zu-Rausch Verhältnisses durchführbar.

Im zweiten Teil der Arbeit wurden Spektren von 142 Feldsternen der Spektralklassen F, G und K aufgenommen. Die projizierte Rotationsgeschwindigkeit $v \sin i$ wurde bestimmt. Mit der erreichten Datenqualität war es möglich, das Rotationsgesetz von Sternen, die schneller rotieren als $v \sin i = 12\,\mathrm{km\,s^{-1}}$, zu bestimmen. Für 84 der 142 Sterne ergab sich ein Wert von $v \sin i$, der kleiner ist als $12\,\mathrm{km\,s^{-1}}$. Von den schneller rotierenden Sternen zeigten 21 Objekte Profildeformationen aufgrund von Oberflächenstrukturen oder durch Doppelsterncharakter. Messungen des stellaren Rotationsgesetzes konnten für 32 Sterne der Spektralklassen F und G durchgeführt werden.

Zehn dieser 32 Sterne zeigen Signaturen sonnenähnlicher differentieller Rotation, die Profile der 22 anderen sind konsistent mit starrer Rotation. Die meisten differentiellen Rotatoren haben Rotationsgeschwindigkeiten von $v \sin i < 20\,\mathrm{km\,s^{-1}}$, der schnellste zeigt aber einen Wert von $v \sin i = 42\,\mathrm{km\,s^{-1}}$; differentielle Rotation ist keine Eigenschaft ausschließlich der langsamen Rotatoren. Die Zeiten, in denen der Äquator polare Regionen überrundet, liegen in der Größenordnung von zehn Tagen. Sie sind somit deutlich kleiner als der solare Wert von $\approx 130\,\mathrm{d}$, dieser ist also nicht universell für Sterne mit magnetischen Dynamos. Alle „schnellen“ ($v \sin i > 15\,\mathrm{km\,s^{-1}}$) differentiellen Rotatoren mit verfügbaren Literaturwerten ihrer Lithiumhäufigkeit sind Li-arm. Die Vorstellung eines Durchmischungsprozesses verbunden mit differentieller Rotation wird dadurch gestützt. Weitere Korrelationen zwischen differentieller Rotation und anderen stellaren Parametern werden erwartet und ihr Auftreten in der vorliegenden Stichprobe wird diskutiert.

Abstract

The plethora of activity phenomena observed on the Sun and indicated in X-ray and CaII H & K measurements on other stars are believed to be of common origin; a stellar dynamo situated at the base of the convection zone transforms kinetic into magnetic energy and causes the magnetic topology, sun- and starspots, coronal phenomena and even the solar and stellar cycles. The underlying mechanism driving a stellar dynamo is believed to be differential rotation; magnetic field lines are wound up and amplified by the latitudinal shear occuring if a star does not rotate rigidly. The amount of differential rotation in this picture would be crucial for a stellar dynamo to work and the dependencies of stellar activity on rotation and differential rotation could help us to understand the physics of solar-like stars including the solar activity cycle.

While the solar rotation law can easily be measured tracking sunspots and can nowadays even be followed in radial direction using helioseismology, surfaces of other stars cannot be spatially resolved and measurements of stellar differential rotation are much more difficult. One way measuring stellar differential rotation is to search for the subtle effects deviations from solid body rotation have on the shape of absorption line profiles. These tiny signatures of the stellar rotation law are smeared out by additional Doppler broadening due to turbulence velocity fields. Interaction of rotation, turbulence, limb darkening and intrinsic line broadening is difficult to overview, and time-consuming modelling of stellar atmospheres was carried out in previous searches for stellar differential rotation.

In the first part of this thesis the signatures of differential rotation in line profiles are studied in detail. As in previous works the advantages of Fourier transform are utilized. Exensive line profile modelling of differentially rotating stars revealed that the zeros of Fourier transformed absorption lines are well-defined tracers of solar-like differential rotation with the equator rotating faster than polar regions. Following this strategy full modelling of the stellar atmospheres becomes obsolete. Further studies on the influence of surface spots and spot groups on the profiles showed that mimicking of solar-like differential rotation by surface features only occurs in some extremely unprobable cases. The detection of stellar differential rotation with the equator faster than the pole turned out to be feasible with the Fourier transform method in a single high resolution, high signal-to-noise spectrum.

Observations of 142 field stars of spectral types F, G and K were carried out in the second part of this thesis. The projected rotational velocity $v \sin i$ was measured utilizing the zeros of the Fourier transformed spectral lines. For the acquired data quality a measurement of the rotation law was possible for stars with values of $v \sin i \geq 12\,\mathrm{km\,s^{-1}}$; for 84 of the 142 stars values of $v \sin i$ smaller than that threshold were measured. Among the faster rotators 21 stars had to be disregarded since their line profiles were dominated by surface features or the stars turned out to be binaries. Measurements of the rotation law were possible for 32 stars of spectral types F and G.

In ten of the 32 stars signatures of solar-like differential rotation were detected, 22 stars are consistent with solid body rotation. Most of the differential rotators have values of $v \sin i < 20\,\mathrm{km\,s^{-1}}$, but the fastest star showing differential rotation rotates as fast as $v \sin i = 42\,\mathrm{km\,s^{-1}}$; differential rotation is no attribute restricted to slow rotators. Lap times of the order of ten days have been detected, i.e., that the solar lap time of $\sim 130\,\mathrm{d}$ is not necessarily typical for all stars harbouring magnetic dynamos. All “fast” rotating ($v \sin i > 15\,\mathrm{km\,s^{-1}}$) differential rotators with lithium abundances available in the literature are Li-depleted. The idea of internal mixing processes due to differential rotation is supported by this result. Further correlations between differential rotation and other stellar parameters are expected and the relations indicated in the examined sample are discussed.

Contents

Chapter 1

Introduction

On 9 March 1611 Johannes Fabricius was presumably the first person observing sunspots and realizing their connection to the solar surface, even though he thought it was the 27th of February 1611 since the Gregorian calendar had not yet been adopted in East Frisia (cf. Berthold G., 1894). He and his father pointed their early telescope directly into the Sun and over the next several months they tracked spots moving across its surface interpreting the day-to-day motion as an indication of the Sun's axial rotation. The first publication on stellar rotation was Fabricius' tract *"De Maculis in Sole Observatis, et Apparente earum cum Sole Conversione Narratio"*. At the same time more famous people like Thomas Harriot, Galileo Galilei and Christoph Scheiner independently drew attention to the sunspots establishing the field of stellar physics.

Fabricius was right interpreting the moving spots on the solar surface as indicators of solar rotation. About 250 years later, Richard Carrington recognized that the Sun is not a solid body but instead is gaseous. He discovered solar differential rotation in the sense that sunspots near the equator take about 25 days for a complete rotation, but spots at higher latitudes take as long as 33 days. Another 140 years later we are today able to "look" inside the Sun using the method of helioseismology.

This thesis deals with the search for differential rotation on stars other than the Sun. Spots are discovered on many of them and let us expect that they may also rotate differentially. This introductory chapter gives a short overview about our modern view of stellar differential rotation, about expectations from theoretical models, implications to stellar activity and ways of observing stellar differential rotation.

1.1 Stellar Differential Rotation

A popular question concerning stellar rotation is "Why do stars rotate differentially?" Considering the nature of the stars – vast amounts of gaseous hydrogen and helium, held together by gravity balanced by gas pressure – one realizes, that the more natural question might rather be: "Why should a star *not* rotate differentially?"

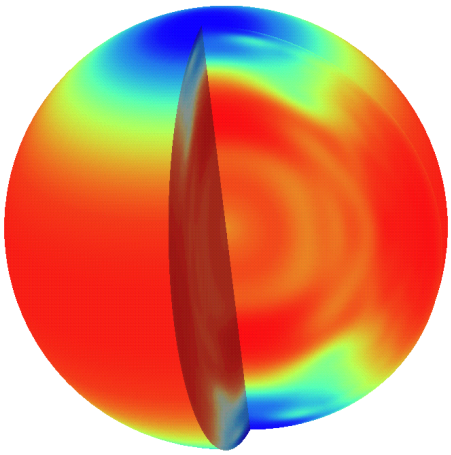

Figure 1.1: Colour-coded rotational velocity of the Sun determined with MDI on SOHO. Red colour represents faster rotation than the average flow, yellow is slower than average, and blue is slower yet.

1.1.1 The solar rotation law

Most of our knowledge about differential rotation, as most of our knowledge about stars in general, comes from the best examined star we know, the Sun. Due to our closeness to the Sun we can directly observe its surface, locate irregularities like spots or plagues on the solar surface, follow them migrating with rotation and determine the rotation period as a function of latitude.

In December 1995 the Solar & Heliospheric Observatory (SOHO) was launched, carrying a variety of instruments studying the Sun. One of those is the Michelson Doppler Imager (MDI). Helioseismology is the technique to study wave oscillations in the Sun. By studying the oscillation modes the solar rotation law was derived even in the interior. Fig. 1.1 shows the colour-coded rotation

Table 1.1: Parameters of Eq. 1.1 in deg/day

Ω_0	A	B	Reference
from Doppler Shifts			
14.049	1.492	2.605	(1)
14.07	1.78	2.68	(2)
from Sunspots			
14.368	2.69		(3)
14.37	2.86		(4)
from Magnetograms			
14.38	1.95	2.17	(5)
from Filaments			
14.42	1.40	1.33	(6)
14.48	2.16		(6)

(1) Snodgrass H.B. (2000)
(2) Pierce A.K. & LoPresto J.C. (1984)
(3) Newton H.W. & Nunn M.L. (1951)
(4) Balthasar et al. (1986)
(5) Komm et al. (1993)
(6) d'Azambuja M. & d'Azambuja L. (1948)

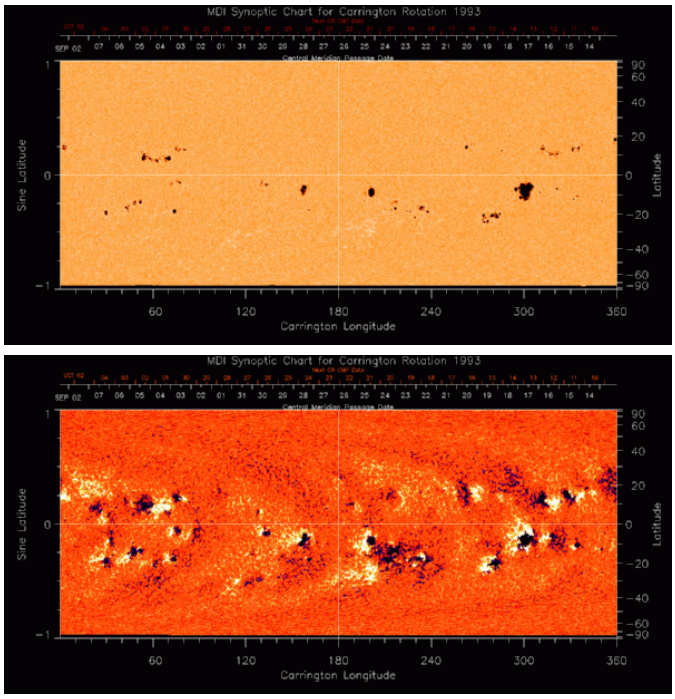

Figure 1.2: Synoptic chart of the solar surface (MDI/SOHO), x-axis is longitude, y-axis latitude. Top panel: Intensity, Lower panel: Magnetogram

of the Sun. Red colour represents faster rotation than the average flow, yellow and blue is slower than average; red regions have a rotation period of roughly 25 d while the blue regions need 33 d for a complete rotation. The solar interior is also visible, roughly speaking the inner 70% of the Sun rotate rigidly. However, there is marked differential rotation in the outer 30%, which corresponds to the solar convection zone where the Sun's energy is carried upwards by convection rather than radiation.

On the solar surface, the equator rotates faster than the poles. The latitude-dependent angular velocity of the solar surface is usually approximated by the following formula:

$$\Omega(l) = \Omega_0 - A \sin^2 l - B \sin^4 l, \qquad (1.1)$$

with Ω_0 being the equatorial angular velocity and l the latitude. In Table 1.1 various determinations of the coefficients determined from different methods are given.

As for stars other than the Sun, it is more difficult to obtain the coefficients of Eq. 1.1, since in general stellar surfaces cannot be directly resolved (cp. Sect. 1.2). No obvious reasons for the existence of stellar rotation laws different to the solar one in Eq. 1.1 exist, and this simplest assumption is usually made. Determinations of stellar rotation laws have typically larger errors due to the indirect methods and it is wise to simplify Eq. 1.1 to reduce the number of free parameters. Neglecting the $\sin^4$-term and using the parameter $\alpha = A/\Omega_0$ the solar rotation law can be written in the form

$$\Omega(l) = \Omega_0(1 - \alpha \sin^2 l) \qquad (1.2)$$

with $\alpha_\odot \approx 0.2$ as determined from sunspots. Note that positive α means solar-like differential rotation, i.e., the equator rotating faster than the polar regions, and that negative α means anti solar-like differential rotation, i.e., polar regions rotating faster than the equator.

1.1.2 Activity and Stellar Dynamos

Activity is the general term summarizing the plethora of short-lived and varying phenomena occuring on surfaces of solar-like stars. There is a rich zoo of phenomena including, e.g., *spots, faculae, spicules, mottles, fibrils, plages* etc., that all have one property in common: We do not understand the underlying physical processesses.

Activity phenomena mostly occur in groups and seem to be closely connected to stellar magnetic fields. Comparing for example the occurence of spots with magnetograms of the Sun, one finds that regions of strong activity coincide with regions of strong magnetic fields. In Fig. 1.2 the spot configuration as seen in the intensity diagram in the upper panel is compared to the magnetogram showing field strengths in the lower panel during Carrington rotation cycle 1993, i.e., between Aug 13 and Sep 09 2002. In the magnetogram the line-of-sight component of the magnetic field is shown; bright patches indicate positive (northern) polarity, dark ones represent negative (southern) polarity. The solar surface is projected with longitude on the x-axis and latitude on the y-axis. Obvi-

ously spots in the intensity diagram and regions of strong magnetic activity coincide.

Other activity phenomena are bound to the occurence of magnetic fields, too. Coronal mass ejections originate at the regions of strong magnetic activity, magnetic loops reach up into the corona and presumably play a major role in the heating of the corona. The most striking and least understood phenomenon of stellar activity is the occurence of the 22 year magnetic activity cycle comprising two sunspot cycles of 11 years each. During the beginning of a cycle, sunspots occur on latitutes up to $\sim 35^{\circ}$, at later phases the sunspots tend to form at progressively lower latitudes. During a given cycle, the majority of the leading sunspots, i.e., the sunspots leading a spot group in direction of rotation, on the northern hemisphere are of the same polarity while most of the leading spots on the southern hemisphere are of the opposite polarity. This is visible in the bottom panel of Fig. 1.2; while on the northern hemisphere the majority of the magnetic regions have positive polarity (white) on the right hand side and negative polarity (black) neighboured on the left hand side of the spot groups, the opposite is true on the southern hemisphere. After roughly 11 years a new sunspot cycle begins and most spots again occur at high latitudes but with magnetic polarities reversed.

The underlying cause of the magnetic cycle and thus the mechanism ultimately responsible for all activity phenomena is believed to be a magnetic dynamo, the mechanism transforming kinetic into magnetic energy. The most promising type for the solar one is the so-called $\alpha\omega$-dynamo. The two main mechanisms maintaining an $\alpha\omega$-dynamo are called ω-effect and α-effect.

The ω-effect

A natural starting point for the onset of a dynamo mechanism is a poloidal magnetic field, possibly a fossil one. Due to the large relaxation time of magnetic fields on microscopic scales, magnetic field lines are tightened to the stellar plasma. If a star rotates differentially, e.g., with the equator moving faster than polar regions, the shear thus also affects the field lines. The magnetic field lines, which are perpendicular to the direction of rotation, are wound up and the poloidal field becomes a toroidal (cp. Fig. 1.3). It is this mechanism that makes differential rotation the crucial ingredient in dynamo theory and in our picture of stellar activity. The stronger differential rotation is, the faster magnetic field lines wind up and poloidal field configurations become toroidal. In the solar case the equatorial regions lap the pole once in approximately 130 d. It is sometimes assumed that this lap time is characteristic for the efficiency of a stellar magnetic dynamo.

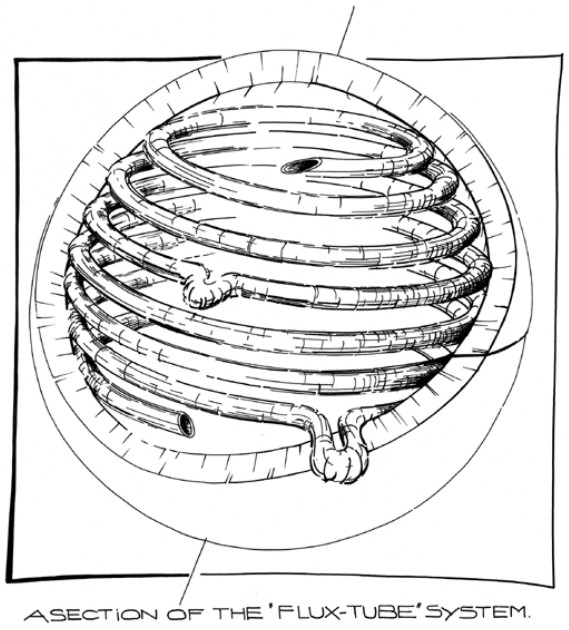

Figure 1.3: Sketch of magnetic flux tubes wound up by differential rotation. Convective upward motions bulge the flux tubes to the surface where spots occur.

The α-effect

In this context α describes the constant of proportionality between the magnetic field lines net effect of many convection cells and the resulting electric field; it must not be mistaken for the amount of differential rotation. The α-effect is responsible for the generation of a reversed poloidal field from the toroidal one, thus developing a magnetic cycle with the reversion of polarity. The details of the effect will not be considered here and can be found, e.g., in Schrijver & Zwaan (2000); Proctor & Gilbert (1994). The main mechanism believed to be responsible for the α-effect is the convective upward motion of flux tubes from deep within the Sun as sketched in Fig. 1.3. Coriolis forces twist the quenched tubes and maintain the α-effect. Where the rising flux tubes reach the surface, spot groups emerge with opposite polarity at the two hemispheres (cp. Fig. 1.2).

1.1.3 Expectations and Estimations

The interaction of convection with rotation due to Coriolis forces is the main driver of angular momentum transport towards the equator maintaining differential rotation. Magnetic field lines are stressed and warped by the motions of the plasma, but although stellar dynamos are thought to be responsible for the phenomena of stellar activity, they are not believed to seriously change the stellar rotation law. Thus magnetic fields are usually neglected

when modelling stellar differential rotation.

Models

Modelling of stellar differential rotation has to be done numerically since analytical approximations are valid only for very few special cases. Two works should be cited here.

(i) Belvedere et al. (1980) computed the latitude dependent angular velocity of main sequence stars of spectral types from F5 down to M possessing convective envelopes and thus believed to undergo differential rotation. Models of five spectral types were calculated with fixed rotation periods of the order of 2 d. The results are shown in the left panel of Fig. 1.4, where the normalized angular velocity is plotted vs. latitude. According to the models, early spectral types (F5) harbouring thin convective envelopes develop strong differential rotation. There is a minimum of differential rotation around spectral type G5 increasing again down along the main sequence towards later spectral types. All models show solar-like differential rotation with the equator rotating faster than the polar regions.

(ii) In the more recent work of Kitchatinov & Rüdiger (1999) main sequence stars of spectral type G2 and K5 are modelled with varying rotation velocities. The amount of differential rotation α is computed for stars with rotation periods between 1 d and 40 d. Their results are shown in the right panel of Fig. 1.4. The authors plotted the value of latitudinal differential rotation α vs. the rotation period. In their calculations the direction of differential rotation is solar-like, too. No case with anti solar-like differential rotation was found. The earlier spectral type possesses stronger differential rotation similar to the results from Belvedere et al. (1980). Furthermore, they found that from their model the relative amount of differential rotation diminishes with faster rotation; stars with shorter rotation periods tend to have smaller a value of α.

Lap Time

According to the calculations carried out by Kitchatinov & Rüdiger (1999) the amount of differential rotation α varies with the rotation period. As for stellar dynamos, it is often estimated that the timescale for winding up the magnetic field lines (Fig. 1.3) should be of the same order for all magnetically active stars. Following this argument the lap times

$$\frac{2\pi}{\Delta\Omega} = \frac{P}{\alpha}, \tag{1.3}$$

i.e., the time the equator needs to lap the pole on a solar-like differentially rotating star, should be of the same order as the solar one ($2\pi/\Delta\Omega_\odot \sim 130$ d).

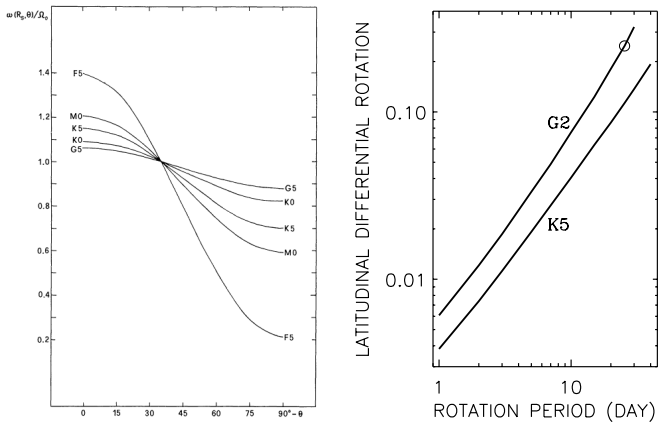

Figure 1.4: Models of differential rotation of main sequence stars. Left panel: Latitude dependent normalized angular velocities of stars of different spectral types with fixed rotation periods (Belvedere et al., 1980). Right panel: Dependence of latitudinal differential rotation (α) on rotation period for G2 and K5 dwarfs (Kitchatinov & Rüdiger, 1999). The Sun is marked with a circle.

Conversions

In theory and observations of stellar dynamos and differential rotation a variety of different variables is used. How fast a star rotates is expressed in terms of the projected rotational velocity $v \sin i$, the rotation period P or the angular velocity Ω. Differential rotation can be measured in units of the difference between the rotation periods of the pole and the equator ΔP, the difference between the respective angular velocities $\Delta\Omega$ or in terms of α. The following conversions hold:

$$\alpha = \frac{\Delta P}{P + \Delta P} \tag{1.4}$$

$$\Delta P = P\frac{\alpha}{1-\alpha} \tag{1.5}$$

$$\Delta\Omega = 2\pi\frac{\alpha}{P} \tag{1.6}$$

1.2 Observing stellar differential rotation

Differential rotation on stars other than the Sun cannot be measured directly since stellar surfaces cannot be spatially resolved. Three indirect methods introduced in this section are used to derive informations about stellar rotation laws; results of differential rotation measurements are summarized in Table 1.2.

1.2.1 Measuring Flux variations

The photometeric flux that reaches an observer can relatively easily be measured and series of observations allow

Table 1.2: Observations of stellar differential rotation

Star	Sp. Type	Period [d]	α	Reference
Direct Observations of Sunspots				
Sun	G2 V	26.9	0.2	Balthasar et al. (1986)
Photometry				
DX Leo	K0 V	5.377	0.04	Messina et al. (1999)
36 stars	F, G, K V	2.8 – 42	0.04 – 0.64	Donahue et al. (1996)
84 stars	F, G, K	0.07 – 100	0.0003 – 0.50	Hall (1991)
Doppler Imaging				
PZ Tel	K0 V (PMS)	0.95	0.01	Barnes et al. (2000)
AB Dor	K0 V	0.51	0.005	Donati & Collier Cameron (1997)
V410 Tauri	K5	1.872	0.001	Rice & Strassmeier (1996)
EI Eri	G5 IV	1.94722	0.002	Hatzes & Vogt (1992)
HR 1099	G9 V	2.83774	-0.004	Vogt et al. (1999)
UX Ari	G5 IV	6.44	-0.02	Vogt & Hatzes (1991)
HD 106 225	K0 IV	10.38	-0.02	Hatzes (1998)
Line Profiles				
some A- and F-stars, all consistent with rigid rotation				Gray (1977, 1982); Wöhl (1983)

to detect variations of the flux. If, e.g., a stellar surface is covered with spots, an observer detects a variable amount of photometric flux when observing the star since rotation changes the spot covered area an observer can see during a rotation period. Thus the rotation periods can be determined by the observation of a periodic change of photometric flux. Using photometry, rotational periods can be determined for relatively faint stars.

On the Sun spots occur on relatively high latitudes at the beginning of a sunspot cycle migrating towards the equator during the cycle. Since the equator rotates faster than higher latitudes the rotation velocity grows during the migration. Observed periods become shorter during a cycle, reflecting the combined effects of equatorward migration of the spots and differential rotation. In analogy to the solar case, changes in rotation periods on stars other than the Sun can possibly be due to spot migration and differential rotation, too.

Two major works were done determining differential rotation by measuring photometric periods; Donahue et al. (1996) measured chromosheric CaII emission while Hall (1991) used broadband photometry.

- **CaII emission**
  Donahue et al. (1996) searched for variations of photometric periods in the chromospheric CaII H & K lines. They defined the range ΔP as the difference between the maximum and the minimum observed period during seasonal rotation periods. They searched for a period dependence in ΔP and found the relation
  $$\Delta P(P_{\rm rot}) = 10^{(-1.3\pm0.06)} \cdot P_{\rm rot}^{(1.3\pm0.01)}.$$
- **Broadband photometry**
  Hall (1991) studied the periodic variation of broadband flux of late-type binary and single stars. He searched for a correlation between differential rotation in terms of α and the rotation period P. For his sample he found the relation
  $$\alpha(P_{\rm rot}) = 10^{(-2.3\pm0.06)} \cdot P_{\rm rot}^{(0.85\pm0.06)}.$$

A comparison of the results is shown in Fig. 1.5; in the left panel, ΔP is plotted vs. $P_{\rm rot}$, in the right panel $\alpha(P_{\rm rot})$ is shown. The results obtained frome CaII emission are plotted as a solid line, results from broadband photometry are shown as a dashed line, the measured points from CaII emission (+) are also shown.

Measuring differential rotation from photometry apparently yields different results when looking at different wavelength regions. It seems like the two studies provide inconsistent results. If the solar analogy holds in the stellar case, maximum latitudes where spots occur are of the order of 35°. Thus when measuring flux variations, one does not observe the whole range of rotation periods but only the "visible" part between 0° and 35°. Comparing the results from broadband and Ca II photometry may differ due to the different wavelength regions used. However, the results of both studies suggest that the amount of relative differential rotation α as well as the absolute amount

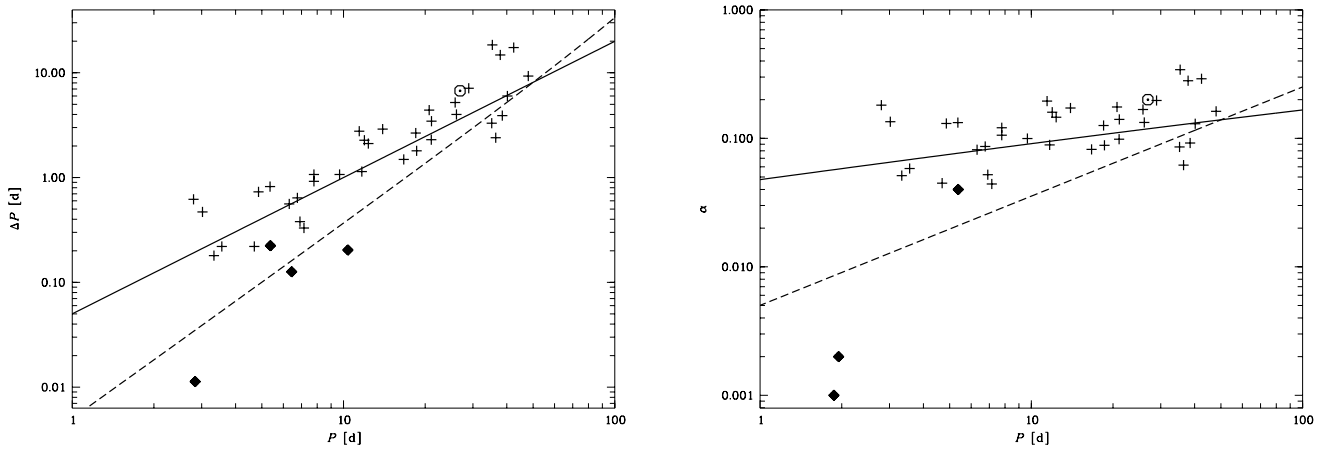

Figure 1.5: Measurements of differential rotation from Doppler imaging (⧫) and from photometry (crosses are data from Donahue et al., 1996). The solid line fits the data from Donahue et al. (1996), the dashed line is the fit to the data from Hall (1991). Left panel: ΔP vs. P; Right panel: α vs. P. The value for the Sun as determined from sunspots is also shown ($\odot$).

of ΔP are period dependent, and in particular that slower rotators have a larger value of relative differential rotation α.

1.2.2 Doppler Imaging

Another method to derive stellar differential rotation is trying to reconstruct the stellar surface at different phases. Analog to the studies on sunspots it is then possible to search for a latitude dependence of the rotational velocity.

The method used to reconstruct a stellar surface from photospheric absorption profiles is called Doppler imaging. Stellar rotation broadens the absorption profiles and due to the Doppler effect starspots appear as sinks or bumps at certain positions in the profile, migrating from the blue flank to the red flank during their migration across the stellar disk.

To derive latitude dependent rotation velocities at least two images have to be reconstructed from the observations that must cover at least one whole rotation period each. The reconstruction of the stellar surface is the delicate step in Doppler imaging due to the fact that no latitude information is contained in each single exposure of the spotted surface. Sophisticated inverse problem solutions have been developed to search for the most probable solutions and to include informations from spectroscopy, photometry, polarimetry etc. (for an overview cf., e.g., Piskunov, 1990).

Results from Doppler imaging are cited in Table 1.2. Even anti solar-like differential rotation has been claimed, but in most cases the results are consistent with rigid rotation within the error bars. It should be noted that the results depend on the width of the latitude bands correlated to search for differential migration of spot groups. Lifetime of spots and uncertainties during the surface reconstruction make interpretations difficult. Some determinations of α from Doppler imaging are shown in Fig. 1.5 (⧫). An often cited result is the differential rotation of AB Dor (Donati & Collier Cameron, 1997), a relatively fast rotating K-dwarf with an amount of differential rotation of 0.5% determined from a broad band in latitude. The idea that α diminishes with faster rotation is supported from Doppler Imaging results, mainly from the observations of AB Dor.

1.2.3 The Fourier Transform Method

Stellar rotation broadens the spectral lines from absorptions in the stellar photosphere due to the Doppler effect. Solid body rotation imprints a characteristic shape in the line profiles, and deviations from rigid rotation should on principle be directly visible in the shape of the spectral lines of rotating stars. A large advantage of this method is that there is no need for time-consuming observation series necessary for the two methods described above. But the stellar rotation law only has tiny effects on the line profiles of rotating stars. Two problems arise from this fact:

1. Other velocity fields like, e.g., turbulence or limb darkening also broaden the stellar absorption lines. Spectral signatures imprinted by differential rotation must be separated from those due to other mechanisms.

2. The data quality in terms of signal-to-noise ratio and spectral resolution has to be sufficiently high

in order to detect the small signatures of differential rotation.

The Fourier Transform Method (FTM) utilizes the Fourier transform of the absorption line profile to search for signatures of differential rotation. It is especially well suited to distinguish rotational broadening from the various broadening mechanisms occuring on a stellar surface.

Photospheric broadening mechanisms

Assuming that the different mechanisms affecting line broadening all have the same shape over the disk of the star, the net result of several broadening effects can be interpreted as a convolution (cf., e.g., Gray, 1992). The convolution of two functions is defined as

$$C(x) = \int_{-\infty}^{\infty} F(x')G(x-x')dx' = F(x) * G(x).$$

The evaluation of convolutions for spectral lines incorporating several broadening functions is thus time-consuming and difficult to overview. Transformation into Fourier domain simplifies these calculations since convolutions become multiplications in Fourier domain;

$$\begin{aligned} f(\sigma) &= \int_{-\infty}^{\infty} F(x)e^{2\pi i x\sigma}dx \\ F(x) &\rightarrow f(\sigma) \\ F(x) * G(x) &\rightarrow f(\sigma) \times g(\sigma). \end{aligned}$$

The most important broadening mechanisms of spectral lines are shown with their Fourier transforms in Fig. 1.6. In the bottom panel the result of the convolutions in data domain (left panel) and of the corresponding multiplications in Fourier domain (right panel) are given. The main constituents of photosperic line broadening are (i) intrinsic line broadening, (ii) turbulent broadening and (iii) rotational broadening.

Intrinsic line broadening

The so called intrinsic line broadening can again be interpreted as a a convolution of two mechanisms:

1. **Thermal broadening** due to the thermal motions of the stellar plasma. Thermal broadening induces a Gaussian profile with a width of

$$v_0 = \sqrt{\frac{2kT}{m}} \tag{1.7}$$

with T the temperature, k the Boltzmann constant and m the mass of the absorbing atom. For a star like the Sun one calculates $v_0 \approx 1.3$ km s^{-1} for atoms like iron.

2. **Damping effects** mainly due to natural, Stark and van der Waals damping. All effects are additive and the result can be described by a single Lorentzian profile with damping parameter $\gamma = \gamma_{\rm nat} + \gamma_{\rm Stark} + \gamma_{\rm v.d.W.}$. The values of γ are calculated numerically or determined from laboratory experiments.

Broadening due to thermal motions and damping effects can be convolved, the result is called a *Voigt* profile.

Broadening by turbulence

Turbulent motions especially in the convection zones of solar-like stars broaden the line profiles in a characteristic way. Studying the shape of line profiles an approximate model of turbulent velocity fields fitting the observations was developed (cf. Gray, 1988). The model consists of two effects, micro- and macroturbulence. For solar-like stars, microturbulence is parametrized by an isotropic Gaussian velocity field of the order of $v_{\rm micro} \approx 1$ km s^{-1}. Macroturbulence is a non isotropic "radial-tangential" flow describing an upward motion that becomes tangential when arriving at the stellar surface. The typical velocity of macroturbulence is $v_{\rm RT} \approx 6$ km s^{-1} for a solar-like star.

Since microscopic motions affect the line opacity, microscopic turbulence is often subsumed under the intrinsic profile as done in Fig. 1.6, too. It is then already accounted for when calculating the intrinsic line profiles numerically. Since the total turbulence broadening can also be described as a convolution of micro- and macroturbulence, this does not change the result of the convolutions.

Stellar Rotation

Including stellar rotation in line profile analyses means two points; (i) Including the Doppler effect due to the rotation of the star. (ii) Paying attention to the fact that a star is a 3-dimensional object with an opaque surface.

Besides the implications to radiation transfer and thus to the intrinsic line profile, the opacity of the outer stellar spheres is responsible for the limb darkening that can easily be observed, e.g., on the Sun. The solar limb appears darker than the centre since an observer normally can look deep into the layers of a stellar photosphere, but near the limb of the disk, there is only a thin surface layer in the line of sight.

The flux $\mathcal{F}(\vartheta)$ coming from a point on the stellar disk at an angular distance ϑ from the centre can be parametrized by the limb darkening parameter ϵ using

$$\mathcal{F}(\vartheta)/\mathcal{F}(0) = 1 - \epsilon + \epsilon\cos\vartheta. \tag{1.8}$$

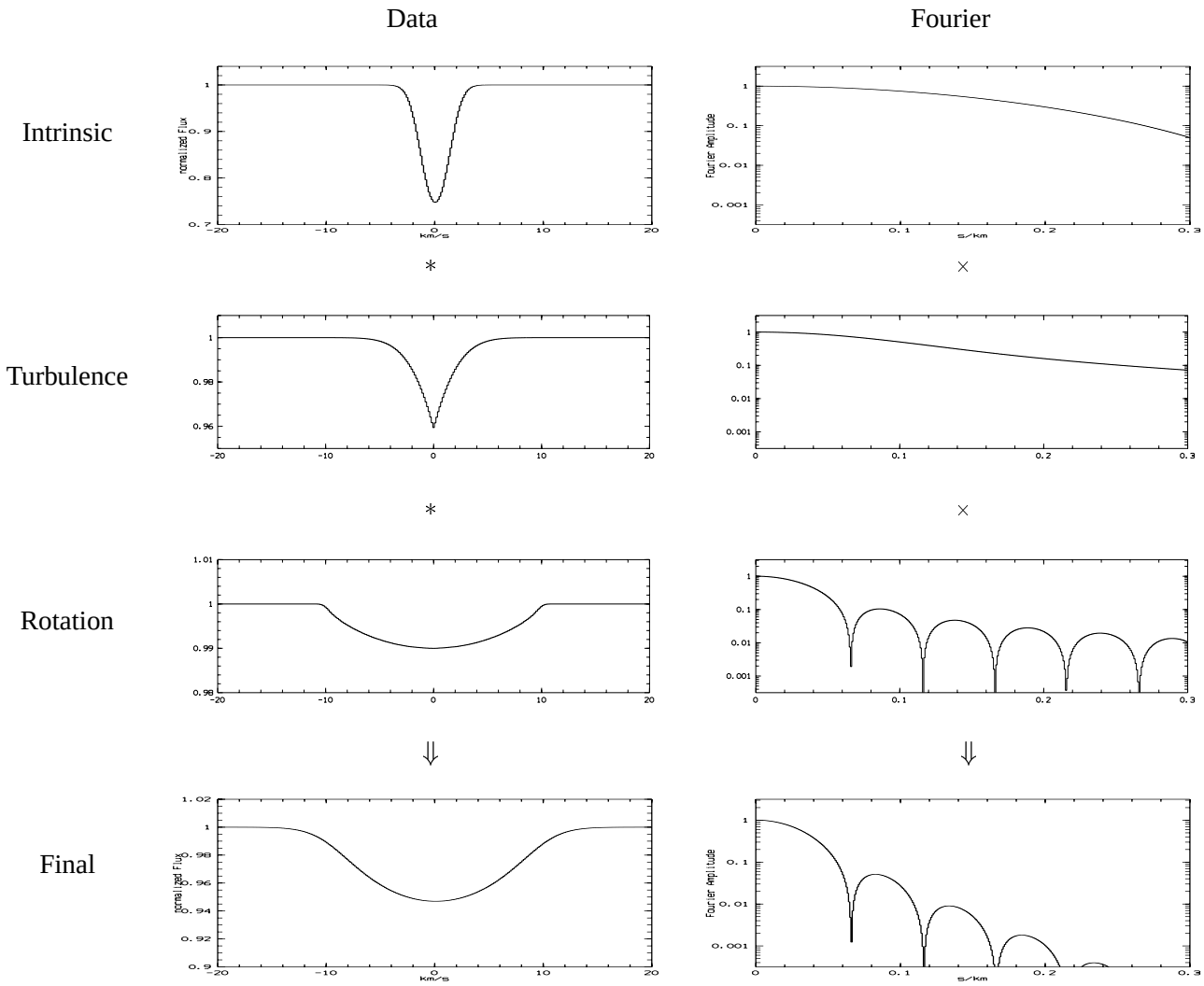

Figure 1.6: Typical line broadening profiles from the three major broadening effects; (i) intrinsic line broadening, (ii) broadening by turbulence and (iii) rotational broadening. The line profiles and their convolutions ($*$) are shown in the left panel, their Fourier transforms in the right panel. Note that convolutions become multiplications ($\times$) in Fourier domain and that especially the zeros of the Fourier transformed rotation profile are the same in the final Fourier profile.

Another critical parameter affecting the rotational line broadening is the inclination i under that the star is observed. For the observer only the projected rotational velocity $v_{\rm proj} = v_0 \sin i$ is visible. On rigidly rotating stars no difference between line profiles of stars with the same projected rotation velocities but different sets of v_0 and i exist. If on the other hand the star rotates differentially this degeneracy vanishes, each parameter becomes individually important. This problem will be discussed in Sect. 3.1.

For differentially rotating stars no analytical description of the rotational line broadening is known. To get an impression of the projected velocity fields of differentially rotating stars, isorotational curves are shown for four different configurations in Fig. 1.7. Rotational broadening profiles are calculated numerically incorporating the effect of limb darkening and the correct projections of the velocity fields.

The advantages of multiplication

Analyzing spectral lines observers often try to fit numerical models to observed data. Following that strategy it should make no difference if a goodness of fit parameter χ^2 is calculated in data or in Fourier domain. But one favourable difference between data and Fourier space is that convolutions in data space become multiplications in Fourier space, and the latter are much easier to handle. For the analysis of differential rotation this simple fact is the main advantage of Fourier domain, since specifically zeros of any involved function do appear in the final result of the multiplications.

In Fig. 1.6 it can be seen that the rotation profile in Fourier domain is the only function involved having zero positions. These zeros also appear in the final profile, which is the Fourier transform of the observed line profile, and can thus be easily observed. Under the as-

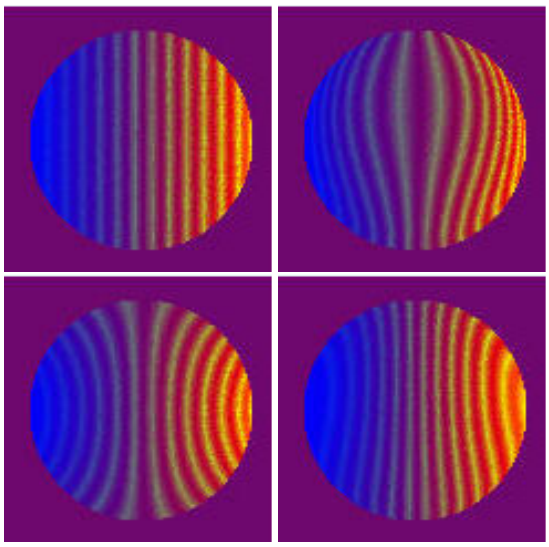

Figure 1.7: Projected rotation velocities of differential rotators seen under different inclination angles. Blue color means motion towards the observer and Doppler shift towards shorter wavelengths, red color the opposite. Yellow lines are curves of isorotation. (Upper left: $i = 90°, \alpha = 0.0$, upper right: $i = 90°, \alpha = 0.6$, lower left: $i = 20°, \alpha = 0.6$, lower right: $i = 20°, \alpha = -0.3$)

sumption that no additional zeros are introduced by other mechanisms, i.e., that especially all other velocity fields are of significantly smaller amplitude than rotation, it is thus possible to observe the zeros of the rotation profile directly in the Fourier transform of the observed spectral line. No time-consuming modelling has to be done using this technique.

The characteristics of the rotation profile's Fourier transform are studied in detail in Sect. 3.1. It is shown there that the Fourier transform's zeros are indeed excellent tracers of solar-like differential rotation.

Some words about data quality

Working in Fourier space it is relatively easy to specify the quality requirements observed spectra must fulfill. The necessary resolution R and the signal-to-noise ratio S/N can directly be estimated from the Fourier transform. As shown in Sect. 3.1 the first and second Fourier transform's zero positions q_1 and q_2 must be measured in order to determine the stellar rotation law. The important parameters are shown in Fig. 1.8. The spectral resolution R determines the Nyquist frequency $\sigma_{\rm N}$ limiting the Fourier transform to higher frequencies on the x-axis. The signal-to-noise ratio S/N translates into a noise level S_σ in Fourier domain limiting the Fourier transform to lower amplitudes on the y-axis. Nyquist frequency $\sigma_{\rm N}$ and noise level S_σ can be written as

$$\begin{aligned} \sigma_{\rm N} &= \frac{1}{2\Delta x} = \frac{R}{2c} \\ \text{and} \qquad S_\sigma &= S_x \Delta x \sqrt{N} \propto \frac{1}{S/N\sqrt{R}} \end{aligned}$$

with Δx a spectral resolution element in data space, S_x the standard deviation of the data, N the number of measured points and c the speed of light. A detailed calculation of the required signal-to-noise ratio and spectral resolution for the instruments and stars used in this work is given in Sect. 4.2.2.

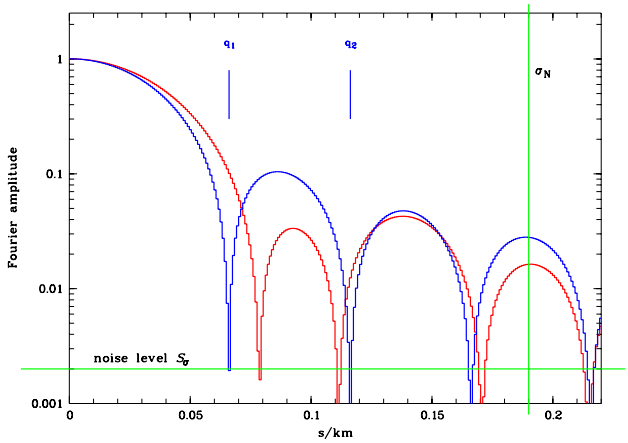

Figure 1.8: Typical rotational broadening profiles of a rigid rotator (blue) and a differential rotator (red) in Fourier space. The first two zeros q_1 and q_2 are measured to determine α (cf. Sect. 3.1). Noise level S_σ and Nyquist frequency σ_N are indicated.

Physical Least Squares Deconvolution

In order to detect the tiny effects of differential rotation in spectral lines especially the signal-to-noise ratio of the data has to be extremely high. One advantage of rotational broadening is that it affects all spctral lines in the same characteristic way. Thus the signal-to-noise ratio can enormously be enhanced by using the broadening information contained in as many spectral lines as possible. One way of doing this is to deconvolve the rotational broadening profile from the observed (final) spectrum using a template assumed to be the unbroadened stellar spectrum. This method is called Least Square Deconvolution (LSD), mathematical details can be found in Cameron (2000).

Using LSD on line profiles from slowly rotating stars, the dependence of thermal broadening on the atomic weight of the absorbing atoms becomes an important factor. According to Eq. 1.7 the atomic weight m of the absorber significantly varies the width of the spectral lines.

For slowly rotating stars it is thus essential to broaden the lines of the spectral template according to the specific weight of the absorbing atom before deconvolving the broadening profile. This physical treatment of thermal broadening is accounted for in the template, being the main difference between the method used, e.g, in Doppler Imaging (Donati & Collier Cameron, 1997; Barnes et al., 2000, etc.) and the Physical Least Squares Deconvolution (PLSD) applied in this work; PLSD is described in Sects. 5.1.2 and 7.1.3.

1.3 Outline

In Table 1.2 recent measurements of stellar differential rotation are presented. The results from photometry come from a large number of stars, but since photometric variations might be due to mechanisms other than stellar rotation, for some of them a number of alternative explanations seem plausible. The results from different works do even yield different results and do not provide a clear overall picture.

Results from Doppler imaging are mainly consistent with rigid rotation within the error bars, probably one of the most promising detections of differential rotation is the case of AB Dor (Donati & Collier Cameron, 1997). However, Doppler Imaging is also affected by some problems, as for example the lifetime of the spots and the ambiguity of the surface reconstruction. The small number of differential rotation measurements from Doppler imaging does neither allow general conclusions about stellar differential rotation.

All observations using the shape of line profiles in the past were consistent with rigid rotation, too. This may mainly be due to the limited data quality supplied by the instrument generation used in those studies. On the other hand it was not exactly known what to look for because numerical simulations about the effects of stellar differential rotation on line profiles could not be studied in the required detail.

Thus it can be said that for no star other than the Sun an unambiguous detection of differential rotation was made. In the following chapters the publications that arose during a new effort of detecting signatures of differential rotation in stellar absorption profiles are presented. With spectra from a first observing night collected with the Coudé Echelle Spectrograph (CES) at the 3.6m telescope at La Silla / Chile in October 2000 the consistency of detecting deviations from rigid rotation in absorption profiles and searching for differential rotation in Fourier space was tested. Using a multi-dimensional χ^2 -fit the atmospheric structure of several stars was directly modelled. It was confirmed that searching for differential rotation using FTM provides the same results as doing time-consuming and complicated atmospheric modelling. Furthermore it was possible to detect signatures of differential rotation in ψ Cap in two absorption lines (Chapter 2).

In Chapter 3 a feasibility study on how differential rotation can be searched for in stellar absorption profiles is given. A parameter study using numerical models was carried out to analyze the effects of different parameters like rotational velocity v, inclination i and limb darkening ϵ on the measurements of the value of differential rotation α.

When observing solar-like stars, the question about an influence of starspots arises immediately. In Chapter 4 a study is presented on how active regions and configurations of starspots can affect the measurements of differential rotation, and especially if differential rotation can be mimicked by surface features on a rigidly rotating star.

Supported by the success of the first observing run, seven more observing nights at the CES were granted to the project in October 2001 and April 2002. In total, 142 stars have been examined during the project. The results from the study are shown in Chapters 5, 6 and 7. In Chapter 5 the focus lies on direct evidences of differential rotation visible even in the data domain; three stars turned out to have an amount of differential rotation as strong as $\alpha \sim 0.4$ and the signatures of differential rotation are visible even in data domain. In Chapter 6 the results of the study with evidence for a correlation between differential rotation and lithium depletion are presented. This result supports the idea of a mixing mechanism working in Li-depleted fast rotators and reveal a physical correlation between the measured value of differential rotation α and the independent parameter of Li abundance. Chapter 7 is a comprehensive summary of methods and results developed and achieved during the project. The measured amounts of stellar differential rotation are correlated to more stellar parameters governing stellar activity and dynamo processes. The results are also compared to the measurements achieved in other studies. Finally, the results are summarized in Chapter 8 and an outlook to future prospects is given.

References

d'Azambuja M., and d'Azambuja L., 1948, Ann. Obs. Paris, Section Meudon VI, Fasc. VII

Balthasar H., Vázques M., and Wöhl H., 1986, A&A, 185, 87

Barnes J.R., Collier Cameron A., James D.J., and Donati J.-F., 2000, MNRAS 314, 162

Belvedere G., Paternò L., and Stix M., 1980, A&A, 91, 328

Berthold G., 1894, “Der Magister Johann Fabricius und die Sonnenflecken”, Verlag von Veit & Comp., Leipzig

Cameron A.C., 2000, Spot mapping in cool stars, Proceedings of Astro-Tomography: An International Workshop on Indirect Imaging, ed. H. Boffin, Danny Steeghs, Jan Guypers. Lecture Notes in Physics (2000), in press

Donahue R.A., Saar S.H., and Baliunas S.L., 1996, ApJ, 466, 384

Donati J.-F., Cameron A., 1997, MNRAS, 291, 1

Gray D.F., 1977, ApJ, 211, 198

Gray D.F., 1982, ApJ, 258, 201

Gray D.F., 1988, Lectures on spectral-line analysis: F, G and K stars, The Publisher, Arva

Gray D.F., 1992, The observation and analysis of stellar photospheres, Cambridge Univ. Press, Cambridge

Hall, D.S., 1991, in The Sun and Cool stars, activity, magnetism, dynamos, eds. I. Tuominen, D. Moss, and G. Rüdiger, Springer Verlag, New York, p.353

Hatzes A.P., and Vogt S.S., 1992 MNRAS, 258, 387

Hatzes A.P., 1998, A&A, 330, 541

Kitchatinov L.L., and Rüdiger G., 1999, A&A, 344, 911

Komm R.W., Howard R.F., and Harvey J.W., 1993, Sol. Phys., 143, 19

Messina S., Guinan E.F., Lanza A.F., and Armbruster C., 1999, A&A, 347, 249

Newton H.W., and Nunn M.L., 1951, MNRAS, 111, 413

Pierce A.K., and LoPresto J.C., 1984, Sol. Phys., 93, 155

Piskunov N.E., 1991, in The Sun and Cool Stars: activity, magnetism, dynamos, ed. I. Tuominen, D. Moss, G. Rüdiger, IAU Coll. 130, Springer Verlag, Berlin

Proctor M.R.E., and Gilbert A.D., 1994, Lectures on Solar and Planetary Dynamos, Cambridge University Press

Rice J.B., and Strassmeier K.G., 1996, A&A, 316, 164

Snodgrass H.B., 2000, Sol. Phys., 94, 13

Schrijver C.J., and Zwaan C., 2000, Solar and Stellar Magnetic Activity, Cambridge University Press

Vogt, S.S., and Hatzes A.P., 1991, in The Sun and Cool stars, activity, magnetism, dynamos, eds. I. Tuominen, D. Moss, and G. Rüdiger, Springer Verlag, New York, p.297

Vogt S.S., Hatzes A.P., and Misch A.A., 1999, ApJSS, 121, 547

Wöhl H., 1983, in Solar and Stellar Magnetic Fields: Origin and Coronal Effects, ed. J.O. Stenflo, IAU Symp. 102, Reidel Dordrecht, p. 155

Chapter 2

Detection of differential rotation in ψ Cap with profile analysis

2.1 A. Reiners, J.H.M.M. Schmitt, and M. Kürster
Astronomy & Astrophysics, 376, L13 (2001)

A&A 376, L13–L16 (2001)
DOI: 10.1051/0004-6361:20011023

Astronomy & Astrophysics

Detection of differential rotation in ψ Cap with profile analysis⋆

A. Reiners[1], J. H. M. M. Schmitt[1], and M. Kürster[2]

[1] Hamburger Sternwarte, Universität Hamburg, Gojenbergsweg 112, 21029 Hamburg, Germany
[2] European Southern Observatory, Casilla 19001, Vitacura, Santiago 19, Chile

Received 8 June 2001 / Accepted 16 July 2001

Abstract. We report detection of differential rotation on the F5 dwarf ψ Cap using line profile analysis. The Fourier transform of both Fe I λ5775 and Si I λ5772 are used to obtain a projected rotational velocity of $v \sin i = 42 \pm 1\,\mathrm{km\,s^{-1}}$. Modelling of the Fourier transformed profiles shows that the combined effects of equatorial velocity, inclination and differential rotation dominate the line profile while limb darkening and turbulence velocities have only minor effects. Rigid rotation is shown to be inconsistent with the measured profiles. Modelling the line profiles analogous to solar differential rotation we find a differential rotation parameter of $\alpha = 0.15 \pm 0.1$ ($15 \pm 10\%$) comparable to the solar case. To our knowledge this is the first successful measurement of differential rotation through line profile analysis.

Key words. methods: data analysis – stars: activity – stars: individual: ψ Cap – stars: late-type – stars: rotation

1. Introduction

According to the standard paradigm of stellar activity differential rotation is a central ingredient for the magnetic dynamo presumed to underlie all activity phenomena. In a turbulent convection zone differential rotation is expected to be a central element of stellar activity. The interaction of rotation and convection naturally produces deviations from rigid rotation. One example for this effect is the Sun, whose equator rotates ∼20% faster than higher latitudes (e.g. Lang 1992). Direct predictions of the dependence of differential rotation on rotational velocity and spectral type have been made (e.g. Belvedere et al. 1980; Kitchatinov & Rüdiger 1999). Observations suggest a strong correlation between rotation and activity in late-type stars with many pieces of evidence summarized as "rotation-activity connection" (Hempelmann et al. 1995; Messina et al. 2001).

However, measurements of differential rotation among stars are either complicated or time-consuming or both. One method to determine differential rotation is to examine spectral line shapes. Subtle differences exist between the line profile of a rigidly rotating star and that of a differentially rotating star, because the underlying flow fields are different. Although significant differences between the two cases are predicted, all previous attempts to measure differential rotation through line profiles alone remained unsuccessful and yielded results consistent with rigid rotation (e.g. Gray 1982; Dravins et al. 1990; Groot et al. 1996). At any rate, for a successful measurement one needs high spectral resolution and high signal to noise. With the Very Long Camera (VLC) of the Coudé Echelle Spectrograph (CES) at ESO's 3.6 m telescope an instrumental setup satisfying these requirements is available. In this letter we report the detection of differential rotation in the F5 dwarf ψ Cap, to our knowledge the first successful measurement of differential rotation through line profiles.

2. Data

ψ Cap (HD 197 692, F5 V, $V_{\mathrm{mag}} = 4.13$, $v \sin i = 40\,\mathrm{km\,s^{-1}}$; Uesugi et al. 1982) is the fastest rotator in a set of solar-like stars in the solar neighbourhood we observed on October 13, 2000 at ESO's 3.6 m telescope (La Silla). The spectral resolution achieved with the CES/VLC setup was $R = 235\,000$ ($\sim 1.28\,\mathrm{km\,s^{-1}}$). Three consecutive exposures of ψ Cap of 270 s each covering the wavelength range between 5770–5810 Å were taken. The signal to noise ratio of the extracted spectrum is $S/N \sim 800$ per pixel with proper flat fielding and removal of interference pattern (cf. Kürster 2001 Sect. 6).

We concentrate our analysis on Fourier transforms of well isolated lines (Fe I λ5775 and Si I λ5772), for which continuum placement because of line blending is not a problem even for large $v \sin i$ values. The signal to noise ratio of our data is high enough to show the crucial features in the Fourier transform already from a single line.

Send offprint requests to: A. Reiners,
e-mail: areiners@hs.uni-hamburg.de

⋆ Based on observations collected at the European Southern Observatory, La Silla (65.L-0101).

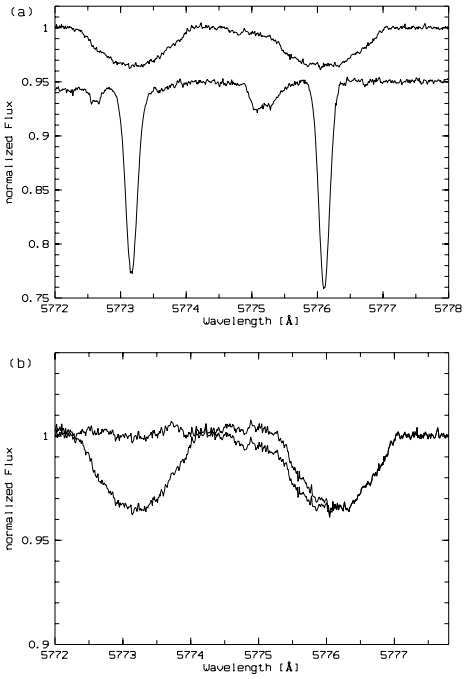

Fig. 1. a) Fe I λ5775 (right) and Si I λ5772 (left) lines of ψ Cap (upper line) and ι Psc (lower line; shifted along y-axis). **b)** Original and modified line profiles of ψ Cap (see text).

Still, in Fe I λ5775 a small blend occurs from a neighbouring set of weak lines $\sim$0.8 Å apart, the influence of which on differential rotation determination is not clear. During our observing run a spectrum of the slow rotator ι Psc (HD 222 368; F7 V) was taken. In Fig. 1a both spectra are shown, with the profile of ι Psc shifted according to its relative radial velocity. Deblending of Fe I λ5775 was accomplished by, first, removing the line in the spectrum of ι Psc "by hand", broadening this template with $v_{\rm rot} = 40\,{\rm km\,s^{-1}}$ and subtracting it from the ψ Cap spectrum. In Fig. 1b the recorded spectrum as well as the modified spectrum of ψ Cap are shown. Obviously, the Si I λ5772 equivalent widths of ψ Cap and ι Psc are the same, since it has been successfully removed (cf. Fig. 1b). The Fe I λ5775 line appears symmetric, thus we think that deblending was successful.

3. Method of analysis

Absorption line profiles are influenced by a number of different effects. An absorption line profile at any point on the star is determined by temperature, gravity, element abundances and atomic parameters. This "intrinsic" profile is Doppler broadened by velocity fields. Many efforts have been undertaken to distinguish these velocity fields, one of them being the stellar rotation (see Gray 1988 and references therein). In addition to the projected rotational velocity of the star, radial-tangential macro- and isotropic microturbulence (denoted with $\zeta_{\rm RT}$ and ξ resp.) turned out to be a reasonable parameterization of stellar atmospheric velocity fields. These parameterizations assume that Doppler broadenings can be treated as convolutions; and that the "intrinsic" profiles are identical over the apparent stellar disk. For fast rotators ($v \sin i > 30\,{\rm km\,s^{-1}}$) and stationary atmospheres rotational broadening dominates and no complications occur with this assumption.

Interpreting the observed data profile $D(\lambda)$ as a a multiple convolution (denoted by $*$) between the intrinsic profile $F(\lambda)$ (including microturbulence broadening), the rotational broadening profile $G(\lambda)$, the instrumental profile $I(\lambda)$ and the macroturbulence profile $M(\lambda)$, $D(\lambda)$ can be written as

$$D(\lambda) = F(\lambda) * G(\lambda) * I(\lambda) * M(\lambda). \quad (1)$$

We calculated $F(\lambda)$ using the packages Atlas9 (Kurucz 1979, 1993) and Bht (Baschek et al. 1966). Atomic damping coefficients obtained from VALD (Kupka et al. 1999; Kurucz 1994) were included in the profile calculations; we chose solar metallicity and for the velocity dispersion of the opacity distribution function in Atlas9 we used $1.0\,{\rm km\,s^{-1}}$. The temperature has been set to $T_{\rm eff} = 6500\,{\rm K}$ (Blackwell & Lynas-Gray 1998). To calculate $G(\lambda)$ a modified version of a package developed and described by Townsend (1997) is used. The surface integration is carried out over about 25 500 visible surface elements. The adopted limb-darkening law is given by

$$I(\cos\theta) = I_0\,(1 - \epsilon + \epsilon\cos\theta), \quad (2)$$

with θ denoting the angle between the surface element normal and the observer's line of sight and ϵ the limb darkening coefficient. We parametrize the differential rotation law through

$$\omega(l) = \omega_0 - \omega_1 \sin^2 l \quad (3)$$

with l being the latitude. Specifically, differential rotation is expressed in terms of $\alpha = \omega_1/\omega_0$. The differential rotation law (Eq. (3)) is adopted from the solar case, where $\alpha_\odot = 0.20$; a more general approach would expand $\omega(l)$ in terms of orthogonal polynomials. The instrumental profile $I(\lambda)$ has been determined from the shapes of calibration lamp lines, a correction for thermal broadening according to the lamp temperature of 120 °C was applied. The macroturbulence broadening function $M(\lambda)$ is adopted from Gray (1992).

The contributions of different velocity fields are difficult to separate especially in the wavelength domain. In the Fourier domain convolutions become multiplications which are much easier to handle; the advantages of Fourier domain are discussed in detail by Gray (1992). In the Fourier domain Eq. (1) becomes

$$d(\sigma) = f(\sigma) \cdot g(\sigma) \cdot i(\sigma) \cdot m(\sigma). \quad (4)$$

The Fourier frequency σ is expressed in cycles/(km s^{-1}) = s km^{-1}. Noise in Fourier domain can be expressed as $S_\sigma = S_\lambda\,\Delta\lambda\,N^{\frac{1}{2}}$ (Gray 1992), with S_λ being

data noise and $\Delta\lambda$ step size in the wavelength domain, N is the number of data points. The Fourier transform of a real, symmetric profile yields a real function in the Fourier domain. Investigations of imaginary transforms of asymmetric lines show that these are no reliable tracers of profile properties (Gray 1980). We created a symmetric profile by mirroring the absorption profile at it's center; the achieved Fourier transform turned out to be stable against small variations of the center position. Rotational broadening, which dominates the line broadening in the case of ψ Cap, yields symmetric profiles. Asymmetries due to convection are believed to be of the order $v < 1\,\mathrm{km\,s^{-1}}$. In Fourier space this is $\sigma > 1\,\mathrm{s\,km^{-1}}$ while our analysis focuses on $\sigma < 0.04\,\mathrm{s\,km^{-1}}$. In the case of Fe I λ5775 an asymmetry may occur due to imperfect deblending, for Si I λ5772 no mechanism should contribute asymmetries of this order.

The Fourier transformed observed line profile was compared with a Fourier transformed model profile via a χ^2 test. Within our adopted modelling approach the following six fit parameters determine the model profiles: rotational velocity (v), inclination angle (i), differential rotation (α), limb darkening (ϵ), macro- (ζ_{RT}) and microturbulence (ξ). The χ^2-calculations have always been carried out directly on $d(\sigma)$. No further corrections have been applied to the data to avoid complications with amplified noise. Bruning (1984) pointed out that the convolution method induces systematic errors due to incorrectly estimated line depths especially in slow rotators. Our study is not focused on reproducing equivalent widths, which can be tuned e.g. by element abundances. The main goal is to reproduce the line shapes. Although we do not examine slow rotators in this study, normalized transformed profiles were used, that is, Fourier transformed profiles have been scaled to unity at $\sigma = 0$.

4. Results and discussion

After a rough determination of $v \sin i$ a grid calculation in the six fit parameters was carried out. As to our model parameterization we note that this description contains parameters whose physics is poorly understood, i.e., the micro- and macroturbulence. We thus use χ^2 only as a relative parameter and not as an absolute criterion as to whether a model is acceptable or not; χ^2_{n} denotes the goodness of fit relative to the best fit, for which $\chi^2_{\mathrm{n}} = 1$ is set. For the actual grid we chose the parameter ranges of ϵ (0.4–0.8), ζ_{RT} (4.0–7.0) $\mathrm{km\,s^{-1}}$ and ξ (1.0–2.5) $\mathrm{km\,s^{-1}}$. The rotation velocity was limited to $v < 120\,\mathrm{km\,s^{-1}}$ ($i > 20°$).

Goodness of fit calculations have been carried out on Fe I λ5775 and Si I λ5772; both lines show identical results. In the following we show only the results for Fe I λ5775.

In Fig. 2 we plot the resulting χ^2_{n} as a function of the differential rotation parameter α; for each fixed value of α, we plot the χ^2_{n} values obtained by varying all other model parameters. Clearly, a well defined lower envelope curve exists with a minimum at $\alpha = 0.20$. The best fits for differential rotation (here $\alpha = 0.20$; $\chi^2_{\mathrm{n}} = 1$, Model 1) and rigid rotation ($\alpha = 0.0$, $\chi^2_{\mathrm{n}} = 7.9$, Model 2) are marked by full squares; all parameters are shown in Table 1.

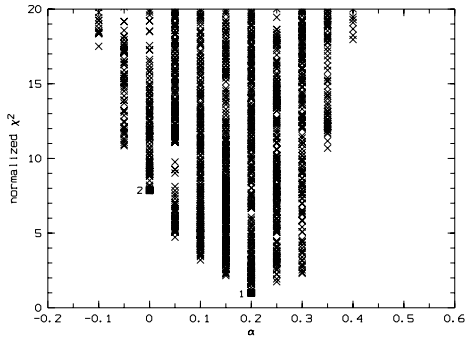

Fig. 2. Normalized χ^2 vs. α for calculated models with various values of $v, i, \epsilon, \zeta_{\mathrm{RT}}$ and ξ (see text); each cross represents one set of parameters. Best fits of all models (1) and for rigid rotation (2) are denoted by full squares.

Table 1. Parameters of best fitting models for rigid and differential rotation.

Model	v	i	α	ϵ	ζ_{RT}	ξ	χ^2_{n}
1	$43\frac{\mathrm{km}}{\mathrm{s}}$	80°	0.20	0.6	$4.0\frac{\mathrm{km}}{\mathrm{s}}$	$1.0\frac{\mathrm{km}}{\mathrm{s}}$	1.0
2	$48\frac{\mathrm{km}}{\mathrm{s}}$	60°	0.00	0.8	$7.0\frac{\mathrm{km}}{\mathrm{s}}$	$2.5\frac{\mathrm{km}}{\mathrm{s}}$	7.9

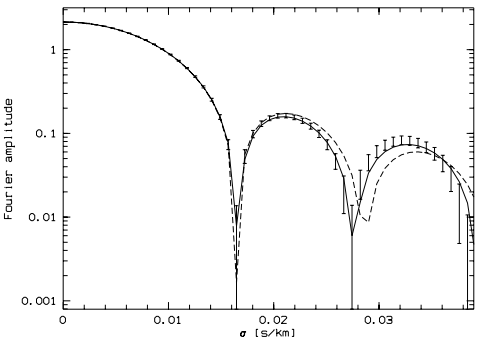

Fig. 3. The Fourier transformed data indicated by error bars. Best fits for differential rotation ($\alpha = 0.20$; full line, Model 1) and rigid rotation ($\alpha = 0.0$; dashed line, Model 2) are shown. See Table 1 for parameters.

In Fig. 3 we plot the corresponding profiles in the Fourier domain; obviously, Model 1 provides a much better fit than Model 2, which is not an adequate description of our data. While no statistical uncertainties can be given on our χ^2_{n}-values, Fig. 3 shows χ^2_{n}-values of 7.9 to be clearly unacceptable.

Inspection of the calculated χ^2_{n}-grid shows that the parameters $\epsilon, \zeta_{\mathrm{RT}}$ and ξ produce only second order effects; the fits are driven by the chosen values of v, i and α,

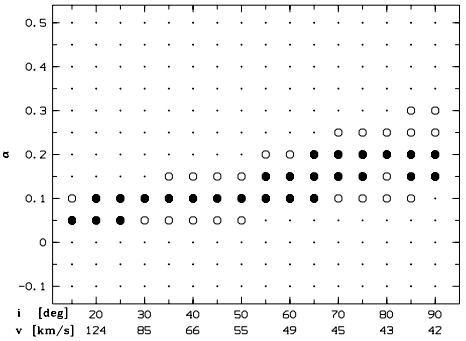

Fig. 4. $\chi^2_{\rm n}$ of fits to Fe I λ5775 with $41.3\,{\rm km\,s^{-1}} < v \sin i < 43.3\,{\rm km\,s^{-1}}$, $\epsilon = 0.6$, $\zeta_{\rm RT} = 6.0\,{\rm km\,s^{-1}}$ and $\xi = 1.0\,{\rm km\,s^{-1}}$ in the $\alpha - i$ (v) plane: $\chi^2_{\rm n} < 5$ (•); $5 < \chi^2_{\rm n} < 10$ (○); $\chi^2_{\rm n} > 10$ (·).

and we cannot determine all model parameters independently. Therefore, we fixed the values $\epsilon = 0.6$ (Carbon & Gingerich 1969), $\zeta_{\rm RT} = 6.0\,{\rm km\,s^{-1}}$ and $\xi = 1.0\,{\rm km\,s^{-1}}$ (Gray 1988, and references therein). We emphasize that our subsequent findings do not require these specific parameter settings, and that the influences of ϵ, $\zeta_{\rm RT}$ and ξ are too small to revoke the effects of α, v and i. For the given parameters the best fit value for $v \sin i$ is $42.3\,{\rm km\,s^{-1}}$. We estimate the total systematic errors to be $\approx 1\,{\rm km\,s^{-1}}$. Models outside the range $42.3 \pm 1\,{\rm km\,s^{-1}}$ all have $\chi^2_{\rm n} > 5$.

Theoretical investigations of the line profile behaviour in Fourier space show that with differential rotation $\alpha \neq 0$ the inclination i becomes important (e.g. Bruning 1981). For comparable values of $v \sin i$ the best fit values of α and i are correlated. In Fig. 4 we consider calculated models with fixed ϵ, $\zeta_{\rm RT}$, ξ, $v \sin i$ between 41.3 and $43.3\,{\rm km\,s^{-1}}$ and varying α, v and i. Three groups of models are distinguished; $\chi^2_{\rm n} < 5$ (•), $5 < \chi^2_{\rm n} < 10$ (○) and $\chi^2_{\rm n} > 10$ (·). A well defined area of reliable fits in the $\alpha - i$ plot emerges. All fits with $\chi^2_{\rm n} < 10$ show $\alpha > 0.0$. Although we used no absolute criterion on wheter a model is acceptable, the estimation of systematic errors and a comparison with Fig. 3 shows that the threshold $\chi^2_{\rm n} < 10$ is a rather high choice.

A variety of combinations of equatorial velocity and inclination seems possible for $\alpha > 0$. A smaller differential effect is preferred for faster rotating models. For extremely high values of $v > 200\,{\rm km\,s^{-1}}$ rigid rotation might be argued, but such velocities seem unlikely given the age of ψ Cap of $\sim 2 \times 10^9$ a (Lachaume et al. 1999). Even the minimum rotational velocity of $42\,{\rm km\,s^{-1}}$ seems uncommonly high. From Fig. 4 we derive $\alpha = 0.15 \pm 0.1$. The identical result was found for Si I λ5772, where the same procedure was applied.

To summarize differential rotation has been established for the rapid rotator ψ Cap independently from two absorption line profiles. While ψ Cap rotates at least 20 times faster than the Sun, it's differential rotation is comparable to the solar value, but not with the differential rotation patterns determined from Doppler images of the fast rotators AB Dor (Donati & Collier Cameron 1997) and PZ Tel (Barnes et al. 2000). As direct predictions for a F5 dwarf have not been calculated by Kitchatinov & Rüdiger (1999) and the rotation period of ψ Cap is only poorly determined, the consistency of our result and the model is not clear. Assuming $R = 1.2\,R_\odot$ and $i = 90°$, we find for ψ Cap the rotation law $\omega(l) = 4.38 - 0.66 \sin^2 l\,{\rm rad/d}$; ψ Cap does not rotate like a rigid body as suggested for AB Dor and PZ Tel. To compare theory and observations more detailed predictions especially on spectral type dependence and a greater sample of direct observations are needed. In particular verification of the differential rotation results of line profile analysis and Doppler imaging for the same star will be instructive.

Acknowledgements. A.R. acknowledges financial support from Deutsche Forschungsgemeinschaft DFG-SCHM 1032/10-1.

References

Barnes, J. R., Collier Cameron, A., James, D. J., & Donati, J.-F. 2000, MNRAS, 314, 162
Baschek, B., Holweger, H., & Traving, G. 1966, Abhandl. Hamburger Sternwarte, 8, 26
Belvedere, G., Paternò, L., & Stix, M. 1980, A&A, 88, 240
Blackwell, D. E., & Lynas-Gray, A. E. 1998, A&AS, 129, 505B
Bruning, D. H. 1981, ApJ, 248, 274
Bruning, D. H. 1984, ApJ, 281, 830
Carbon, D. F., & Gingerich, O. 1969, in Theory and Observation of normal stellar atmospheres, ed. O. Gingerich (MIT Press)
Donati, J.-F., & Collier Cameron, A. 1997, MNRAS, 291, 1
Dravins, D., Lindegren, L., & Torkelsson, U. 1990, A&A, 237, 137
Gray, D. F. 1980, ApJ, 235, 508
Gray, D. F. 1982, ApJ, 258, 201
Gray, D. F. 1988, Lectures on spectral-line analysis: F, G and K stars (The Publisher, Arva)
Gray, D. F. 1992, The observation and analysis of stellar photospheres (Cambridge Univ. Press, Cambridge)
Groot, P. J., Piters, A. J. M., & van Paradijs, J. 1996, A&AS, 118, 545
Hempelmann, A., Schmitt, J. H. M. M., Schultz, M., Rüdiger, G., & Stępien, K. 1995, A&A, 294, 515
Kitchatinov, L. L., & Rüdiger, G. 1999, A&A, 344, 911
Kürster, M. 2001, The CES User Manual `http://www.ls.eso.org/lasilla/Telescopes/360cat/ces/`
Kurucz, R. L. 1979, ApJS, 40, 1
Kurucz, R. L. 1993, in Peculiar versus normal phenomena in A-type and related stars, IAU Coll. 138, ed. Dworetsky et al., ASP Conf. Ser., 87
Kurucz, R. L. 1994, SAO, Cambridge, CDROM 20-22
Kupka, F., Piskunov, N. E., Ryabchikova, T. A., Stempels, H. C., & Weiss, W. W. 1999, A&AS, 138, 119
Lachaume, R., Dominik, C., Lanz, T., & Habing, H. J. 1999, A&A, 348, 897
Lang, K. R. 1992, Astrophysical Data I. Planets and Stars (Springer-Verlag, Berlin)
Messina, S., Rodonò, M., & Guinan, E. F. 2001, A&A, 366, 215
Townsend, R. 1997b, MNRAS, 284, 839
Uesugi, A., & Fukuda, I. 1982, Catalogue of stellar rotational velocities (revised), Kyoto: University of Kyoto, Departement of Astronomy, Rev. Ed

2.2 Oral presentation at the "12th Cambridge workshop on Cool Stars, Stellar Systems and the Sun", Boulder (2001)

to appear in PASP Conference Series

Detection of differential rotation in ψ Cap with profile analysis

A. Reiners[1], J.H.M.M. Schmitt[1], M. Kürster[2]

Abstract.

Differential rotation has been detected on the fast rotator ψ Cap (F5 V) using line profile analysis. The Fourier transforms of both Fe I λ5775 and Si I λ5772 are used to obtain a projected rotational velocity of $v \sin i = 42 \pm 1\,\mathrm{km\,s^{-1}}$. Modelling of the Fourier transformed profiles shows that the combined effects of equatorial velocity, inclination and differential rotation dominate the line profile while limb darkening and turbulence velocities have only minor effects. Rigid rotation is shown to be inconsistent with the measured profiles. Modelling the line profiles analogous to solar differential rotation we find a differential rotation parameter of $\alpha = 0.15 \pm 0.1$ ($15 \pm 10\%$) comparable to the solar case. To our knowledge this is the first successful measurement of differential rotation through line profile analysis. A cosnsistency check with an observable directly obtained from the Fourier transform was successful and proves the applicability of the observable to search for stellar differential rotation.

1. Introduction

According to the standard paradigm of stellar activity differential rotation is a central ingredient for the magnetic dynamo presumed to underlie all activity phenomena. In a turbulent convection zone differential rotation is expected to be a central element of stellar activity. The interaction of rotation and convection naturally produces deviations from rigid rotation. One example for this effect is the Sun, whose equator rotates $\sim 20\%$ faster than higher latitudes (Lang 1992). Direct predictions of the dependence of differential rotation on rotational velocity and spectral type have been made (e.g. Belvedere et al. 1980, Kitchatinov & Rüdiger 1999). Observations suggest a strong correlation between rotation and activity in late-type stars with many pieces of evidence summarized as "rotation-activity connection" (e.g. Hempelmann et al. 1995, Messina et al. 2001).

However, measurements of differential rotation among stars are either complicated or time-consuming or both. Three methods for determining stellar differential rotation have been used. (1) Variation of rotational periods; in the solar case spots emerge at certain latitudes and migrate across the surface from pole to equator. If the spots cause flux variations the rotational period of the

[1] Hamburger Sternwarte, Universität Hamburg, Gojenbergsweg 112, D-21029 Hamburg, Germany

[2] European Southern Observatory, Casilla 19001, Vitacura, Santiago 19, Chile

spot's latitude can be measured photometrically. In case of differential rotation the periods are expected to change with time (e.g. Donahue et al. 1996, Messina et al. 1999, Messina & Guinan 2001). (2) Doppler Imaging; On a solar like differentially rotating star spot groups migrating over the stellar surface disperse when the spots nearer to the equator move faster than those nearer to the pole. Two surface images of a star at two different times can reveal spot migrations and dispersions (e.g. Barnes et al. 2000, Donati & Collier Cameron 1997, Weber & Strassmeier 2001). For both methods (1) and (2) a huge amount of telescope time is needed what makes the observations of a larger sample very difficult. For the third method only one single line profile is sufficient: (3) Line profile analysis; direct examination of the subtle differences which exist between the line profile of a rigidly rotating star and that of a differentially rotating star. Although significant differences between the two cases are predicted, all previous attempts to measure differential rotation through line profiles alone remained unsuccessful and yielded results consistent with rigid rotation (Gray 1982, Dravins et al. 1990, Groot et al. 1996). At any rate, for a successful measurement one needs high spectral resolution and high signal to noise. With the Very Long Camera (VLC) of the Coudé Echelle Spectrograph (CES) at ESO's 3.6m telescope an instrumental setup satisfying these requirements is available. We report the detection of differential rotation in the F5 dwarf ψ Cap, to our knowledge the first successful measurement of differential rotation through line profiles.

2. Data

ψ Cap (HD 197 692, F5 V, $V_{\rm mag} = 4.13$, $v \sin i = 40\,{\rm km\,s^{-1}}$; Uesugi & Fukuda 1982) is the fastest rotator in a set of solar-like stars in the solar neighbourhood we observed on October 13, 2000 at ESO's 3.6m telescope (La Silla). The spectral resolution achieved with the CES / VLC setup was $R = 235\,000$ ($\sim 1.28\,{\rm km\,s^{-1}}$). Three consecutive exposures of ψ Cap of 270 s each covering the wavelength range between 5770 – 5810 Å were taken. The signal to noise ratio of the extracted spectrum is $S/N \sim 800$ per pixel with proper flat fielding and removal of interference pattern (Kürster 2001).

We concentrate our analysis on Fourier transforms of well isolated lines (Fe I λ5775 and Si I λ5772), for which continuum placement because of line blending is not a problem even for large $v \sin i$ values. The signal to noise ratio of our data is high enough to show the crucial features in the Fourier transform already from a single line.

Still, in Fe I λ5775 a small blend occurs from a neighbouring set of weak lines $\sim$ 0.8 Å apart, the influence of which on differential rotation determination is not clear. During our observing run a spectrum of the slow rotator ι Psc (HD 222 368; F7 V) was taken. In Fig.1a both spectra are shown, with the profile of ι Psc shifted according to its relative radial velocity. Deblending of Fe I λ5775 was accomplished by, first, removing the line in the spectrum of ι Psc "by hand", broadening this template with $v_{\rm rot} = 40\,{\rm km\,s^{-1}}$ and subtracting it from the ψ Cap spectrum. In Fig. 1b the recorded spectrum as well as the modified spectrum of ψ Cap (blue) are shown. Obviously, the Si I λ5772 equivalent widths of ψ Cap and ι Psc are the same, since it has been successfully removed (cf.

Fig.1b). The Fe I λ5775 line appears symmetric, thus we think that deblending was successful.

3. Method of Analysis

Absorption line profiles are influenced by a number of different effects. An absorption line profile at any point on the star is determined by temperature, gravity, element abundances and atomic parameters. This "intrinsic" profile is Doppler broadened by velocity fields. Many efforts have been undertaken to distinguish these velocity fields, one of them being the stellar rotation (see Gray 1988 and references therein). In addition to the projected rotational velocity of the star, radial-tangential macro- and isotropic microturbulence (denoted with $\zeta_{\rm RT}$ and ξ resp.) turned out to be a reasonable parameterization of stellar atmospheric velocity fields. These parameterizations assume that Doppler broadenings can be treated as convolutions; and that the "intrinsic" profiles are identical over the apparent stellar disk. For fast rotators ($v \sin i > 30\,\mathrm{km\,s^{-1}}$) and stationary atmospheres rotational broadening dominates and no complications occur with this assumption.

Interpreting the observed data profile $D(\lambda)$ as a a multiple convolution (denoted by $*$) between the intrinsic profile $F(\lambda)$ (including microturbulence broadening), the rotational broadening profile $G(\lambda)$, the instrumental profile $I(\lambda)$ and the macroturbulence profile $M(\lambda)$, $D(\lambda)$ can be written as

$$D(\lambda) = F(\lambda) * G(\lambda) * I(\lambda) * M(\lambda). \quad (1)$$

We calculated $F(\lambda)$ using the packages ATLAS9 (Kurucz 1979, Kurucz 1993) and BHT (Baschek et al. 1966). Atomic damping coefficients obtained from VALD (Kupka et al. 1999, Kurucz 1994) were included in the profile calculations; we chose solar metallicity and for the velocity dispersion of the opacity distribution function in ATLAS9 we used $1.0\,\mathrm{km\,s^{-1}}$. The temperature has been set to $T_{\rm eff} = 6500\,\mathrm{K}$ (Blackwell & Lynas-Gray 1998). To calculate $G(\lambda)$ a modified version of a package developed and described by Townsend (1997) is used. The surface integration is carried out over about 25 500 visible surface elements. The adopted limb-darkening law is given by

$$I(\cos\theta) = I_0\,(1 - \epsilon + \epsilon\cos\theta), \quad (2)$$

with θ denoting the angle between the surface element normal and the observer's line of sight and ϵ the limb darkening coefficient. We parametrize the differential rotation law through

$$\omega(l) = \omega_0 - \omega_1 \sin^2 l \quad (3)$$

with l being the latitude. Specifically, differential rotation is expressed in terms of $\alpha = \omega_1/\omega_0$. The differential rotation law (Eq. 3) is adopted from the solar case, where $\alpha_\odot = 0.20$; a more general approach would expand $\omega(l)$ in terms of orthogonal polynomials. The instrumental profile $I(\lambda)$ has been determined from the shapes of calibration lamp lines, a correction for thermal broadening according to the lamp temperature of 120°C was applied. The macroturbulence broadening function $M(\lambda)$ is adopted from Gray (1992).

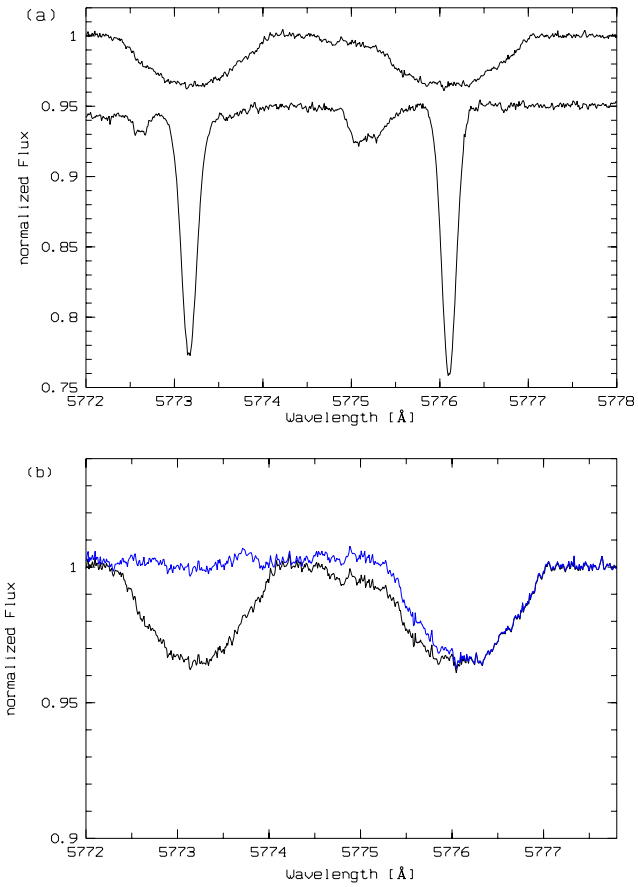

Figure 1. (a) Fe I λ5775 (right) and Si I λ5772 (left) lines of ψ Cap (upper line) and ι Psc (lower line; shifted along y-axis). (b) Original (black) and modified (blue) line profiles of ψ Cap (see text).

The contributions of different velocity fields are difficult to separate especially in the wavelength domain. In the Fourier domain convolutions become multiplications which are much easier to handle; the advantages of Fourier domain are discussed in detail by Gray (1992). In the Fourier domain Eq. 1 becomes

$$d(\sigma) = f(\sigma) \cdot g(\sigma) \cdot i(\sigma) \cdot m(\sigma). \quad (4)$$

The Fourier frequency σ is expressed in cycles / (km s^{-1}) = s km^{-1}. Especially zero positions of $g(\sigma)$ are not affected by multiplications with the functions $f(\sigma), i(\sigma)$ and $m(\sigma)$; $d(\sigma)$ shows the same zero positions as $g(\sigma)$.

Noise in Fourier domain can be expressed as $S_\sigma = S_\lambda \, \Delta\lambda \, N^{\frac{1}{2}}$ (Gray 1992), with S_λ being data noise and $\Delta\lambda$ step size in the wavelength domain, N is the number of data points. The Fourier transform of a real, symmetric profile yields a real function in the Fourier domain. Investigations of imaginary transforms of asymmetric lines show that these are no reliable tracers of profile properties (Gray 1980). We created a symmetric profile by mirroring the absorption profile at it's center; the achieved Fourier transform turned out to be stable against small variations of the center position. Rotational broadening, which dominates the line broadening in the case of ψ Cap, yields symmetric profiles. Asymmetries due to convection are believed to be of the order $v < 1\,\mathrm{km\,s^{-1}}$. In Fourier space this is $\sigma > 1\,\mathrm{s\,km^{-1}}$ while our analysis focuses on $\sigma < 0.04\,\mathrm{s\,km^{-1}}$. In the case of Fe I λ5775 an asymmetry may occur due to imperfect deblending, for Si I λ5772 no mechanism should contribute asymmetries of this order.

The Fourier transformed observed line profile was compared with a Fourier transformed model profile via a χ^2 test. Within our adopted modelling approach the following six fit parameters determine the model profiles: rotational velocity (v), inclination angle (i), differential rotation (α), limb darkening (ϵ), macro- (ζ_{RT}) and microturbulence (ξ). The χ^2-calculations have always been carried out directly on $d(\sigma)$. No further corrections have been applied to the data to avoid complications with amplified noise. Bruning (1984) pointed out that the convolution method induces systematic errors due to incorrectly estimated line depths especially in slow rotators. Our study is not focused on reproducing equivalent widths, which can be tuned e.g. by element abundances. The main goal is to reproduce the line shapes. Although we do not examine slow rotators in this study, normalized transformed profiles were used, that is, Fourier transformed profiles have been scaled to unity at $\sigma = 0$.

4. Results and Discussion

After a rough determination of $v \sin i$ a grid calculation in the six fit parameters was carried out. As to our model parameterization we note that this description contains parameters whose physics is poorly understood, i.e., the micro- and macroturbulence. We thus use χ^2 only as a relative parameter and not as an absolute criterion as to whether a model is acceptable or not; χ^2_{n} denotes the goodness of fit relative to the best fit, for which $\chi^2_{\mathrm{n}} = 1$ is set. For the actual grid we chose the parameter ranges of ϵ (0.4 – 0.8), ζ_{RT} (4.0 – 7.0) km s^{-1} and ξ (1.0 – 2.5) km s^{-1}. The rotation velocity was limited to $v < 120\,\mathrm{km\,s^{-1}}$ ($i > 20°$).

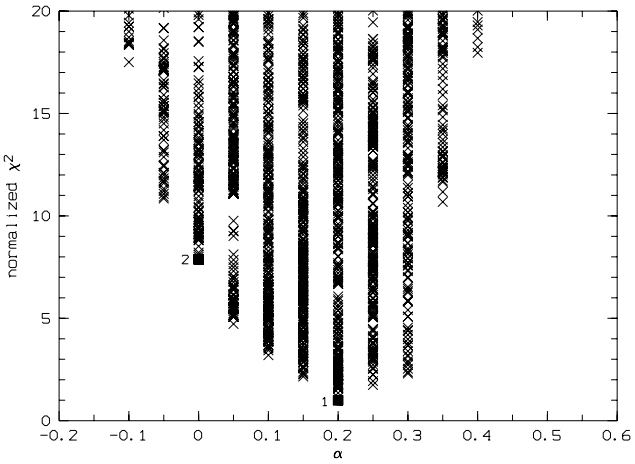

Figure 2. Normalized χ^2 vs. α for calculated models with various values of $v, i, \epsilon, \zeta_{\rm RT}$ and ξ (see text); each cross represents one set of parameters. Best fits of all models (1) and for rigid rotation (2) are denoted by full squares.

Goodness of fit calculations have been carried out independently on Fe I λ5775 and Si I λ5772; both lines show identical results. In the following we show only the results for Fe I λ5775.

In Fig. 2 we plot the resulting $\chi^2_{\rm n}$ as a function of the differential rotation parameter α; for each fixed value of α, we plot the $\chi^2_{\rm n}$ values obtained by varying all other model parameters. Clearly, a well defined lower envelope curve exists with a minimum at $\alpha = 0.20$. The best fits for differential rotation (here $\alpha = 0.20$; $\chi^2_{\rm n} = 1$, Model 1) and rigid rotation ($\alpha = 0.0$, $\chi^2_{\rm n} = 7.9$, Model 2) are marked by full squares; all parameters are shown in Tab. 1.

Table 1. Parameters of best fitting models for rigid and differential rotation

Model	v	i	α	ϵ	$\zeta_{\rm RT}$	ξ	χ^2_n
1	$43\frac{\rm km}{\rm s}$	80°	0.20	0.6	$4.0\frac{\rm km}{\rm s}$	$1.0\frac{\rm km}{\rm s}$	1.0
2	$48\frac{\rm km}{\rm s}$	60°	0.00	0.8	$7.0\frac{\rm km}{\rm s}$	$2.5\frac{\rm km}{\rm s}$	7.9

In Fig. 3 we plot the corresponding profiles in the Fourier domain; obviously, Model 1 provides a much better fit than Model 2, which is not an adequate description of our data. While no statistical uncertainties can be given on our $\chi^2_{\rm n}$-values, Fig. 3 shows $\chi^2_{\rm n}$-values of 7.9 to be clearly unacceptable.

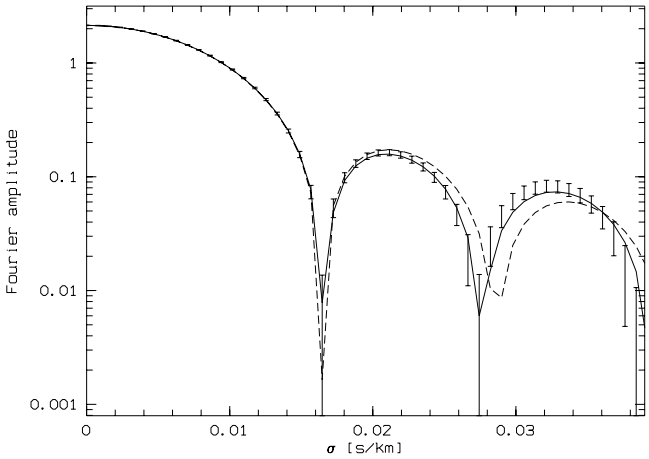

Figure 3. The Fourier transformed data indicated by error bars. Best fits for differential rotation ($\alpha = 0.20$; full line, Model 1) and rigid rotation ($\alpha = 0.0$; dashed line, Model 2) are shown. See Tab. 1 for parameters.

Inspection of the calculated $\chi^2_{\rm n}$-grid shows that the parameters $\epsilon, \zeta_{\rm RT}$ and ξ produce only second order effects; the fits are driven by the chosen values of v, i and α, and we cannot determine all model parameters independently. Therefore, we fixed the values $\epsilon = 0.6$ (Carbon & Gingerich 1969), $\zeta_{\rm RT} = 6.0\,{\rm km\,s^{-1}}$ and $\xi = 1.0\,{\rm km\,s^{-1}}$ (Gray 1988 and references therein). We emphasize that our subsequent findings do not require these specific parameter settings, and that the influences of ϵ, $\zeta_{\rm RT}$ and ξ are too small to revoke the effects of α, v and i. For the given parameters the best fit value for $v \sin i$ is $42.3\,{\rm km\,s^{-1}}$. We estimate the total systematic errors to be $\approx 1\,{\rm km\,s^{-1}}$. Models outside the range $42.3 \pm 1\,{\rm km\,s^{-1}}$ all have $\chi^2_{\rm n} > 5$.

Theoretical investigations of the line profile behaviour in Fourier space show that with differential rotation $\alpha \neq 0$ the inclination i becomes important (e.g. Bruning 1981). For comparable values of $v \sin i$ the best fit values of α and i are correlated. In Fig. 4 we consider calculated models with fixed ϵ, $\zeta_{\rm RT}$ and ξ, $v \sin i$ between 41.3 and $43.3\,{\rm km\,s^{-1}}$ and varying α, v and i. Three groups of models are distinguished; $\chi^2_{\rm n} < 5\,(\bullet)$, $5 < \chi^2_{\rm n} < 10\,(\circ)$ and $\chi^2_{\rm n} > 10\,(\cdot)$.

A well defined area of reliable fits in the $\alpha - i$ plot emerges. All fits with $\chi^2_{\rm n} < 10$ show $\alpha > 0.0$. Although we used no absolute criterion on wheter a model is acceptable, the estimation of systematic errors and a comparison with Fig. 3 shows that the threshold $\chi^2_{\rm n} < 10$ is a rather high choice.

A variety of combinations of equatorial velocity and inclination seems possible for $\alpha > 0$. A smaller differential effect is preferred for faster rotating models. For extremely high values of $v > 200\,{\rm km\,s^{-1}}$ rigid rotation might be argued, but such velocities seem unlikely given the age of ψ Cap of $\sim 2\,10^9$ a

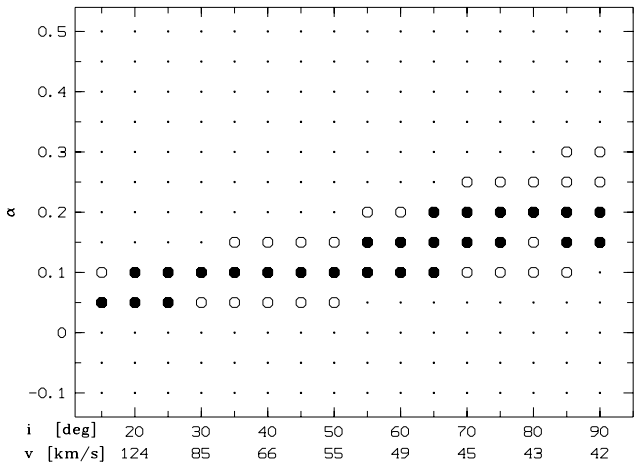

Figure 4. $\chi^2_{\rm n}$ of fits to Fe I λ5775 with $41.3\,{\rm km\,s^{-1}} < v \sin i < 43.3\,{\rm km\,s^{-1}}$, $\epsilon = 0.6$, $\zeta_{\rm RT} = 6.0\,{\rm km\,s^{-1}}$ and $\xi = 1.0\,{\rm km\,s^{-1}}$ in the $\alpha - i$ (v) plane: $\chi^2_{\rm n} < 5$ (•); $5 < \chi^2_{\rm n} < 10$ (○); $\chi^2_{\rm n} > 10$ (·).

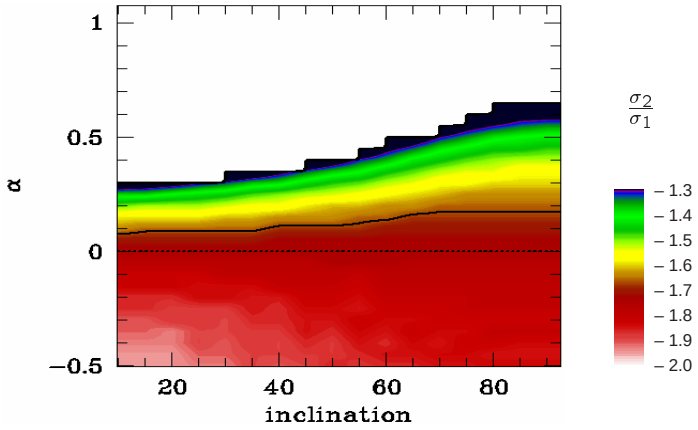

Figure 5. Ratio σ_2/σ_1 of second (σ_2) and first (σ_1) zero positions of a Fourier transformed line profile in the $\alpha - i$ plane ($\epsilon = 0.6$). From a measured value of σ_2/σ_1 an associated region can be found in the $\alpha - i$ plane. For ψ Cap we found $\sigma_2/\sigma_1 = 1.65 \pm 0.01$ which is marked with the solid line. As can be seen, σ_2/σ_1 is a well suited obeservable to determine solar-like differential rotation ($\alpha > 0$) but is not adequate for detection of anti-solar differential rotation ($\alpha < 0$).

(Lachaume et al. 1999). Even the minimum rotational velocity of $42\,\mathrm{km\,s^{-1}}$ seems uncommonly high. From Fig. 4 we derive $\alpha = 0.15 \pm 0.1$. The identical result was found for Si I λ5772, where the same procedure was applied.

As a consistency check we tried to determine the amount of differential rotation directly by the zero positions of $d(\sigma)$, which are inferred from the rotational broadening profile $g(\sigma)$. The ratio of the second (σ_2) and the first (σ_1) zero positions σ_2/σ_1 is sensitive to differential rotation as well as limb darkening (see e.g. Bruning 1981). For a rigid rotator σ_2/σ_1 is in the range $1.72 \ldots 1.83$ (Dravins et al. 1990). From the Fourier transform of ψ Cap we derive $\sigma_2/\sigma_1 = 1.65 \pm 0.01$, which clearly is outside the range accesible by rigid rotation and varying limb darkening only. In Fig. 5 σ_2/σ_1 is shown colour-coded in the $\alpha - i$ grid for $\epsilon = 0.6$. With a given value of σ_2/σ_1 a range of possible combinations in the $\alpha - i$ plane can be achieved. The solid line shows the value measured for ψ Cap and marks exactly the same region found in Fig. 4 by detailed atmospheric modelling. Thus σ_2/σ_1 can be used as an easily measurable observable to search for differential rotation in fast rotators.

To summarize differential rotation has been established for the rapid rotator ψ Cap independently from two absorption line profiles. While ψ Cap rotates at least 20 times faster than the Sun, it's differential rotation is comparable to the solar value, but not with the differential rotation patterns determined from Doppler images of the fast rotators AB Dor (Donati & Collier Cameron 1997) and PZ Tel (Barnes et al. 2000). As direct predictions for a F5 dwarf have not been calculated by (Kitchatinov & Rüdiger 1999) and the rotation period of ψ Cap is only poorly determined, the consistency of our result and the model is not clear. Assuming $R = 1.2\,\mathrm{R}_\odot$ and $i = 90°$, we find for ψ Cap the rotation law $\omega(l) = 4.38 - 0.66 \sin^2 l\,\mathrm{rad/d}$; ψ Cap does not rotate like a rigid body as suggested for AB Dor and PZ Tel. To compare theory and observations more detailed predictions especially on spectral type dependence and a greater sample of direct observations are needed. In particular verification of the differential rotation results of line profile analysis and Doppler imaging for the same star will be instructive.

Acknowledgments. A.R. acknowledges financial support from Deutsche Forschungsgemeinschaft under DFG-SCHM 1032/10-1.

References

Barnes J.R., Collier Cameron A., James D.J., Donati J.-F. 2000, MNRAS, 314, 162

Baschek B., Holweger H., Traving G. 1966, Abhandl. Hamburger Sternwarte, 8, 26

Belvedere G., Paternò L., Stix M. 1980, A&A, 88, 240

Blackwell D.E., Lynas-Gray A.E. 1998, A&AS, 129, 505B

Bruning D.H 1981, ApJ, 248, 274

Bruning D.H 1984, ApJ, 281, 830

Carbon D.F., Gingerich O. 1969, in Theory and Observation of normal stellar atmospheres, MIT Press, Ed. Gingerich O.

Donahue R.A., Saar S.H., Baliunas S.L. 1996, ApJ, 466, 384

Donati J.-F., Collier Cameron A. 1997, MNRAS, 291, 1

Dravins D., Lindegren L., Torkelsson U. 1990, A&A, 237, 137

Gray D.F. 1980, ApJ, 235, 508

Gray D.F. 1982, ApJ, 258, 201

Gray D.F. 1988, Lectures on spectral-line analysis: F, G and K stars, The Publisher, Arva

Gray D.F. 1992, The observation and analysis of stellar photospheres, Cambridge Univ. Press, Cambridge

Groot P.J., Piters A.J.M., van Paradijs J. 1996, A&AS, 118, 545

Hempelmann A., Schmitt J.H.M.M., Schultz M., Rüdiger G., Stępien K. 1995, A&A, 294, 515

Kitchatinov L.L., Rüdiger G. 1999, A&A, 344, 911

Kürster M. 2001, The CES User Manual; http://www.ls.eso.org/lasilla/Telescopes/360cat/ces/

Kurucz R.L. 1979, ApJS, 40, 1

Kurucz R.L. 1993, in Peculiar versus normal phenomena in A-type and related stars, IAU Coll. 138, Eds. Dworetsky et al., ASP Conf. Series, 87

Kurucz R.L. 1994, SAO, Cambridge, CDROM 20-22

Kupka F., Piskunov N.E., Ryabchikova T.A., Stempels H.C., Weiss W.W. 1999, A&AS, 138, 119

Lachaume R., Dominik C., Lanz T., Habing H.J. 1999, A&A, 348, 897

Lang K.R. 1992, Astrophysical Data I. Planets and Stars. Springer-Verlag, Berlin

Messina S., Guinan E.F., Lanza A.F., Armbruster C. 1999, A&A, 347, 249

Messina S., Rodonò M., Guinan E.F. 2001, A&A, 366, 215

Messina S., Guinan E.F., CS 12, Poster 06.07

Townsend R. 1997, MNRAS, 284, 839

Uesugi, A., Fukuda, I., Catalogue of stellar rotational velocities (revised), Kyoto: University of Kyoto, Departement of Astronomy 1982, Rev.ed

Weber M., Strassmeier K.G. 2001, A&A, 373, 974

Chapter 3

On the feasibility of the detection of differential rotation in stellar absorption profiles

3.1 A. Reiners, and J.H.M.M. Schmitt
Astronomy & Astrophysics, 384, 155 (2002)

A&A 384, 155–162 (2002)
DOI: 10.1051/0004-6361:20011801

Astronomy & Astrophysics

On the feasibility of the detection of differential rotation in stellar absorption profiles

A. Reiners[1] and J. H. M. M. Schmitt[1]

Hamburger Sternwarte, Universität Hamburg, Gojenbergsweg 112, 21029 Hamburg, Germany

Received 24 September 2001 / Accepted 12 December 2001

Abstract. Stellar differential rotation invokes subtle effects on line absorption profiles which can be best studied in the Fourier domain. Detailed calculations of the behavior of Fourier transformed profiles with respect to varying differential rotation, limb darkening and inclination angles are presented. The zero positions of the Fourier transform are found to be very good tracers of differential rotation. The ratio of the first two zero positions σ_2/σ_1 can be easily measured and is a reliable parameter to deduce the amount of differential rotation. It is shown that solar-like differential rotation (equatorial regions have larger angular velocity then polar regions) has an unambigious signature in the Fourier domain and that in certain cases it can easily be distinguished from limb darkening effects. A simple procedure is given allowing the determination of the amount of differential rotation by the knowledge of the first two zero positions of a line profile's Fourier transform alone (i.e., without the need for thorough atmospheric modelling), under the assumption of a linear limb darkening law with a limb darkening coefficient of $\epsilon = 0.6$.

Key words. stars: rotation – line: profiles

1. Introduction

Differential rotation is a central ingredient of the general accepted stellar activity paradigm, according to which a magnetic dynamo is ultimately responsible for the plethora of observed activity phenomena. Model calculations of stellar dynamos including differential rotation have been carried out (e.g. Kitchatinov & Rüdiger 1999) but only a few measurements of stellar differential rotation exist.

Three approaches to determine differential rotation exist: (a) By identifying individual features on Doppler maps and following their migration with time; (b) by studying the rotation law with time; and (c) by studying line profiles. Method (a) has been used for example for AB Dor (Donati & Collier Cameron 1997), PZ Tel (Barnes et al. 2000) and the rapidly rotating giant KU Pegasi (Weber & Strassmeier 2001). At least two different images of the surface of the star are necessary to draw conclusions about differential rotation by this method. The construction of two (or more) Doppler images requires good phase coverage with high signal to noise; consequently large amounts of observing time are needed. For method (b) it is assumed that activity regions dominating the rotational period migrate in latitude over the stellar surface during a magnetic cycle and thus lead to an apparent change in rotation rate. The observations must cover at least a complete magnetic cycle, which makes these projects difficult and time consuming, too. For method (c), which we want to revisit in this paper, only one single exposure with large spectral resolution and high signal to noise is needed. However, to our knowledge only one successful measurement (Reiners et al. 2001) of non-rigid rotation through line profile analysis exists.

The possibility of detecting differential rotation through line profile analysis is discussed in a serie of publications (Huang 1961; Gray 1977; Bruning 1981; García-Alegre et al. 1982), but the extent of these studies is limited to only a few cases, which do not provide a consistent overall picture. Furthermore, differences between the calculations are mentioned which can only partly be explained by the different underlying assumptions (see also Bruning 1982). In principle, a search for differential rotation effects can be carried out on every line profile measured with high signal to noise, however, in order to decide whether rigid rotation is consistent with the data or not a complete atmospheric model including all atomic data, turbulence and geometric effects must be carried out.

Send offprint requests to: A. Reiners,
e-mail: areiners@hs.uni-hamburg.de

This is rather cumbersome and no convenient observable is tabulated for a quick check on whether a star is differentially rotating or not.

The purpose of this paper is to revisit the effects of differential rotation on absorption line profiles. Detailed calculations are presented which in particular do allow a clear separation of the included model parameters. In particular we present tabulated observables for a quick and easy check on whether a line profile is consistent with rigid rotation or not. Thus large samples of stars can be analysed for differential rotation effects without the need to carry out a time-consuming line profile modelling for every object.

2. The Fourier-transformed profile

The basic assumption of our approach is to interpret a given absorption line profile $D(\lambda)$ as a convolution (denoted by $*$) between an "intrinsic" line profile $F(\lambda)$ – which here is the line profile including atomic data (e.g. damping coefficients), temperature and element abundance effects, turbulent velocity fields and instrumental effects – and a rotational broadening function $G(\lambda)$ including limb darkening. With this assumption $D(\lambda)$ can be written as

$$D(\lambda) = F(\lambda) * G(\lambda). \tag{1}$$

It is further assumed that the line profiles are identical over the stellar surface including the deeper layers. The validity of this assumption is not obvious and one has to check individual cases, but particularly for fast rotators rotation dominates the line profiles and our assumption becomes more and more reliable. Gray (1976) also developed broadening functions inferred from turbulent velocity fields. In this paper we show that, except for very slow rotators, the complete modeling of $D(\lambda)$ is not necessary for a determination of differential rotation.

For the analysis of absorption lines, Fourier transform of the profiles is convenient because Eq. (1) simplifies in Fourier domain to

$$d(\sigma) = f(\sigma) \cdot g(\sigma), \tag{2}$$

where we use the Fourier frequency σ expressed in cycles/(km s^{-1}) = s km^{-1} and $d(\sigma), f(\sigma)$ and $g(\sigma)$ are the Fourier transforms of $D(\lambda), F(\lambda)$ and $G(\lambda)$, respectively. In the Fourier domain convolutions become multiplications. Therefore any zero in the Fourier transformed rotational broadening function $g(\sigma)$, which contains the information on differential rotation, must also appear in the observed Fourier transform $d(\sigma)$. The latter can be observed in the transformed data profiles without any data manipulation and in particular without any deconvolution of $F(\lambda)$.

For rigid rotation the zeros in $g(\sigma)$ can be analytically calculated. Using the limb darkening law

$$I_\lambda(\theta)/I_\lambda(0) = 1 - \epsilon + \epsilon\cos\theta, \tag{3}$$

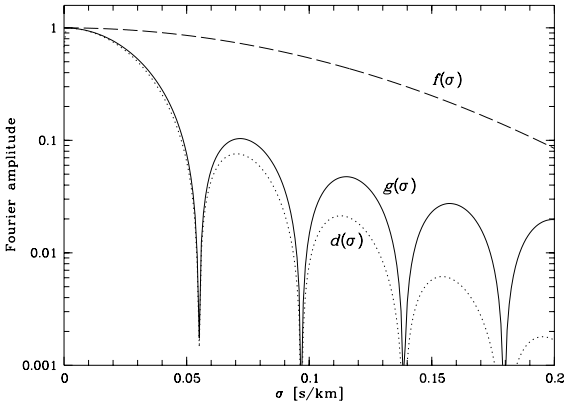

Fig. 1. A typical normalized Fourier transformed rotational broadening function $g_\epsilon(\sigma)$ ($v \sin i = 12$ km s^{-1}; solid line) and the Fourier transform of a Gaussian broadening function $f(\lambda)$, (e.g. isotropic turbulence) with $v_{\rm iso} = 5$ km s^{-1} (dashed line). The multiplication $d(\sigma) = f(\sigma) \cdot g(\sigma)$ is shown with a dotted line.

where $I_\lambda(\theta)$ denotes the intensity from a surface element, whose angle between its normal and the observer's line of sight is given by θ. The limb darkening dependent rotationally broadening profile centered at some wavelength λ_0 can be expressed as

$$G_\epsilon(\lambda - \lambda_0) = \frac{2(1-\epsilon)\left(1-\left(\frac{\lambda-\lambda_0}{\delta}\right)^2\right)^{\frac{1}{2}} + \frac{\pi\epsilon}{2}\left(1-\left(\frac{\lambda-\lambda_0}{\delta}\right)^2\right)}{\pi\delta\left(1-\frac{\epsilon}{3}\right)}, \tag{4}$$

where $\mid \lambda - \lambda_0 \mid < \delta$ and $\delta = (\lambda_0 v \sin i)/c$ (cf. Unsöld 1968; Gray 1976). In terms of the variable $x = 2\pi\delta\sigma$ the Fourier transform of Eq. (4) is given by Böhm (1952) as:

$$g_\epsilon(\sigma) = \frac{2}{x(1-\frac{\epsilon}{3})}\left[(1-\epsilon)J_1 x + \epsilon\left(\frac{\sin x}{x^2} - \frac{\cos x}{x}\right)\right], \tag{5}$$

with $J_1(x)$ denoting the first order Bessel-function. The ϵ dependent zeros of g_ϵ are therefore determined from the equation

$$(1-\epsilon)J_1 x + \epsilon\left(\frac{\sin x}{x^2} - \frac{\cos x}{x}\right) = 0. \tag{6}$$

An example of a typical normalized Fourier transformed rotational broadening function $g_\epsilon(\sigma)$ is shown in Fig. 1. The "main lobe" centered on $\sigma = 0$ is followed by a series of "sidelobes". Important attributes are the zero positions σ_1, σ_2 etc. and the sidelobe amplitudes I_1, I_2 etc. The dashed line shows the Fourier transform of an assumed intrinsic Gaussian line profile with a dispersion of $v_{\rm disp} = 5$ km s^{-1}. The Fourier transformed data profile $d(\sigma) = g(\sigma) \cdot d(\sigma)$ is shown with a dotted line. Since in our specific case the Fourier transformed broadening function $f(\sigma)$ decreases monotonically, the amplitudes of the

sidelobes especially at higher frequencies ($I_2, I_3 \ldots$) are affected by the multiplication with $f(\sigma)$ while the zero positions of $g(\sigma)$ remain unchanged and their determination require no knowledge of $f(\sigma)$.

$g_\epsilon(\sigma)$ and its zero positions σ_n scale with $v \sin i$ (Carroll 1933a; Carroll 1933b); σ_n can be expressed as

$$\sigma_n = q_n(\epsilon) / v \sin i. \quad (7)$$

Thus, given ϵ, $v \sin i$ can directly be determined from the zero positions of $d(\sigma)$. Dravins et al. (1990) found an approximation for $q_1(\epsilon)$ and $q_2(\epsilon)$:

$$q_1 = 0.610 + 0.062\epsilon + 0.027\epsilon^2 + 0.012\epsilon^3 + 0.004\epsilon^4 \quad (8)$$

$$q_2 = 1.117 + 0.048\epsilon + 0.029\epsilon^2 + 0.024\epsilon^3 + 0.012\epsilon^4 \quad (9)$$

$$\frac{q_2}{q_1} = 1.831 - 0.108\epsilon - 0.022\epsilon^2 + 0.009\epsilon^3 + 0.009\epsilon^4 \quad (10)$$

and thus

$$1.72 < \frac{q_2}{q_1} < 1.83 \qquad (0.0 < \epsilon < 1.0). \quad (11)$$

For a parameterization of differential rotation we use a rotation law analogous to the solar case:

$$\omega(l) = \omega_0 - \omega_1 \sin^2 l, \quad (12)$$

with l denoting latitude. Specifically, differential rotation is expressed in terms of α,

$$\alpha = \frac{\omega_1}{\omega_0} \qquad (\alpha_\odot = 0.20); \quad (13)$$

$\alpha = 0$ means solid body rotation, $\alpha > 0$ equatorial acceleration (solar-like differential rotation) and $\alpha < 0$ polar acceleration.

Many efforts have been undertaken to find a parameterization of $g_{\epsilon,\alpha}(\sigma)$ for the case of a differentially rotating star. Huang (1961) found solutions for special cases ($i = 90°, \epsilon = 0.0$) but no analytical forms for the general case are known. Thus modeling of differential rotation has to be performed by numerical integration over the stellar surface. Gray (1977) examined the equator-on case ($i = 90°$) and found that the ratio of first to second sidelobe amplitudes is smaller in case of solar-like differential rotation ($\alpha > 0$). Bruning (1981) and García-Alegre et al. (1982) calculated profiles for differentially rotating stars; Bruning's calculations assume $\epsilon = 0.6$ while García-Alegre et al. neglected limb-darkening ($\epsilon = 0.0$). Both authors also investigated a few cases with $i < 90°$ and found differences to the equator-on case. Substantial differences exist between the mentioned calculations, which Bruning (1982) attributed to the different values of the limb darkening parameter ϵ used. Furthermore, although Bruning (1981) did not directly mention the amplitude of the second sidelobe, his Fig. 4 is inconsistent with the calculations of García-Alegre et al. (1982). Bruning's Table 1 has been the reference for analyses e.g. by Gray (1982).

We thus conclude that previous calculations do not show a clear picture of the important parameter dependences of differential rotation. No approximations for Eqs. (8)–(10) with α included are known. We therefore carried out detailed calculations of the changes of Fourier transformed line profiles with differential rotation, and especially focused on the inclination dependence and the possibility of distinguishing limb darkening effects from differential rotation effects.

3. Model

Let us first consider the rotational broadening function $G(\lambda)$ for a differentially rotating star. For the case of rigid rotation $G(\lambda)$ can be expressed analytically as in Eq. (4), to numerically calculate $G(\lambda)$ for the case of differential rotation we use a modified version of the package developed and described by Townsend (1997). The rotation law (12) and limb darkening law (3) was applied. The integration is carried out over 25 500 visible surface elements. To reduce numerical noise we used a Gaussian profile as input function instead of a δ-function. This is equivalent to the convolution of a Gaussian profile $F(\lambda)$ with the desired rotational broadening profile $G(\lambda)$. We chose an equivalent width of 1 Å for the Gaussian input function, which implies that the Fourier transformed profile is normalized to amplitude 1 at the abscissa. Similar to the convolution of the rotational broadening profile $g(\sigma)$ with the intrinsic line broadening profile $f(\sigma)$ discussed in Sect. 2, our specifically chosen input function affects the amplitude of $g(\sigma)$ and has to be taken into account when amplitudes of $g(\sigma)$ are considered. However, in our case the Fourier transformed Gaussian input profile has an amplitude of 99.93% at 0.2 s km^{-1}; since our study focuses on the region $\sigma < 0.15$ s km^{-1}, we applied no correction to $g(\sigma)$.

We arbitrarily centered the input function at $\lambda_0 = 6251.826$ Å. We chose a spectral resolution of 0.003 Å (0.14 km s^{-1}) and used a grid of 8192 points on which Fourier components were computed. The calculated profiles depend on four parameters, the differential rotation α, the limb darkening coefficient ϵ, equatorial rotational velocity $v_{\rm eq}$ and the inclination i of the rotation axis.

4. Results

In Figs. 2–4 we show the dependence of the absorption line profiles (left panel) and the corresponding Fourier transforms (right panel) for a projected rotational velocity of $v \sin i = 12$ km s^{-1} on α, ϵ and i. Figure 2 shows the behaviour with changing limb darkening ϵ for rigid rotation ($\alpha = 0$); in Fig. 3 we consider variable amounts of differential rotation for constant $\epsilon = 0.6$; and in Fig. 4 we investigate the influence of varying the inclination angles i for the case of a solar-like differentially roting star ($\alpha = 0.35$) with $\epsilon = 0.6$.

In the data domain all three parameters α, ϵ and i change the line profile in a similar way, also the changes are at the percent level showing the necessity of high signal-to-noise data. In Fourier domain, however, the signatures become distinguishable; note that in the Fourier domain the ordinate is plotted with a logarithmic scale, while in

158 A. Reiners and J. H. M. M. Schmitt: Detection of differential rotation in absorption profiles

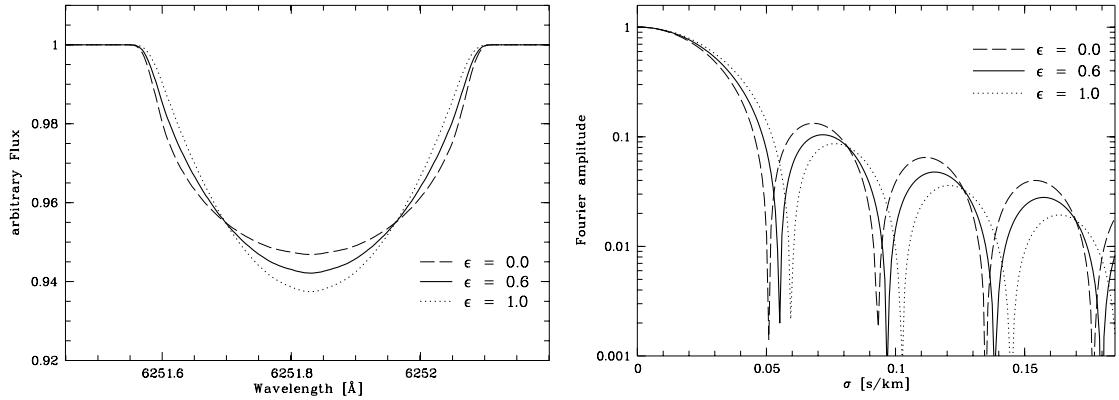

Fig. 2. Absorption line profiles for $v \sin i = 12\ \mathrm{km\,s^{-1}}$ and rigid rotation ($\alpha = 0$; $i = 90°$) in data domain (left) and Fourier domain (right). Three different cases of limb darkening ($\epsilon = 0.0, \epsilon = 0.6$ and $\epsilon = 1.0$) are indicated by dashed, solid and dotted lines, respectively. Note that in Fourier domain the ordinate is plotted with logarithmic scale, while in data domain it is a linear scale.

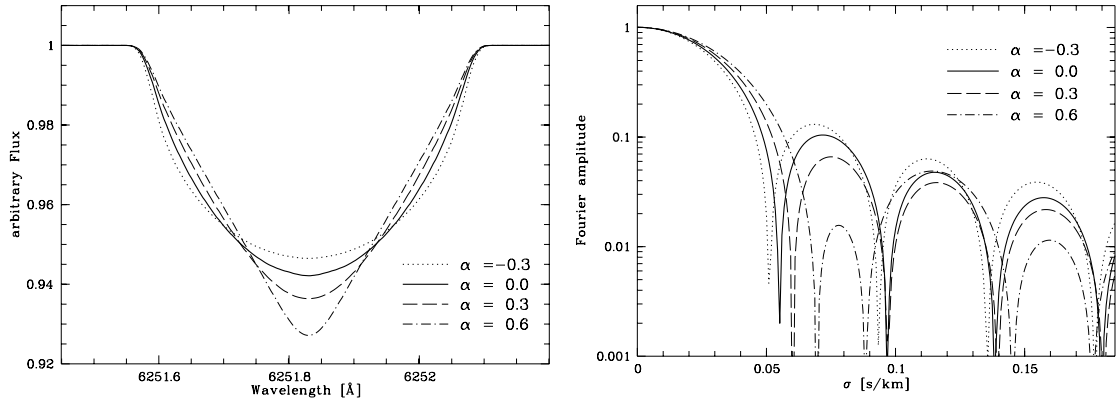

Fig. 3. Absorption line profiles as in Fig. 2 for limb darkening $\epsilon = 0.6$ and $i = 90°$. Different cases of differential rotation ($\alpha = -0.3, \alpha = 0.0, \alpha = 0.3$ and $\alpha = 0.6$) are indicated. In the Fourier domain the different behaviour of the first sidelobe is evident, it narrows for larger differential rotation, while it's amplitude lessens. The amplitude of the second sidelobe changes slightly.

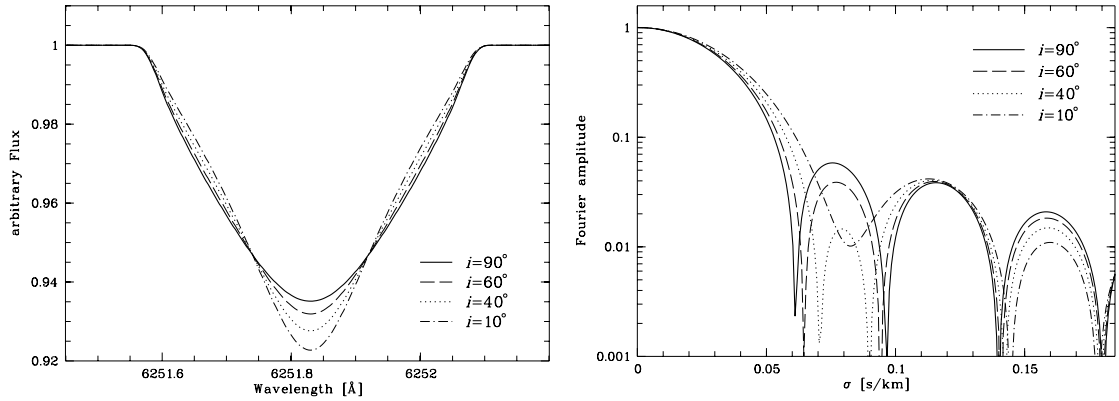

Fig. 4. Absorption line profiles as in Fig. 2 for limb darkening $\epsilon = 0.6$ and differential rotation ($\alpha = 0.35$). Different inclination angles at constant $v \sin i$ ($i = 90°, i = 60°, i = 40°$ and $i = 10°$) are indicated. The behaviour of the first sidelobe with smaller inclination is comparable to the case of larger differential rotation. The amplitude of the second sidelobe remains constant.

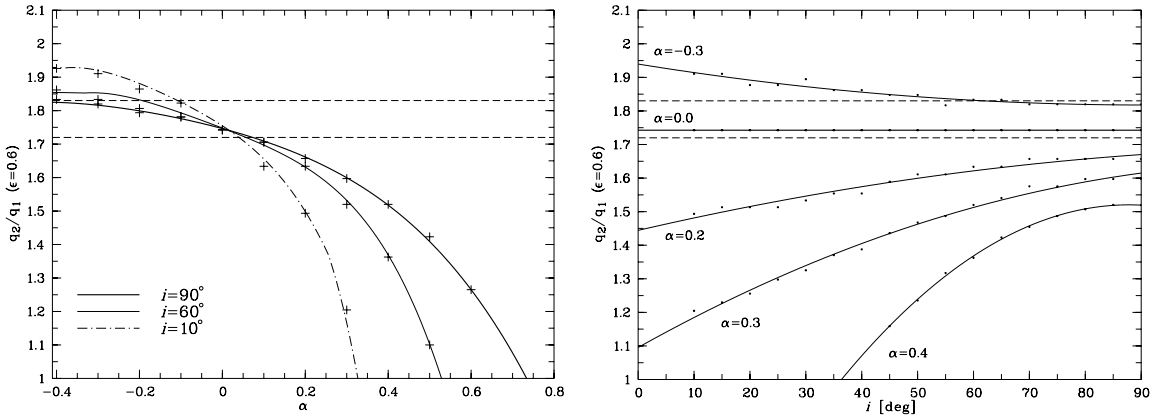

Fig. 5. q_2/q_1 plotted versus α (left) and versus i (right); $\epsilon = 0.6$. Calculated values are marked by crosses in the left and by dots in the right plot. Hand drawn lines of constant inclination (left) respectively constant differential rotation (right) connect the values. Dashed lines define the region which can be achieved by rigid rotation ($\alpha = 0.0$) and varying limb darkening ($0.0 \leq \epsilon. \leq 1.0$).

the data domain it is a linear scale. We confirm that limb darkening (Fig. 2) changes the zero positions σ_i and amplitudes of all sidelobes I_i in a similar way. Differential rotation (Fig. 3) narrows the first sidelobe and diminishes its amplitude I_1 while the amplitude of the second sidelobe I_2 is only slightly affected. Our calculations are consistent with Gray (1977), Bruning (1981) and García-Alegre et al. (1982) and confirm that the first sidelobe of a Fourier transformed line profile is sensitive to differential rotation. As can be seen in Fig. 4, smaller inclination angles do mimic stronger differential rotation; note that $v \sin i$ remains constant in the profiles. For inclination angles as small as $i = 10°$ the first sidelobe even vanishes. On the other hand, the amplitude of the second sidelobe is only slightly affected by changing differential rotation α (non-varying inclination i, Fig. 3) and it remains almost constant with changing inclination i and constant differential rotation α (Fig. 4).

Bruning (1981) calculated σ_1, σ_2 and I_1 while García-Alegre et al. (1982) showed I_1 and I_1/I_2. Our results are in good agreement with the results of Bruning for $i = 90°$, for $i < 90°$ deviations of up to 15% can be recognized. Calculations of I_1 agree with the calculations from García-Alegre et al. for all cases of α and i while their ratios of first and second sidelobe amplitudes I_1/I_2 are systematically higher (up to 25%) than our values. We attribute these differences to the width of the used input function. García-Alegre et al. used a Gaussian profile which is not further specified. If their input function has a significant line width, the amplitudes of higher sidelobes will be diminished, as explained in Sect. 3 resulting in a higher ratio I_1/I_2.

The two most instructive ratios of observable parameters are, first, the ratio of the second and first zero positions σ_2/σ_1 (which is identical to q_2/q_1) and, second, the ratio of the first and second sidelobe amplitudes I_1/I_2. According to Eq. (11) the value of q_2/q_1 varies between 1.72 and 1.83 for a rigidly rotating star by varying ϵ. As mentioned in Sect. 2, for a sufficiently high rotation rate the zero positions of a Fourier transformed profile are only affected by the rotation law. A measured value of σ_2/σ_1 outside that range (1.72–1.83) must therefore be a direct indication of differential rotation.

Figure 5 shows the value q_2/q_1 for different combinations of α and i (keeping $\epsilon = 0.6$ fixed). In the left panel the values are plotted versus α, in the right panel versus inclination i. Calculated values are marked by crosses in the left and by dots in the right panel. Lines of constant inclinations (left) resp. constant differential rotation values (right) connect the calculated values. The dashed lines define the region of q_2/q_1 between 1.72 and 1.83, where rigid rotation is possible.

Clearly, well defined dependences of q_2/q_1 on α and i appear which exceed the effects caused by limb darkening and rigid rotation alone. In all cases q_2/q_1 shows a monotonic behaviour; it diminishes (the first sidelobe becomes narrower) with larger α and smaller inclination i. For extreme values of differential rotation and for small inclination angles, q_2/q_1 crosses the ordinate, i.e. the first sidelobe vanishes (cf. Fig. 4). Although it is not possible to determine both α and i from a measured value of q_2/q_1 simultaneously, this easily measured value is suitable to rule out rigid rotation for many cases.

Figure 6 shows a contour plot of the parameter q_2/q_1 vs. α and i for the case $\epsilon = 0.6$ (solid lines); it can be used to determine the permitted α/i-combinations from a measured q_2/q_1-ratio. The dashed lines mark the values of q_2/q_1 which can be achieved with solid body rotation and extreme limb darkening parameters alone. Small values of q_2/q_1 are expected for small inclination angles combined with differential rotation of the order of the solar value. Above the 1.3-contour the gradient of q_2/q_1 is very steep

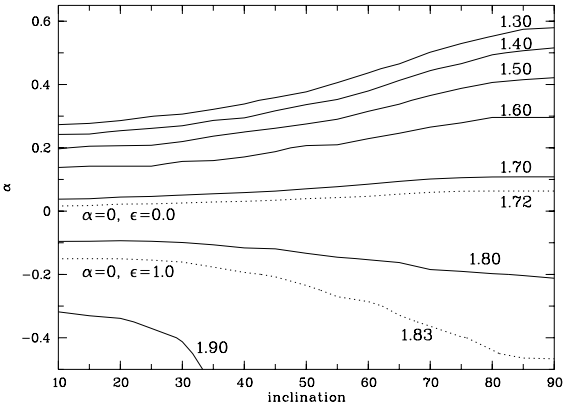

Fig. 6. Contour-plot of q_2/q_1 in the $\alpha - i$ plane. Solid lines mark the possible combinations of differential rotation α and inclination i for a given q_2/q_1 with limb darkening $\epsilon = 0.6$. Dashed lines show the region which is accessible with rigid rotation ($\alpha = 0.0$) and varying limb darkening ϵ.

and lines for $q_2/q_1 = 1.2$ and 1.1 are not drawn for better legibility. The first sidelobe vanishes close to the 1.3-line.

The second measurable ratio, I_1/I_2, is shown in Fig. 7 for $\epsilon = 0.6$. A systematic behaviour can also be noticed here; for positive α (solar-like differential rotation) the situation is comparable with that of q_2/q_1, but for negative α (anti-solar differential rotation; polar regions rotate faster than the equator) the ratio lessens as well. Thus I_1/I_2 can validate results obtained with q_2/q_1, but the sense of differential rotation cannot be determined using this value. Moreover, unlike q_2/q_1, I_1/I_2 is affected by the intrinsic line profile $f(\sigma)$, which involves additional velocity fields, intrinsic parameters like temperature and atomic data, and the instrumental profile. In Fig. 1 the shown Fourier transform of the isotropic velocity field with $v_{\rm iso} = 5$ km s^{-1} can be interpreted as an approximation of a Fourier transformed intrinsic line profile $f(\sigma)$. While $g(\sigma)$ scales in σ-direction with varying $v \sin i$, $f(\sigma)$ remains constant. Thus the sidelobe amplitudes of $d(\sigma)$ are affected by the shape of $f(\sigma)$ and particularly for slower rotators I_1/I_2 becomes unreliable. Therefore, in order to use the ratio I_1/I_2 for determination of differential rotation, $g(\sigma)$ has to be deconvolved from the data $d(\sigma)$, and especially for slower rotators a complete line profile modelling is required.

5. An example: ψ Cap

As an example for the application of the above procedure we show the determination of α/i-combinations from the absorption line Fe I λ5775 of the differentially and rapidly rotating F5 dwarf ψ Cap ($v \sin i = 42 \pm 1$ km s^{-1}). The data has been taken during an 810 s exposure on Oct. 13, 2000 with the CES at ESO 3.6 m, $S/N \sim 800$; a complete analysis has been presented by Reiners et al. (2001). Although the S/N ratio is rather high, we mirrored the line profile at its center to achieve an even higher S/N ratio and to obtain a symmetric profile. Since the main broadening mechanism for ψ Cap is rotation, symmetry of the profile is expected and no problems should arise with mirroring. No further corrections were applied to the data and especially no corrections for turbulence or instrumental broadening were made.

Table 1. Fourier transformed Fe I λ5775 intensities and zero positions of ψ Cap.

	q_1	q_2	I_1	I_2	q_2/q_1	I_1/I_2
	0.017	0.027	0.078	0.041	1.65	1.914
$\pm$	0.001	0.001	0.003	0.003	0.01	0.004

In Table 1 we show the values for zero positions and sidelobe intensities derived from our CES spectrum of ψ Cap. The zero positions were determined from the intersection of a regression line defined by the nearest three points neighbouring the zero position with unambigious sign and the abscissa. We estimated the error of the zero positions by regression lines through the respective point plus (minus) S_σ. For ψ Cap we derive $q_2/q_1 = 1.65 \pm 0.01$. In Fig. 8 the corresponding combinations of inclination i and differential rotation α is shown. Clearly, the thus defined region (black area with $1.64 \leq q_2/q_1 \leq 1.66$) is significantly distinct from that accessible by rigid rotation and arbitrary limb darkening. In particular, the thus defined region is fully consistent with the parameter region determined from a complete atmospheric modelling of the ψ Cap data (cf. Fig. 4 in Reiners et al. 2001). Since the result derived from q_2/q_1 is the same as that derived from the complete atmospheric fit, we argue that q_2/q_1 is an adequate observable to quickly and reliably determine solar-like ($\alpha > 0$) differential rotation for fast rotators.

We mention in passing that the measured ratio of the sidelobe amplitudes $I_1/I_2 = 1.914 \pm 0.004$ also supports the result that ψ Cap is no rigid rotator (cp. with Fig. 7). Although we showed that great care has to be taken using I_1/I_2 for differential rotation determination, in the case of the fast rotator ψ Cap the sidelobe amplitudes are expected to be only marginally affected by turbulent velocity fields and instrumental effects.

6. Summary

We have carried out detailed calculations of the dependence of Fourier transformed line profiles on differential rotation α and the inclination angle, focusing on the question, to what extent differential rotation can be distinguished from limb darkening effects and to what extent inclination matters. We have excluded the question of how starspots can influence the reliability of the method. This will be the topic of a further publication.

Our calculations assume an approximation of the Maunder differential rotation law analogous to that derived for the solar case and a linear limb darkening law. Alternative rotation or limb darkening laws and influences

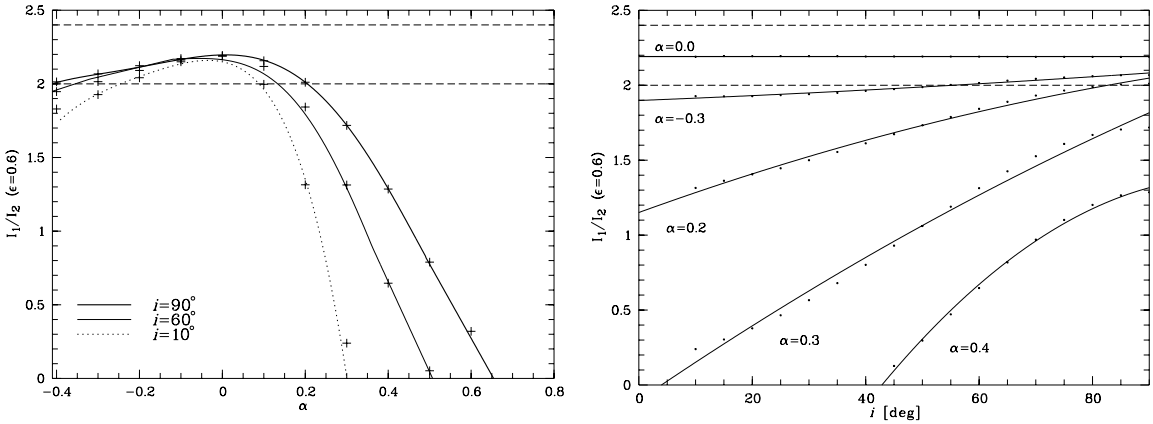

Fig. 7. I_1/I_2 for $\epsilon = 0.6$ plotted in the same way as q_2/q_1 in Fig. 5. I_1/I_2 also depends strongly on α and i but shows a non-monotonic behaviour. Note that in the right panel the line for $\alpha = -0.3$ lies below the line for $\alpha = 0.0$.

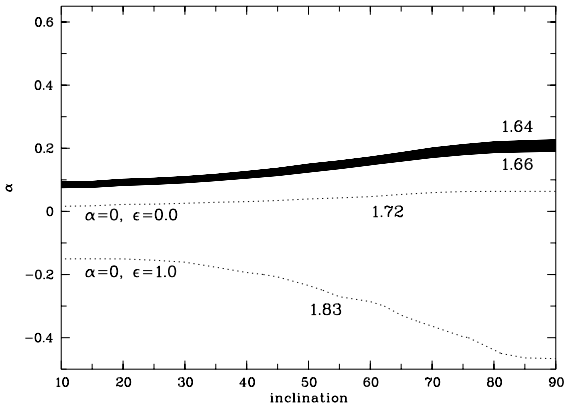

Fig. 8. Contour-plot of q_2/q_1 with the derived region for ψ Cap ($1.64 \leq q_2/q_1 \leq 1.66$) marked black. The black area is clearly different from that accessible with rigid rotation (area between the dottet lines) and occupies the same region as that found by Reiners et al. (2001) in their Fig. 4.

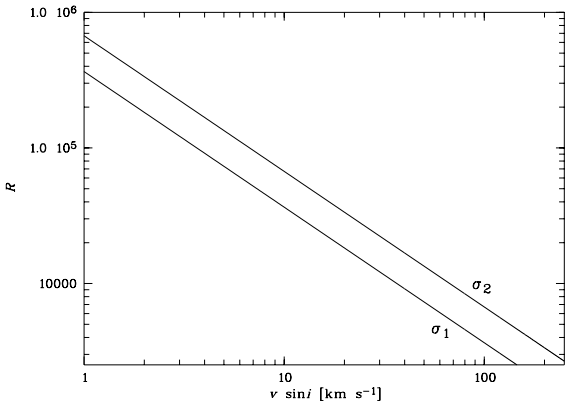

Fig. 9. The required resolution R for the detection of the first (σ_1) and second (σ_2) zero positions for a star with a projected rotational velocity of $v \sin i$ and rigid rotation ($\alpha = 0.0$).

of spots have not been investigated yet. Although we intend to carry out calculations including a greater variety of assumptions we do not expect large differences in our results. Our analysis focuses on the low frequency part of the Fourier transforms while small bumps produced by small scale spots or small deviations from the rotation and limb darkening laws are expected to influence only the high frequency part of the Fourier spectrum. However, we do want to point out that large polar spots as found in many Doppler images on a variety of stars may possibly influence our results.

Two measurable values – q_2/q_1, the ratio of the second and the first zero of the Fourier transform, and I_1/I_2, the ratio of the amplitudes of the first and second sidelobes – have been studied. A reliable interpretation of a measured value of I_1/I_2 is quite difficult because those ratios are affected by the – in general unknown – intrinsic line profile. Only for very rapid rotators this ratio can be disentangled from the intrinsic line profile characteristics. The sign of differential rotation cannot be determined with this ratio. However, q_2/q_1 turned out to be a very reliable tracer of differential rotation. The measurement of q_2/q_1 is straightforward and can be used without any modelling of line profiles. q_2/q_1 does carry information about differential rotation; a value of $q_2/q_1 < 1.72$ is a direct indication for a solar-like differential rotation law, while $q_2/q_1 > 1.83$ indicates anti-solar differential rotation. The combination of inclination angle i and differential rotation α remains ambiguous, but information on period and radius of the star can confine possible parameter regions.

As is clear from Fig. 6 for a given value of α, smaller inclinations always lead to larger deviations from the rigid rotation case, but obviously small inclination angles diminish the projected value of $v \sin i$ and the given spectral resolution limits the measurement of σ_2. Consequently sufficiently large $v \sin i$ values are needed. Thus there is a bias in our detectability of differential rotation.

For slow rotators the Nyquist frequency σ_ν, i.e. the maximum Fourier frequency σ contained in a Fourier transform of a line profile obtained with a resolution R, limits the detection of σ_2. For fast rotators the situation improves dramatically and no problems arise with the measurement of σ_2. In Fig. 9 the required resolution for the detection of the first (σ_1) and second (σ_2) zero positions of $g(\sigma)$, the Fourier transform of a rigid rotation broadening function $G(\lambda)$, observed with a specified value of $v \sin i$ is shown. A resolution of the order $R = 70\,000$ is needed to determine σ_2 for a star with $v \sin i = 10$ km s^{-1}. Known complications like aliasing emphasize the need for a somewhat higher resolution.

Our picture of stellar rotation law is still very poor (e.g. Gray 1977, 1982; Wöhl 1983). Information on a large sample of moderate rotators with high sensitivity to differential rotation would be instructive for our understanding of stellar dynamo processes. This can easily be accomplished by measuring the q_2/q_1 ratios as shown in this paper.

References

Barnes, J. R., Collier Cameron, A., James, D. J., & Donati, J.-F. 2000, MNRAS, 314, 162

Böhm, K. 1952, Zeit. f. Astrophysik, 30, 117

Bruning, D. H. 1981, ApJ, 248, 274

Bruning, D. H. 1982, A&A, 115, 203

Carroll, J. A. 1933a, MNRAS, 93, 478

Carroll, J. A. 1933b, MNRAS, 93, 680

Donati, J.-F., & Collier Cameron, A. 1997, MNRAS, 291, 1

Dravins, D., Lindegren, L., & Torkelsson, U. 1990, A&A, 237, 137

García-Alegre, M. C., Vázquez, M., & Wöhl, H. 1982, A&A, 106, 261

Gray, D. F. 1976, The observation and analysis of stellar photospheres (Wiley, New York)

Gray, D. F. 1977, ApJ, 211, 198

Gray, D. F. 1982, ApJ, 258, 201

Huang, S.-S. 1961, ApJ, 133, 130

Kitchatinov, L. L., & Rüdiger, G. 1999, A&A, 344, 911

Reiners, A., Schmitt, J. H. M. M., & Kürster, M. 2001, A&A, 376, L13

Townsend, R. 1997, MNRAS, 284, 839

Unsöld, A. 1968, Physik der Sternatmosphären (Springer, Berlin)

Weber, M., & Strassmeier, K. G. 2001, A&A, 373, 974

Wöhl, H. 1983, in Solar and Stellar Magnetic Fields: Origin and Coronal Effects, ed. J. O. Stenflo (Reidel Dordrecht), IAU Symp., 102, 155

Chapter 4

Can star spots mimic differential rotation?

4.1 A. Reiners, and J.H.M.M. Schmitt
Astronomy & Astrophysics, 388, 1120 (2002)

A&A 388, 1120–1123 (2002)
DOI: 10.1051/0004-6361:20020564

Astronomy & Astrophysics

Can star spots mimic differential rotation?

A. Reiners and J. H. M. M. Schmitt

Hamburger Sternwarte, Universität Hamburg, Gojenbergsweg 112, 21029 Hamburg, Germany

Received 30 January 2002 / Accepted 20 March 2002

Abstract. The search for stellar differential rotation in Fourier-transformed profiles utilizes subtle deviations from the standard rotation profile. We investigate the influence of stellar spots on the results obtained with the Fourier Transform Method. Different spot configurations, especially polar spots, are examined, and their influence on Fourier-transformed line profiles studied. We found that polar spots cannot mimic solar-like differential rotation and are thus not critical for the use of the Fourier Transform Method. Although not indicated by Doppler imaging, other configurations may occur on stellar surfaces and their influence on the analysis is discussed. A symmetric distribution of spots in an activity belt leads – in a small region of the parameter space – to line profiles that are very similar to the signatures produced by differential rotation.

Key words. starspots – stars: rotation

1. Introduction

The solar rotation law and its applicability to stars other than the Sun play a key role in our understanding of the solar/stellar dynamo and activity. Evidence for the differential rotation of the Sun comes from long-term observations of solar spots and from helioseismology (Howard 1984; Schou et al. 1998). Rotation laws on other stars cannot be observed directly and different approaches have been developed. One method is to search for effects of differential rotation in the line profiles, that was first discussed by Huang (1961). The usefulness of the Fourier transform in this context was realized by Gray (1977), and the effects of differential rotation on Fourier-transformed line profiles were studied in detail by Reiners et al. (2002). They specifically show that the Fourier Transform Method (FTM) is capable of detecting stellar differential rotation under certain circumstances.

The Fourier-transformed line profile of a rotating star shows a characteristic shape (Fig. 1), that is dominated by a "main lobe" at low frequencies, followed by smaller "sidelobes" at higher frequencies. Reiners et al. (2002) studied the location of the zeros (q_1, q_2 etc.) separating the lobes for differentially rotating stars, assuming rotation laws similar to that observed on the Sun:

$$\omega(l) = \omega_0(1 - \alpha \sin^2 l), \quad (1)$$

with l the latitude and ω_0 the angular velocity at the equator. $\alpha = 0$ implies solid body rotation, $\alpha > 0$ equatorial acceleration (solar-like differential rotation; $\alpha_\odot = 0.20$) and $\alpha < 0$ polar acceleration.

Send offprint requests to: A. Reiners,
e-mail: areiners@hs.uni-hamburg.de

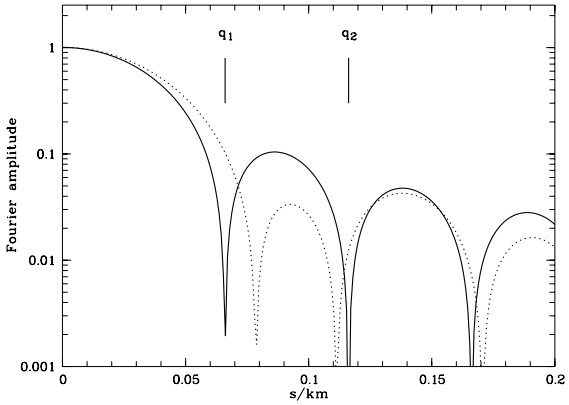

Fig. 1. Normalized Fourier transforms of rotationally broadened line profiles with $v_{\rm rot} = 10\,{\rm km\,s^{-1}}$ ($i = 90°$); rigid rotation ($\alpha = 0.0$; solid line) and differential rotation ($\alpha = 0.5$; dashed line) are shown. Zero positions q_1 and q_2 of the solid line are marked.

Reiners et al. (2002) specifically showed that the ratio q_2/q_1 can be used to determine the value of α. In Fig. 2 the dependence of q_2/q_1 on α and on the inclination angle i is plotted in grayscale (from black to white, values of q_2/q_1 from 1.3 to 2.0 are shown). In the considered case a linear limb darkening law with a limb darkening parameter $\epsilon = 0.6$ was used. The correct choice for ϵ is only poorly known and three lines of constant q_2/q_1 according to different values of ϵ but constant $\alpha = 0.0$ are overplotted. The dashed line represents q_2/q_1 for $\epsilon = 0.6$, the value expected for the Sun; solid lines indicate the values due to extreme ($\epsilon = 1.0; q_2/q_1 = 1.83$, left line) and no limb darkening ($\epsilon = 0.0; q_2/q_1 = 1.72$, right line).

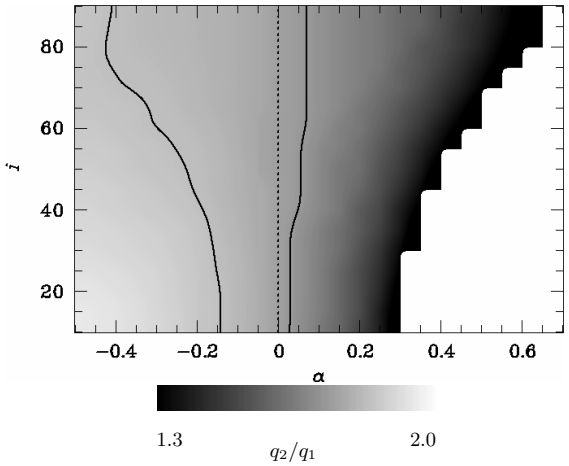

Fig. 2. Dependence of the measured ratio q_2/q_1, which is sensitive to differential rotation, on the inclination angle i and the amount of differential rotation (α). q_2/q_1 is greyscaled with values from 1.3 (black) to 2.0 (white). Three lines at constant q_2/q_1 are plotted for $\alpha = 0.0$; solid lines show $q_2/q_1 = 1.83$ ($\epsilon = 1.0$), $q_2/q_1 = 1.72$ ($\epsilon = 0.0$), the dashed line has constant q_2/q_1 at $\epsilon = 0.6$ (see text).

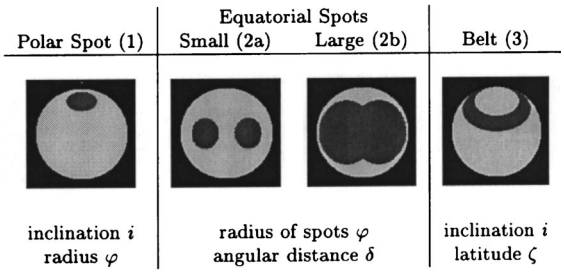

Fig. 3. The geometries of stellar spot distributions considered in this study and the varied parameters. (1) polar spot; (2) two spots on the equator seen under inclination $i = 90°$, the phase is chosen to obtain a symmetrical distribution; (3) a belt around the pole, thickness $h = 20°$.

Thus the region in between the solid lines is occupied by values that can be obtained by varying the limb darkening parameter ϵ of a rigidly rotating star ($\alpha = 0.0$), as well as by varying the differential rotation parameter α while leaving ϵ constant. As a consequence, this implies that values of q_2/q_1 outside the region bordered by the solid lines cannot be due to an undisturbed rigidly rotating stellar surface, regardless of the choice of ϵ.

In summary, measurements of $q_2/q_1 < 1.72$ indicate solar-like differential rotation ($\alpha > 0.0$), $q_2/q_1 > 1.83$ indicate anti-solar-like differential rotation ($\alpha < 0.0$). A value of $q_2/q_1 = 1.65 \pm 0.01$ was determined for ψ Cap (F5V) by Reiners et al. (2002), which has been interpreted as solar-like differential rotation ($\alpha = 0.15 \pm 0.1$). For a fast rotator like ψ Cap ($v \sin i = 42 \pm 1\,\mathrm{km\,s^{-1}}$) no differential effect of this strength would be expected and the question arises whether there are additional effects influencing the shape of the spectral lines and mimicking differential rotation. An obvious candidate are star spots. Star spots can be quite large in active stars and can change the gross features of the line profile. Rapid rotators in which differential rotation is least difficult to detect tend to be active stars and active stars tend to have spots. The purpose of this paper is therefore to investigate whether star spots can mimic differential rotation effects in Fourier transformed line profiles.

2. Configurations of active regions

In any discussion of the influence of stellar surface structures on line profiles, two different cases must be distinguished from the observer's point of view; the projected configuration of spots on the stellar surface with respect to the axis of rotation is a) symmetric, or, b) it is asymmetric. In high quality spectra, asymmetric surface configurations lead to asymmetries in the line profiles. These asymmetries can easily be found by mirroring the profile at its center and comparing the original with the mirrored profile. Because the Fourier Transform Method (FTM) explained in Sect. 1 is only applicable to symmetric profiles, we must disregard any asymmetric profiles. This implies that the FTM is not suitable for stars showing asymmetric projections of the distributions of surface spots (that are large enough to affect the line profiles).

For the symmetric line profiles three different scenarios with spots are possible; 1) polar spots, 2) incidentally symmetric distributions of spots, 3) activity belts. Stellar surfaces with polar spots are often found in Doppler images, and their influence on the FTM will be discussed in Sect. 2.1. Incidentally, symmetric distributions include principally any spotted stellar surface that happens to yield to a symmetric projection towards the observer. These cases are considered in Sect. 2.2. Another symmetric configuration can occur if many spots are ordered on a belt around the rotational pole. This geometry is investigated in Sect. 2.3.

2.1. Polar spots

Indications for polar spots on the photospheres of cool stars have been found in a series of studies. Particularly, the Doppler imaging technique indicates that polar spots are quite frequent on the surfaces of G- and K-type stars (for an overview see e.g. Strassmeier 2001). Line profiles from stars with polar spots are affected in the line center. The surface configuration does not change with rotation and no modulation of the light curve can be seen either. Thus polar spots cannot be ruled out by the use of photometric or spectroscopic time series, and the only way to detect them is to compare the spectra with model profiles from unspotted stars.

It is not obvious whether polar spots affect line profiles and especially the Fourier transform in a similar way to

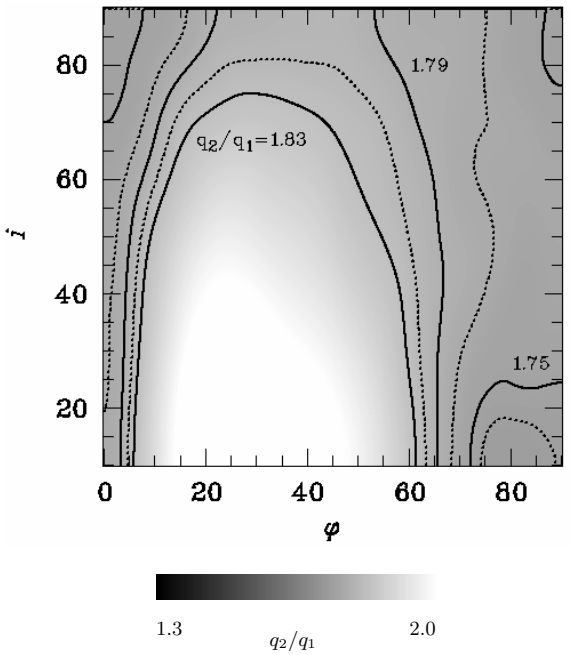

Fig. 4. Map of grayscaled q_2/q_1 according to a star with a cool polar spot of radius φ (in degrees), observed under inclination i. Grayscale of q_2/q_1 is the same as in Fig. 2. Contours indicate constant q_2/q_1 for $1.83 \geq q_2/q_1 \geq 1.75$ in steps of 0.02, the dashed line in the lower right corner is the same as in Fig. 2 (q_2/q_1 at $\alpha = 0.0$ and $\epsilon = 0.6$). Note that the line at $q_2/q_1 = 1.72$ does not appear; $q_2/q_1 > 1.72$ for all cases.

differential rotation. We therefore modelled a rigidly rotating star with one circular spot at the visible pole using the same modeling and transformation technique discussed in Reiners et al. (2001). The temperature of our model star is 5700 K, and we used a spot temperature of 4200 K, comparable to an average sunspot. Two parameters are varied in our study; a) the inclination i of the rotational axis to the observer's line of sight, b) the radius φ of the spot; φ is expressed in degree, i.e., a spot with a radius of $\varphi = 90°$ covers half the star (cf. Fig. 3).

An analysis identical to that discussed in Sect. 1 was carried out for the spotted star's spectra. We found that the shape of the Fourier transform does not fundamentally change by the introduction of a polar spot, and that the characteristic sidelobe structure can be found in the Fourier transformed profiles of all of our model stars. The ratio q_2/q_1 was calculated and the results are shown in Fig. 4. The same lines of constant q_2/q_1 as used in Fig. 2 appear, and some additional contours are also plotted for readability. It appears that the dashed line, which represents that value of q_2/q_1 which is expected from a rigidly rotating star with a limb darkening parameter $\epsilon = 0.6$ without any spots, spans only a small part of the considered parameter space (lower right part in Fig. 4). A large part of the parameter space is covered by values of q_2/q_1 larger than 1.83 (which is marked with a solid line), the highest ratio q_2/q_1 that can be caused by limb darkening effects. The line at $q_2/q_1 = 1.72$ does not appear in Fig. 4, i.e. q_2/q_1 is always larger than 1.72.

Since the criterion for the detection of solar-like differential rotation in a Fourier transformed line profile is $q_2/q_1 < 1.72$, we conclude that polar spots cannot mimic solar-like differential rotation. Therefore polar spots cannot invalidate any search for solar-like differential rotation using FTM. On the other hand we found that a large region of the parameter space yields values of q_2/q_1 larger than 1.83. These values can also be due to anti-solar-like differential rotation (pole rotates faster than equator), but cannot be obtained from the spectrum of an unspotted rigidly rotating star. For rigidly rotating stars believed to occupy that region in Fig. 4, $q_2/q_1 > 1.83$ is a necessary condition for the existence of the polar spot. Thus it is possible in some cases to check the geometries suggested from Doppler Imaging.

2.2. Incidentally symmetric spot distributions

We can in principle not exclude the case that the observed characteristics of line profiles are due to incidental combinations of the spots' temperatures and spatial distributions. Almost arbitrary spot distributions on the stellar surface observed at a suitable phase of rotation might cause symmetric projections towards an observer.

Whether the symmetry of an observed stellar surface is due to a symmetric surface geometry or is only due to the projection at the time of observation can be tested by more observations. Observations at different rotational phases will vary if the surface distribution is asymmetric and thus these cases can be ruled out.

We carried out simulations for the case of two circular spots with identical sizes φ (in degrees), and with a distance $\delta < 180°$, describing an asymmetric geometry, but with the observational phase chosen to obtain a symmetric projection of this geometry (cf. Fig. 3). We varied the parameters φ and δ and calculated q_2/q_1 from the Fourier spectrum. The inclination angle is always set to $i = 90°$. Configurations with spot radii $\varphi \gtrsim 30°$ (case 2b in Fig. 3) have spot filling factors of >30% of the visible surface. Such large filling factors are unlikely due to spots. On the other hand such geometries would be comparable to hot spots at the poles, which are not considered here.

Some configurations implying spots with $\varphi \lesssim 30°$ do indeed lead to values of $q_2/q_1 < 1.72$ and thus mimic solar-like differential rotation (e.g., case 2a in Fig. 3 has $q_2/q_1 = 1.71$). For all of those models the distance between the two spots is $40° < \delta < 90°$, which means that two noticeable bumps emerge in the spectrum. Our calculations showed that perturbations of the undisturbed (rigidly or differentially) rotation profile, which are due to such spots, will be significant, if the signal to noise ratio is as high as needed for the detection of differential rotation.

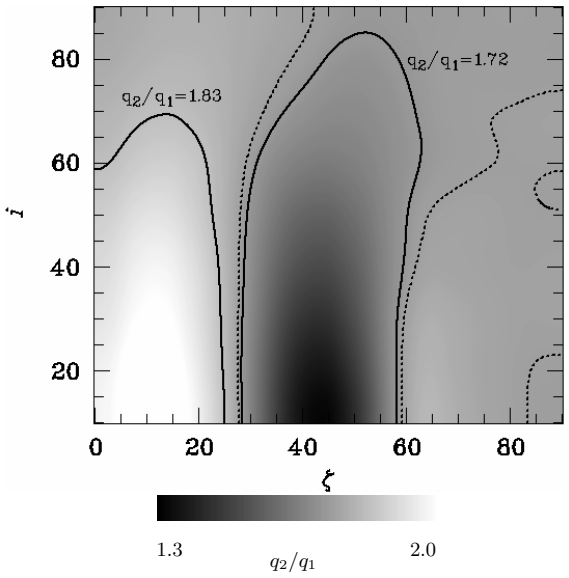

Fig. 5. Map of grayscaled q_2/q_1 according to a star with a cool belt of 20° width at latitude ζ (in degree), observed under inclination i. Grayscale of q_2/q_1 and overplotted lines of constant q_2/q_1 are the same as in Fig. 2.

Thus those "small" spots contained in the profile cannot be misinterpreted as differential rotation.

2.3. Activity belts

Besides polar spots there is a second symmetric distribution of active regions that one should consider. If in analogy to the solar case, active regions are placed at certain latitudes, one also can think of stars where these latitudes are to a high degree populated by spots. In these cases the spots might apparently merge to a belt of active regions around the star. We computed this configuration using a thickness of the belt of $h = 20°$ (cf. Fig. 3, case 3). The belt latitude ζ is varied between 0° (which is equivalent to a polar spot) and 90° (a belt around the rotational equator). The rotational axis is inclined under an arbitrary inclination angle i ($0° < i \leq 90°$). We show the q_2/q_1-map of this geometry in Fig. 5. The bright region at small values of ζ is comparable to the case of polar spots, because the belt is almost closed around the pole. For values of $30° < \zeta < 60°$, there is a region where $q_2/q_1 < 1.72$.

Taking a look at the Fourier transforms of the line profiles with $\zeta \gtrsim 50°$, it emerges that their shape differs strongly from shapes due to rigid or differential rotation. Those profiles would in practice not be attributed to differential rotation. On the other hand, activity belts with $30° < \zeta < 50°$ lead to profiles that can hardly be distinguished from rotational profiles. If additionaly the inclination angle has a value leading to $q_2/q_1 < 1.72$ (Fig. 5), such cases can mimic solar-like differential rotation using FTM.

3. Discussion and conclusions

A study on the influence of geometrical distributions of stellar spots on the search for solar-like differential rotation using FTM has been carried out. It is impossible to attribute small values of q_2/q_1 to a polar spot, a stellar surface feature that can be found on many Doppler images. Furthermore, the signature of a polar spot in stellar line profiles is similar to anti-solar-like differential rotation. Since we do not expect an anti-solar-like rotation law (i.e., an accelerated pole) for solar-like stars, it is possible to test the results from Doppler-imaged polar spots.

Our study of the influence of equatorial spots showed that with a signal-to-noise ratio needed for the detection of differential rotation, spots that might influence the Fourier transform will be detected directly in the line profile. Thus significant asymmetric spot distributions can be discerned, and they will not mimic an unspotted differentially rotating surface.

For the symmetric distributions a handful of configurations remain which indeed can mimic solar-like differential rotation. Since the incidental symmetric distributions are rather implausible, the only probable geometry is a large number of spots occupying a region along a certain latitude in a belt. At latitudes $30° < \zeta < 50°$ and certain inclination angles i (cf. Fig. 5) q_2/q_1 becomes smaller than 1.72, which is the indication of solar-like differential rotation. On the Sun a typical filling-factor of 0.2% is reached at the maximum of activity. The desired configurations have filling-factors of ∼8%. For the faster rotators that can be investigated with FTM this might not be unrealistic. In these cases time-series can be helpful; if the value of q_2/q_1 was dominated by a belt, and if we assume that those objects underly activity cycles similar to the Sun, q_2/q_1 in turn will change during a stellar cycle.

However, although indications for spots situated along activity belts do indeed exist (e.g., Barnes et al. 2001), the configurations are not sufficiently continuous to mimic an unspotted differentially rotating star. Thus we conclude that observed q_2/q_1 values cannot be attributed to surface spots and that the most probable interpretation of $q_2/q_1 < 1.72$ is that of solar-like differential rotation.

Acknowledgements. A.R. acknowledges financial support from Deutsche Forschungsgemeinschaft DFG-SCHM 1032/10-1.

References

Barnes, J. R., Collier Cameron, A., James, D. J., & Steeghs, D. 2001, MNRAS, 326, 1057
Gray, D. F. 1977, ApJ, 211, 198
Howard, R. 1984, ARA&A, 22, 131
Huang, S.-S. 1961, ApJ, 133, 130
Reiners, A., Schmitt, J. H. M. M., & Kürster, M. 2001, A&A, 376, L13
Reiners, A., & Schmitt, J. H. M. M. 2002, A&A, 384, 155
Schou, J., Antia, H. M., Basu, S., et al. 1998, ApJ, 505, 390
Strassmeier, K. G. 2001, 11th Cambridge Workshop on Cool Stars, Stellar Systems and the Sun, ed. R. J. García López, R. Rebolo, & M. R. Zapatero Osorio, ASP Conf. Ser., 223, 271

4.2 Poster presentation at the "1st Potsdam Thinkshop on Sunspots & Starspots", Potsdam (2002)

Poster Proceedings of the 1st Potsdam Thinkshop on Sunspots & Starspots", Potsdam (2002),
eds. K.G. Strassmeier, and A. Washuettl, p.5

1st Potsdam Thinkshop Poster Proceedings, p. 5–6

Spots or differential rotation?

A. REINERS and J.H.M.M SCHMITT

Hamburger Sternwarte, Gojenbergsweg 112, D-21029 Hamburg, Germany

Received *July 5, 2002*; accepted *July 5, 2002*

Abstract. Absorption line profiles of rotating stars can in detail be studied using the Fourier Transform Method (FTM). A differential rotation law as observed on the sun has an unambiguous influence on the Fourier transform of a rotationally broadened line profile. Differentially rotating stars also may have polar spots as suggested by Doppler Imaging results. Here we show how differential rotation and polar spots influence the profile simultaneously. The conditions mainly limiting the usage of FTM are the required high S/N ratio and the resolution of the data. We show what quality is needed to obtain a reasonable measurement of differential rotation.

Key words: observation techniques; stellar rotation

1. The Fourier Transform Method

Absorption line profiles of rotating stars can be studied in detail using the Fourier Transform Method (FTM). The Fourier transform of a rotationally broadened line profile can be characterized by some typical features; particularly the zero positions (q_1, q_2; cf. Fig. 1) are dominated by the rotational law and are not severely biased by other broadening mechanisms like turbulence or limb darkening (Reiners et al. 2002a). A differential rotation law as observed on the sun ($\omega(l) = \omega_0 - \omega_1 \sin^2 l; \alpha = \omega_1/\omega_0$) has an unambiguous influence on the ratio q_2/q_1; differential rotation can be measured from only one high quality spectrum.

Reiners et al. (2002a) showed how to determine stellar differential rotation with respect to its inclination by measuring q_2/q_1. It turned out that a ratio of $q_2/q_1 < 1.72$ is a direct indication for solar-like differential rotation (equator faster than pole) and that $q_2/q_1 > 1.83$ can be assigned to anti solar-like differential rotation (pole faster than equator). The region in between is occupied by values possibly due to limb darkening effects. Stars within this region show little or no differential rotation. In Reiners et al. (2002b) the influence of spots and spot configurations has been studied; polar spots like those found by Doppler Imaging (e.g., Strassmeier 2001) cause larger values of q_2/q_1. Thus measurements of $q_2/q_1 > 1.83$ are likely due to spots and cannot be assigned to anti solar-like differential rotation. Other spot configurations in general lead to asymmetries in the profiles and q_2/q_1 cannot be obtained from such spectra.

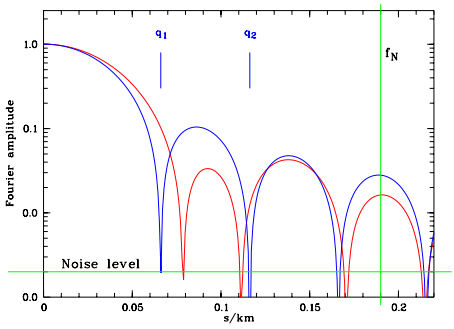

Fig. 1. Fourier transform of a rotationally broadened line profile (blue: solid ration; red: differential rotation with $\alpha > 0.0$). Zero positions q_1 and q_2 are sensitive to differential rotation. In order to measure q_2/q_1, the second sidelobes' maximum must be smaller than f_N and its amplitude must lie above the Noise Level.

Differentially rotating stars may also have polar spots; in this study we show how differential rotation and polar spots simultaneously influence q_2/q_1. The factors mainly limiting the usage of FTM are the required high S/N ratio and the resolution of the data. We study the data quality needed to obtain a reasonable measurement of q_2/q_1; our simulations follow the strategy outlined in Reiners et al. (2002a) and are based on a surface integration over about 25 500 visible grid points.

Correspondence to: areiners@hs.uni-hamburg.de

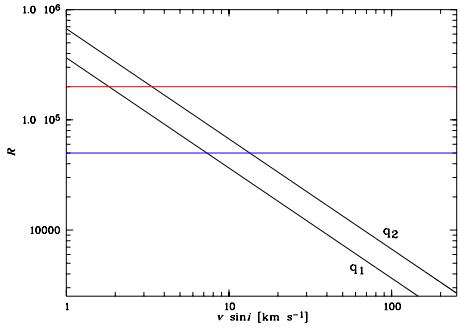

Fig. 2. Resolution R required to measure q_2 and q_1 with respect to $v \sin i$ of the star. To detect the second sidelobe and to avoid aliasing the resolution should be somewhat higher.

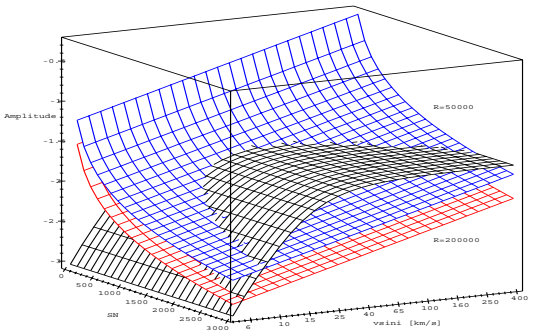

Fig. 3. Noise level and amplitude of the second sidelobe with respect to S/N of the data and $v \sin i$ of the star. The noise level in Fourier domain depends on the resolution and is shown for cases of $R = 50\,000$ (blue) and $R = 200\,000$ (red).

2. Data quality

For measuring the ratio q_2/q_1 two limitations exist:

1. The resolution R determines the Nyquist frequency $f_{\rm N} = 1/(2\Delta x)$ of the Fourier transform; no frequency higher than $f_{\rm N}$ can be obtained. To detect the second zero of the Fourier transform, it must be situated at a frequency lower than $f_{\rm N}$. Since q_2 scales with $v \sin i$, the limiting resolution depends on the projected rotational velocity of the star. Fig. 2 shows which resolution is required in order to detect the first (second) zero q_1 (q_2) for a star with given $v \sin i$.

2. The signal-to-noise ratio determines the noise level in the Fourier domain (assumed to be white, i.e., constant noise at all frequencies). For the detection of the second zero the amplitude of the second sidelobe must be significantly higher than the noise level. For high values of $v \sin i$ this value is at about -1.5 for a normalized Fourier transform. In the case of slow rotators (or small inclination angles) this amplitude drops due to the various broadening mechanisms. Fig. 3 shows the amplitude of the second sidelobe with respect to a turbulence velocity of $5\,{\rm km\,s^{-1}}$ (black curve) and the noise level for stars with given $v \sin i$ observed with a given S/N ratio for two resolutions $R = 50\,000$ (blue curve), $R = 200\,000$ (red curve).

3. Spots and differential rotation

While a ratio of q_2/q_1 less than 1.72 is an indication for solar-like differential rotation, a ratio larger than 1.83 can be due either to anti solar-like differential rotation or to polar spots. Since we do not have analytical formulae to investigate the interference of both effects, it remains unclear what happens if a differentially rotating star also has polar spots. To investigate this situation we modeled a differentially rotating, spotted star with parameters r (radius of polar spot) and α (differential rotation). Maps of q_2/q_1 are shown for four different inclination angles (i = 90°, 70°, 50°, 30°) in Fig. 4.

From Fig. 4 it is clear that for large inclination angles (i=90°, i=70°) the ratio q_2/q_1 is almost a linear combination of the effects of α and r known from the previous simulations of these parameters alone (Reiners et al. 2002a, 2002b);

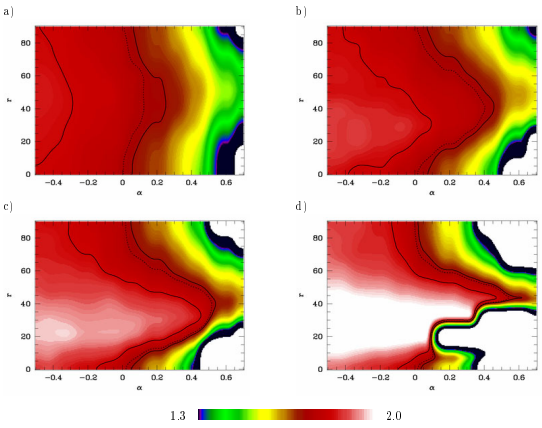

Fig. 4. Value of q_2/q_1 for different values of spot size r (in degree) and differential rotation α; inclination angle is a) 90°, b) 70°, c) 50°, d) 30°. Solid lines mark $q_2/q_1 = 1.72$ and 1.83; solid rotation can be assumed within this region.

spots with a radius of about 30° have the largest influence on q_2/q_1. For small inclination angles a non-linear behaviour of the parameter combinations can be seen; especially the combination of α and r where the first sidelobe vanishes is erratic.

However, the central result of our study is that the presence of a polar spot can hide the signatures of differential rotation in the Fourier profile. On the other hand, no cases have been found where an interference of both mechanisms mimics differential rotation in case of a solid rotator. Thus differential rotation remains the sole reasonable cause of measured values of $q_2/q_1 < 1.72$.

References

Reiners A., Schmitt J.H.M.M., 2002a, A&A, 384, 155
Reiners A., Schmitt J.H.M.M., 2002b, A&A, accepted
Strassmeier K.G., 2001, ASP Conf. Ser. 223: 11th Cambridge Workshop on Cool Stars, Stellar Systems and the Sun, ed. R.J. García López, R. Rebolo, M.R. Zapatero Osorio, p. 271

Chapter 5

Differential rotation in a larger sample of cool stars

5.1 Poster presentation at the IAU Symp. No. 210 “Modelling of Stellar Atmospheres”, Uppsala (2002)

to appear in PASP Conference Series

Modelling of Stellar Atmospheres
IAU Symposium, Vol. xxx, xxxx
N. E. Piskunov, W. W. Weiss, D. F. Gray, eds.

Differential rotation in a larger sample of cool stars

A. Reiners[1] and J.H.M.M. Schmitt

Hamburger Sternwarte, Gojenbergsweg 112, 21029 Hamburg

Abstract. Using the Fourier Transform Method (FTM) it is nowadays possible to detect stellar differential rotation in a single high quality spectrum. Detection of the subtle effects requires very accurate broadening profiles. With a "Physical Least Squares Deconvolution" process the template and broadening profiles of a large sample of F-, G- and K-dwarfs have been obtained in order to search for differential rotation. The accuracy of the fits is shown here. We report nine significant detections of stellar differential rotation and show the importance of the rotational law for an accurate line profile fit.

1. Effects of differential rotation in line profiles

Differential rotation invokes subtle effects on the line profiles that can be detected using the Fourier Transform Method (Reiners et al. 2002a). In Fig. 1 an absorption profile is shown for the case of solid rotation (black) and for differential rotation with a rotation law analogous to the solar case. To detect differential rotation the spectra need to have very high resolution and S/N, and the profiles must not be dominated by spots (Reiners et al. 2002b).

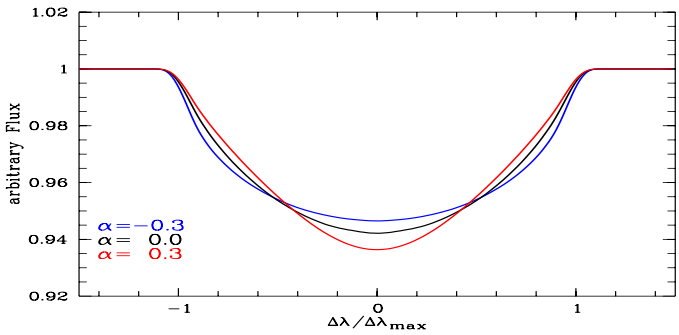

Figure 1. Absorption profile for the case of solid rotation (black) and for differential rotation with a rotation law analogous to the solar case; $\omega(l) = \omega_0(1 - \alpha \sin^2 l)$, $\alpha = 0.3$ (equator faster than pole, red line) and $\alpha = -0.3$ (pole faster than equator, blue line), l = latitude.

2. Physical Least Squares Deconvolution

In most cases the profile of a single absorption line is not sufficient to obtain a reliable measurement of differential rotation. Three reasons are:

1. The S/N-ratio of one single line is not high enough
2. Measurements from one line may be biased by systematic effects inherent in the line itself
3. Spectra of late type stars are severely blended and there is hardly a single isolated line

We thus extracted an overall broadening profile from wider regions of the spectra by deconvolving it with respect to an "unbroadened" template. Accurate positions and equivalent widths of the template's absorption lines are crucial for obtaining the broadening profile. We did not use a slowly rotating star with similar spectral type for the template because differences of, e.g., metallicity invoke critical deviations that may dominate our results. The process of the template's construction and deconvolution of the broadening profile is sketched in Fig. 2. After measuring the equivalent widths and line positions in a spectrum of a slowly rotating star of similar spectral type, an approximated broadening profile of the object is deconvolved using that template. The equivalent widths of the object's line profiles are fitted by deconvolving the template with the broadening profile fixed. In an iterative process the equivalent widths and the broadening profile are optimized.

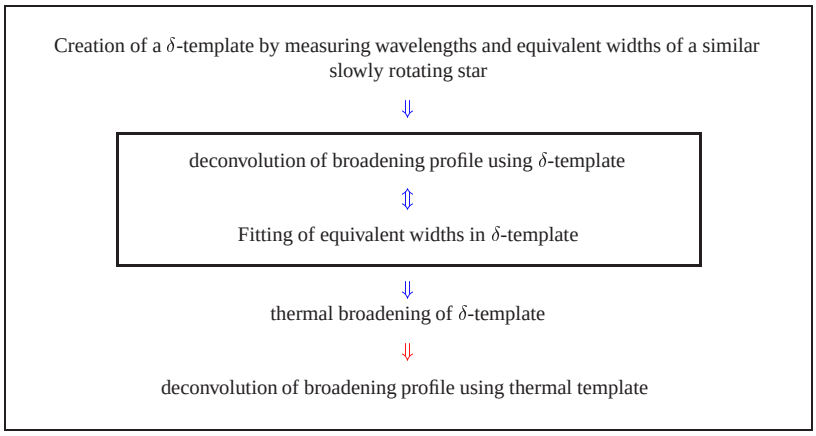

Figure 2. Process used to build the line template and to deconvolve the overall broadening profile.

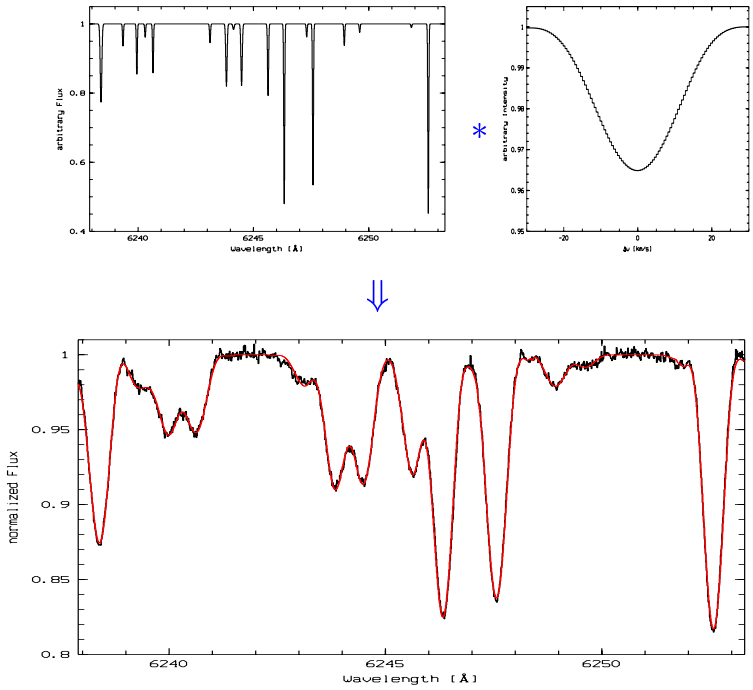

Figure 3. Example of the results of the Physical Least Squares Deconvolution. The physical (thermal broadened) template shown in the upper left figure is convolved with the achieved overall broadening profile (upper right). The result (red curve) is plotted over the original data in the bottom panel.

For the analysis of slowly rotating stars ($v \sin i < 20\,\mathrm{km\,s^{-1}}$) thermal broadening becomes important. We thus broadened each "δ-Peak" in our template according to the star's effective temperature and the atomic weight of the absorbing atom. With that template we deconvolve the final broadening profile used for the analysis. A typical example of the results is shown in Fig. 3, where the final template is again convolved with the final broadening profile.

3. Detections of differential rotation

Using the Fourier Transform Method (FTM) on stars with $v \sin i > 10\,\mathrm{km\,s^{-1}}$ it is not necessary to synthesize line profiles or broadening profiles due to, e.g., turbulence. The overall broadening profile is Fourier transformed and the indicators of differential rotation (zero positions of the Fourier transform, cf. Reiners et al. 2002a) can be measured directly. Thus it is possible to search for differential rotation in a large sample of stars.

We observed 142 F-, G- and K- dwarfs during three observing runs in 2000, 2001 and 2002 with the CES at the 3.6m telescope at ESO, La Silla ($R = 220\,000, S/N = 400...900$). 32 stars were found to be well suited for our analysis by means of $v \sin i$ and symmetry of the profiles. We found that 9 of the 32 stars show differential rotation with the equator rotating faster than the pole; for the most extreme case $\alpha/\sqrt{\sin i} = 0.42 \pm 0.07$ was derived.

In case of a large differential effect the profile deformation can be seen directly in the data. The derived profile (left) and a small spectral region (right) of the most extreme case, HD 173 667, are shown in Fig. 4 (upper panel). The red curve shows the result of the convolution of our template with the derived broadening profile. The blue curve shows the result of a convolution of the template with the theoretical broadening profile of a rigid rotator with the same value of $v \sin i$. Spectral regions of two other examples of strong differential rotation are plotted in the lower panel. In all examples the red curve excellently resembles the data and the differences between solid and differential rotation are pronounced.

In the example of HD 89 449 we also plotted the curves for solid rotation and extreme limb darkening coefficients (according to a linear limb darkening law). It can be seen that while the line center could also be fitted by a solid rotation law, the profile's flanks are too steep for all cases of limb darkening. Note that an anisotropic turbulence is incorporated in the solidly rotating models and that optimizing the turbulence can not improve the misfit between data and non-differential model.

We conclude that differential rotation severely alters the line profiles in a large fraction of cool stars, and that it has to be accounted for when modelling high resolution spectra of cool stars.

Acknowledgments. A.R. acknowledges financial support from Deutsche Forschungsgemeinschaft DFG-SCHM 1032/10-1.

References

Reiners A., Schmitt J.H.M.M., 2002a, A&A, 384, 155
Reiners A., Schmitt J.H.M.M., 2002b, A&A, 388, 1120

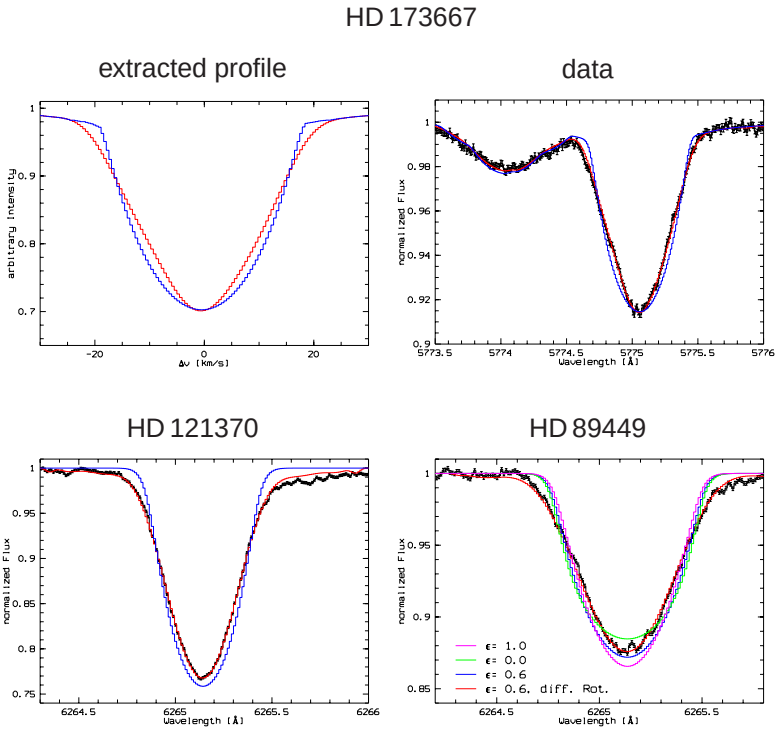

Figure 4. Three examples of differential rotation seen in the data; HD 173 667 (F6), HD 121 370 (G0) and HD 89 449 (F6). The red curves indicate the results of the convolution of the templates with the derived broadening profiles; blue curves are results of the convolution with broadening profiles according to rigidly rotating stars. For HD 89 449 curves for solid rotation and extreme limb darkening coefficient (according to a linear limb darkening law) are also shown.

Chapter 6

Evidence for strong differential rotation in Li-depleted fast rotating F-stars

6.1 A. Reiners, and J.H.M.M. Schmitt

Astronomy & Astrophysics, 393, L77 (2002)

A&A 393, L77–L80 (2002)
DOI: 10.1051/0004-6361:20021250

Astronomy & Astrophysics

Evidence for strong differential rotation in Li-depleted fast rotating F-stars⋆

A. Reiners[1] and J. H. M. M. Schmitt[1]

Hamburger Sternwarte, Universität Hamburg, Gojenbergsweg 112, 21029 Hamburg, Germany

Received 20 July 2002 / Accepted 23 August 2002

Abstract. We report the detection of strong differential rotation on ten fast rotating ($v \sin i > 10\,\mathrm{km\,s^{-1}}$) stars of spectral types F0–G0 using the Fourier Transform Method, in three cases we find $\alpha > 20\%$. Among the six differential rotators with $v \sin i > 15\,\mathrm{km\,s^{-1}}$, five have Li abundances of $\log \epsilon(\mathrm{Li}) < 1.5$, for one object no Li abundance is available to our knowledge. No differentially rotating star with high Li abundance was found, although the average Li abundance of fast rotators in the literature is $\log \epsilon(\mathrm{Li}) > 2.0$. Our results suggest that Li-depleted fast rotators tend to show differential rotation. Interpreting high rotational velocity as indicator of youth, this finding supports the idea of the connection between mixing processes and differential rotation during magnetic breaking in F-stars.

Key words. stars: abundances – stars: evolution – stars: rotation

1. Introduction

The detection of differential rotation on other stars or the Sun is a difficult observational task. Extensive measurements of photometric variability, migration of photosperic spots and deviations in the rotational profile have been carried out in order to detect its effects. Recently results of differential rotation measurements were reported using the Doppler Imaging technique (e.g., Donati & Collier Cameron 1997).

The main driver of this quest is the poor understanding of stellar dynamo theory, that is believed to be the primary source of all solar and stellar activity phenomena. An empirical dependence of differential rotation on fundamental stellar parameters can provide a key ingredient of stellar dynamo theory.

The results from Doppler Imaging lend support to theoretical studies of the dependence of latitudinal differential rotation on rotational frequency. Using a mean-field approach Kitchatinov & Rüdiger (1999) found that the rotational shear $\Delta\Omega$ is approximately constant in solar like stars for all rotational frequencies. Thus the relative amount of differential rotation,

$$\alpha = \frac{\Delta\Omega}{\Omega_0}, \qquad \Delta\Omega = \Omega_1 - \Omega_0, \tag{1}$$

with Ω_0 the angular velocity at the equator and Ω_1 at the poles, becomes less with faster rotation.

However, the rotational velocity plays an important role for the understanding of a second physical process taking place on stars, namely lithium depletion. Early measurements of Li abundances were believed to be due solely to the depth of the convection zone, but extensive observations during the last decades revealed that the Li depletion processes are much more complicated.

During the evolution on the main-sequence, F-stars undergo magnetic braking. Angular momentum transport induces radial differential rotation, thereby Li is transported in the deeper layers of the star that becomes Li-depleted (cf. Pinsonneault et al. 1989). After the phase of rotational breaking, at the end of the main sequence, a large spread in Li abundances is believed to represent the spread of initial angular momentum among those stars, although a similar initial Li abundance is assumed. Observations of, e.g., Balachandran (1990) show that slowly rotating F-stars do have a large spread in Li abundances.

On the other hand, again assuming similar initial Li abundances, it is surprising that stars with high rotational velocities also show a spread in Li abundance, too. Those stars should be younger and mixing processes should not have depleted Li as expected for the old and slowly rotating stars. Balachandran (1990) showed that fast rotators are indeed mainly Li-rich but a few cases of fast rotating Li-depleted F-dwarfs were also found. Boesgaard & Tripicco (1986) pointed out, that despite the observed general trend of fast rotating Li-rich and slowly rotating Li depleted stars, they found some "misfits" with high $v \sin i$ but low $\log \epsilon(\mathrm{Li})$.

Our work connects the observational data of Li abundances with our measurements of latitudinal differential rotation. We focus on the "misfitting" group of fast rotating Li-depleted stars. A deeper examination of our measurements and

Send offprint requests to: A. Reiners,
e-mail: areiners@hs.uni-hamburg.de

⋆ Based on observations collected at the European Southern Observatory, La Silla.

Table 1. Observations.

Date	# Objects	Region	Resolution
13.10.2000	11	5770–5810 Å	235 000
01.–04.10.2001	62	5770–5810 Å	235 000
01.–03.04.2002	77	6225–6270 Å	235 000

correlations to other stellar parameters will be presented in a forthcoming paper.

2. Observations and data analysis

Our primary data sample consists of 142 F-, G- and K-dwarfs mostly brighter than $M_V = 6$ mag and visible at ESO La Silla, Chile. We concentrated on stars with known rotational velocity and $10\,\mathrm{km\,s^{-1}} < v \sin i < 40\,\mathrm{km\,s^{-1}}$, however, we also observed 30 stars without known rotational velocities.

With the Fourier Transform Method (FTM), differential rotation can be measured in stars with $v \sin i \gtrsim 10\,\mathrm{km\,s^{-1}}$ (cp., Reiners & Schmitt 2002a). The zero positions q_1 and q_2 of the Fourier transformed broadening profile are used to measure the differential rotation rate. For stars with lower rotational velocity, other line broadening effects become dominant and the measurement of q_2 is not reliable. To detect differential rotation on stars with $v \sin i < 20\,\mathrm{km\,s^{-1}}$, high resolution spectra of $R \geq 100\,000$ are needed. The data was taken with Ces at the ESO 3.6 m telescope at La Silla, Chile. In its highest resolution mode ($R = 235\,000$) the spectral region covers ∼40 Å. We used two different wavelength regions (5770–5810 Å and 6225–6270 Å) in the three observing runs listed in Table 1. For a detection of the subtle effects of differential rotation high S/N-ratios are essential. The S/N-ratio of our data is between 400 and 900 for all observations.

To measure differential rotation we extracted an overall broadening profile by a "Physical Least Squares Deconvolution" process. We constructed an unbroadened δ-template using a slowly rotating star of similar spectral type. Central wavelengths were optimized to correct for convective wavelength shifts. With that template as a starting point the equivalent widths of the individual lines and the broadening profile of the star were iterated. For line profiles of stars rotating as slowly as our sample stars, thermal broadening becomes important. Thus after the iteration we broadened the template lines according to the effective temperature of the star and the atomic weight of the absorbing atom. With that final template we deconvolved the final broadening profile.

The broadening profile was Fourier transformed and differential rotation was measured as described in Reiners & Schmitt (2002a). To show the quality of the deconvolution process, we convoluted the final template with the final broadening profile. The result is plotted over the error bars of the data points in Fig. 1.

3. Results

Of the 142 observed stars we found 80 objects rotating below $10\,\mathrm{km\,s^{-1}}$. As mentioned above it is not possible to derive

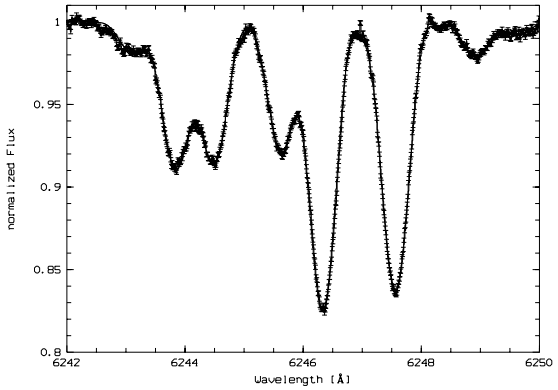

Fig. 1. Example of the quality of the deconvolution process. The convolution of the thermal broadened template with the derived broadening profile is plotted over the error bars of the data.

informations about differential rotation for these stars with our method. Data quality limited us to stars with $v \sin i > 12\,\mathrm{km\,s^{-1}}$, and five stars of our sample were multiple stars or showed peculiar line profiles and no reliable broadening profile could be derived for these cases. The remaining 53 stars can be sorted in two groups; 32 symmetric and 21 asymmetric profiles with respect to the error bars. The asymmetric ones are suspected to be mainly due to spots and flux variations within the photosphere. Thus the shape of the profile can be dominated by temperature variations and not by the rotational law. For this study we did not use those profiles and analyzed only the symmetric ones.

The remaining 32 stars are of spectral type F0 – G0. For their symmetric profiles with $v \sin i > 10\,\mathrm{km\,s^{-1}}$ the ratio of the first two zeros of the Fourier transform was calculated. Following Reiners & Schmitt (2002a), a ratio $q_2/q_1 < 1.72$ is a direct indication for solar-like differential rotation (equator faster than pole). $1.72 < q_2/q_1 < 1.83$ is typical for solid rotation with arbitrary limb darkening, and a value of $q_2/q_1 > 1.83$ indicates anti solar-like differential rotation (pole faster than rotator) or a polar spot (Reiners & Schmitt 2002b).

In Fig. 2 the distribution of the measurements of q_2/q_1 among the 32 profiles is shown. The region occupied by unspotted solid rotators is indicated by dashed lines. The majority of our objects (20 of 32) lie within that region. Ten of the 32 objects show significant differential rotation with $q_2/q_1 < 1.72$. Only two objects have $q_2/q_1 > 1.83$.

In the literature we found lithium abundances for 18 of the 32 analyzed stars. No lithium line lies within our spectral region and it was not possible to derive Li abundances for the remaining 14 objects. In Table 2 the parameters of the ten differential rotators and of the two stars with $q_2/q_1 > 1.83$ are shown.

In Fig. 3 we plot the Li abundances vs. q_2/q_1. Since the mentioned studies on connections between Li abundance and $v \sin i$ suggest that a large spread of Li abundances is common for stars with $v \sin i \lesssim 15\,\mathrm{km\,s^{-1}}$, and that fast rotators ($v \sin i \gtrsim 15\,\mathrm{km\,s^{-1}}$) are in general Li-rich, we divide our sample in two

Table 2. Stars with $q_2/q_1 < 1.72$ or $q_2/q_1 > 1.83$; i.e., not consistent with solid ration of an unspotted photosphere.

HD	HR	Type	$v \sin i$ [km s^{-1}]	q_2/q_1	log ϵ(Li)
89449	4054	F6IV	17.3 ± 1.7	1.44 ± 0.04	<1.10[a]
89569	4061	F6V	12.2 ± 0.7	1.57 ± 0.02	n.a.
100563	4455	F5V	13.5 ± 0.4	1.67 ± 0.04	2.66[c]
105452	4623	F0IV/V	23.5 ± 1.2	1.59 ± 0.02	n.a.
120136	5185	F7V	15.6 ± 1.0	1.57 ± 0.04	<0.60[d]
121370	5235	G0IV	13.5 ± 1.3	1.46 ± 0.03	<1.81[b]
160915	6595	F6V	12.4 ± 0.5	1.60 ± 0.03	2.26[c]
173667	7061	F6V	18.0 ± 2.0	1.40 ± 0.02	<1.37[b]
175317	7126	F5IV/V	17.1 ± 0.7	1.58 ± 0.04	<0.46[b]
197692	7936	F5V	41.7 ± 1.7	1.62 ± 0.02	<1.18[c]
23754	1173	F5V	13.8 ± 0.3	1.87 ± 0.05	n.a.
124850	5338	F7IV	15.0 ± 0.6	1.91 ± 0.04	< 1.21[a]

[a] Cutispoto et al. (2002).
[b] Balachandran (1990).
[c] Boesgaard & Tripicco (1986).
[d] Boesgaard & Lavery (1986).

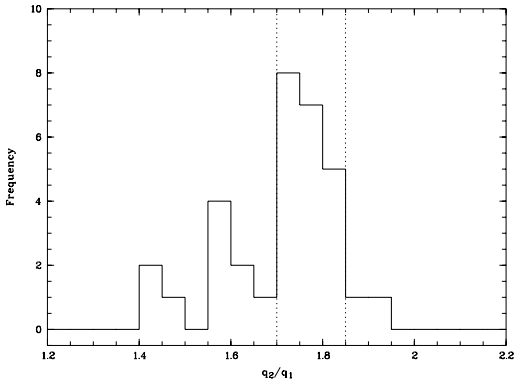

Fig. 2. Distribution of the ratio q_2/q_1 among the 32 analyzed profiles. The region between the dashed lines is occupied by solid rotators with arbitrary limb darkening coefficient according to a linear limb darkening law. $q_2/q_1 < 1.72$ indicates solar-like differential rotation, $q_2/q_1 > 1.83$ can be due to anti solar-like differential rotation or a polar spot.

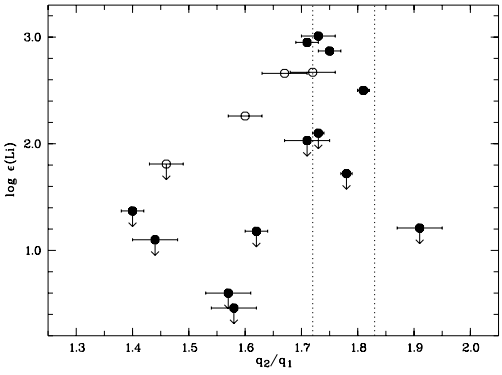

Fig. 3. Li abundance vs. q_2/q_1 for our sample stars, upper limits of Li abundances are marked with arrows, dashed lines as in Fig. 2. Open circles represent slow ($v \sin i < 15\,\mathrm{km\,s^{-1}}$), filled circles fast ($v \sin i > 15\,\mathrm{km\,s^{-1}}$) rotators. Two objects happen to have same values at $\log(\epsilon) = 2.5$, $q_2/q_1 = 1.81$. Note that the actual strength of differential rotation in terms of α or $\Delta\Omega$ is not simply a function of q_2/q_2, but that $q_2/q_1 < 1.72$ is always a direct indication for the presence of differential rotation.

subroups defined by $v \sin i = 15\,\mathrm{km\,s^{-1}}$. Stars with $v \sin i > 15\,\mathrm{km\,s^{-1}}$ are marked with full circles in Fig. 3, slower rotating stars with open circles. The region between the dashed lines is again consistent with solid rotation without spots.

Although, in agreement with stellar evolution theory, fast rotators tend in general to be Li-rich, a handful of Li-depleted fast rotators were found in observations by Boesgaard & Tripicco (1986) and Balachandran (1990).

In Fig. 3 it can be seen that we found five Li-depleted fast rotators with $q_2/q_1 < 1.72$ in our sample, while there is no differentially rotating Li-rich star with $v \sin i \geq 15\,\mathrm{km\,s^{-1}}$. For one fast differential rotator no Li-abundance is available to our knowledge. It should be mentioned that even for our whole sample of stars we find more Li-depleted than Li-rich differential rotators (six Li-poor vs. two or one Li-rich differential rotators, depending on whether we interpret $q_2/q_1 = 1.67 \pm 0.04$ on HD 100 563 as significant differential rotation).

Our sample of objects with measurable differential rotation and available Li abundances is rather small, but nevertheless we can determine the statistical significance of a correlation between differential rotation and Li depletion in our data.

In Table 3 the objects with $v \sin i > 15\,\mathrm{km\,s^{-1}}$ are sorted into subgroups defined by their Li abundance and measured value of q_2/q_1. Stars for which only upper limits of Li abundances are available have been qualified as Li-poor, neglecting the actual value of the upper limit. Stars with $q_2/q_1 < 1.72$ are qualified as differential rotators according to Reiners & Schmitt (2002a). We tested the null hypothesis on whether the obtained distributions of Li detections and upper limits for differentially and

Table 3. Subgroups of the fast rotators; $v \sin i > 15\,\mathrm{km\,s^{-1}}$.

	Li	
rotation	upper limit	detection
differential	5	0
rigid	3	5

rigidly rotating stars can be due to underlying identical population distributions. Using a χ^2-test (cf., Press et al. 1992) we found that the probability of obtaining our results from identical population distributions for differentially and solidly rotating stars is less than 2.4%, i.e., a correlation between Li depletion and differential rotation in our sample is significant on a $2.2\,\sigma$ level.

4. Conclusions

From our primary data sample of 142 F-, G-, and K-stars we excluded the profiles where it is impossible or unreliable to measure the subtle effects of the rotational law. Stellar velocity fields and data quality limited us to stars rotating faster than $12\,\mathrm{km\,s^{-1}}$. Dominant photospheric distortions make measurements of the ratio q_2/q_1 unreliable in stars with asymmetric profiles.

For symmetric profiles the possibility of significant influences of photospheric features on q_2/q_1 is discussed in Reiners & Schmitt (2002b) and can be neglected as a source of our differential rotation measurements. Reliable measurements were possible in 32 objects in the spectral range F0–G0.

From mean-field theory no significant differential rotation is expected for stars rotating faster than $v \sin i = 10\,\mathrm{km\,s^{-1}}$. The profiles of the majority of the sample stars (20 of 32; 63%) are consistent with solid rotation and an unspotted photosphere. Two cases are found with signatures of either anti solar-like differential rotation or a polar spot ($q_2/q_1 > 1.83$). However, in contrast to the predictions, significant effects of solar-like differential rotation ($q_2/q_1 < 1.72$) are detected in 10 of our 32 sample stars (31%), nine of them have $q_2/q_1 < 1.65$. We want to emphasize that for this study we concentrated on the question, if the stars show *any* signatures of differential rotation, regardless of its actual value of α or $\Delta\Omega$. However, from Fig. 6 of Reiners & Schmitt (2002a) we derive a value of $\alpha > 20\%$ for the three stars with $q_2/q_1 < 1.5$.

For 18 of the 32 analyzed objects Li abundances are available in the literature, making it feasible to search for connections between Li-depletion and evidence of differential rotation. Observations done by Boesgaard & Tripicco (1986) and Balachandran (1990) show a large spread in Li abundances for slow rotators, while stars with $v \sin i \gtrsim 15\,\mathrm{km\,s^{-1}}$ tend to be Li-rich. Nevertheless, a handful of Li-depleted fast rotating "misfits" were found in the mentioned works. It is this group of "misfits" we focused on. While Li-depletion seems to be a common phenomenon in slowly rotating stars and in good agreement with calculations (Pinsonneault et al. 1989), in fast rotators it is an exception.

In our sample Li measurements are available for five of the observed fast differential rotators ($v \sin i > 15\,\mathrm{km\,s^{-1}}$). As mentioned, no differential rotation is expected for these stars from theory. All of them have measured Li abundances of $\log \epsilon(\mathrm{Li}) < 1.5$, i.e., we can identify these stars with surprisingly strong evidence of differential rotation with a subgroup of the "misfits" in the works of Boesgaard & Tripicco (1986) and Balachandran (1990).

In statistical terms, the correlation of Li-depletion and presence of differential rotation in our sample of fast rotating F-stars is significant at a $2.2\,\sigma$ level. Under the assumption that the high rotational velocity of these objects is mainly due to their youth, this correlation lends support to the idea that during magnetic breaking differential rotation takes place on F-stars and that Li becomes depleted already before the star has spun down. We emphasize that in our limited sample other effects like, e.g., undetected binarity, could also be the reason for high rotational velocities. In such case differential rotation may reflect the higher evolutionary stage of older stars.

The derivation of the strength of differential rotation in terms of α and $\Delta\Omega$ and further correlations between stellar parameters like mass, metallicity and especially age may clarify the situation. This will be presented together with the other stars of our sample in a subsequent publication.

Acknowledgements. A.R. acknowledges financial support from Deutsche Forschungsgemeinschaft DFG-SCHM 1032/10-1.

References

Balachandran, S. 1990, ApJ, 354, 310
Boesgaard, A. M., & Tripicco, M. J. 1986, ApJ, 303, 724
Boesgaard, A. M., & Lavery, R. J. 1986, ApJ, 309, 770
Cutispoto, G., Pastori, L., de Medeiros, J. R., Tagliaferri, G., & Andersen, J. 2002, A&A, 384, 491
Donati, J.-F., & Cameron, A. 1997, MNRAS, 291, 1
Kitchatinov, L. L., & Rüdiger, G. 1999, A&A, 344, 911
Pinsonneault, M. H., Kawaler, S. D., Sofia, S., & Demarque, P. 1989, ApJ, 338, 424
Press, W. H., Teukolsky, S. A., Vetterling, W. T., & Flannery, B. P. 1992, Numerical Recipes in C (Cambridge Universtity Press), p.620 ff
Reiners, A., & Schmitt, J. H. M. M. 2002a, A&A, 384, 555
Reiners, A., & Schmitt, J. H. M. M. 2002b, A&A, 388, 1120

Chapter 7

Rotation and differential rotation in field F- and G-type stars

7.1 A. Reiners and J.H.M.M. Schmitt
accepted for publication in Astronomy & Astrophysics

Rotation and differential rotation in field F- and G-type stars⋆,⋆⋆

A. Reiners[1] and J.H.M.M. Schmitt[1]

Hamburger Sternwarte, Universität Hamburg, Gojenbergsweg 112, 21029 Hamburg, Germany
e-mail: areiners@hs.uni-hamburg.de

Received 6 October 2002 / Accepted 5 November 2002

Abstract. We present a detailed study of rotation and differential rotation analyzing high resolution high S/N spectra of 142 F-, G- and early K-type field stars. Using Least Squares Deconvolution we obtain broadening profiles for our sample stars and use the Fourier transform method to determine projected rotational velocities $v \sin i$. Distributions of rotational velocities and periods are studied in the HR-diagram. For a subsample of 32 stars of spectral type F0–G0 we derive the amount of differential rotation in terms of $\alpha = (\Omega_{\rm Equator} - \Omega_{\rm Pole})/\Omega_{\rm Equator}$. We find evidence for differential rotation in ten of the 32 stars. Differential rotation seems to be more common in slower rotators, but deviations from rigid rotation are also found in some fast rotators. We search for correlations between differential rotation and parameters relevant for stellar activity and show indications against strong differential rotation in very active stars. We derive values of ΔP and $\Delta\Omega$, which support a period dependence of differential rotation. Derived lap times $2\pi/\Delta\Omega$ are of the order of 20 d and contradict the assumption that constant lap times of the order of the solar one ($\sim$ 130 d) are the rule on stars which are thought to harbour magnetic dynamos.

Key words. Stars: rotation – Stars: late-type – Stars: activity

1. Introduction

Stellar surface phenomena are driven by a variety of different forces. Gradients of temperature and gravity together with different ionization stages determine the depth of surface convection zones. Stellar rotation implies results in Coriolis forces that interact with turbulent fluid motions. Especially interesting are the processes taking place in the presence of magnetic fields; differential rotation is expected to wind up magnetic field lines and to maintain a stellar dynamo. Such dynamos are believed to be the cause of the plethora of all activity phenomena like, e.g., spots, chromosperic CaII emission, X-ray emission and activity cycles. As a consequence stars are generally not expected to rotate rigidly and different kinds of rotation laws can be imagined even in the absence of magnetic fields.

The only direct evidence for differential rotation comes from spatially resolved observations of the Sun; the solar rotation law can be approximated as

$$\Omega(l) = \Omega_{\rm Equator}(1 - \alpha \sin^2 l), \quad (1)$$

with l being the latitude and $\alpha_\odot \approx 0.2$, i.e., the Equator rotating 20% faster than the Pole.

Stellar differential rotation cannot be directly measured. Three main methods have been used for the search for deviations from rigid rotation on stars other than the Sun. (i) Variations of photometric periods, e.g., in chromospheric CaII emission (Donahue et al. 1996) or broadband photometry (Hall 1991). (ii) Identifying individual features on Doppler maps and follow their migration with time (e.g., Donati & Collier Cameron 1997; Barnes et al. 2000). (iii) Studying line profiles (Gray 1977, 1982; Wöhl 1983; Reiners et al. 2001). In this paper we will pursue method (iii).

Searching for non-rigid rotation using method (iii), it is crucial to disentangle the different stellar velocity fields. Realizing this, Gray (1973) examined the Fourier transform of stellar absorption profiles. Utilizing the fact that convolutions become multiplications in Fourier domain, he showed that velocity fields like micro- and macroturbulence and especially rotation are indeed distinguishable in the Fourier domain. However, no examples of non-rigid rotation were found among A-type (Gray 1977) and F-type (Gray 1982) stars.

For a determination of the rotation law the zeros of the Fourier transformed broadening profile are of particular interest. The ratio of the first and second zeros is a direct indicator for solar-like differential rotation (Reiners

Send offprint requests to: A. Reiners

⋆ Based on observations collected at the European Southern Observatory, La Silla

⋆⋆ Tables 3 and A1 are also available at the CDS via anonymous ftp to cdsarc.u-strasbg.fr (130.79.125.5) or via http://cdsweb.u-strasbg.fr/Abstract.html

Table 1. Observations

Date	# Objects	Region	Resolution
13.10.2000	11	5770–5810 Å	235 000
01.–04.10.2001	62	5770–5810 Å	235 000
01.–03.04.2002	77	6225–6270 Å	235 000

& Schmitt 2002a), i.e., $\alpha > 0$; equatorial regions rotate faster than polar ones. The important point is that the zeros of a Fourier transform are unaffected by convolutions with other velocity profiles. As long as other line broadening effects do not introduce additionally zeros – and convolutions are appropriate approximations of the superposition of the different velocity fields – the rotation law can be directly measured in the Fourier transform of stellar absorption profiles without any need of modelling.

In the present paper we apply the Fourier transform method (FTM) to a sample of late type stars with moderate rotational velocities ($v \sin i \leq 45\,\mathrm{km\,s^{-1}}$). We derive projected rotational velocities $v \sin i$ for all of our sample stars. The measurement of differential rotation in terms of α is possible only for a subsample (Sect. 3); for an overview on the method and the required data quality we refer to Reiners & Schmitt (2002a,b). We present a relation between the observable ratio of the zero positions in Fourier domain and the differential rotation parameter α on the basis of model calculations. Finally, we search for correlations between our derived values of α and other stellar parameters, focusing on those believed to be relevant for stellar activity.

2. Observations

Our primary data sample consists of 142 F-, G- and K-dwarfs visible from ESO La Silla, Chile. Histograms in visual magnitude and $B - V$ colour characterizing our sample are shown in Fig. 1. We concentrated on stars with known rotational velocity in the range $10\,\mathrm{km\,s^{-1}} < v \sin i < 40\,\mathrm{km\,s^{-1}}$. However, we also observed 30 stars without known rotational velocities.

The data was taken with CES at the ESO 3.6m telescope at La Silla, Chile. In its highest resolution mode ($R = 235\,000$) the spectral region covers ~ 40Å. In the three observing runs listed in Table 1 we used two different wavelength regions at $5770 - 5810$ Å and $6225 - 6270$ Å. For a detection of the subtle effects of differential rotation high S/N-ratios are essential. The S/N-ratios of our data range between 400 and 900 for all observations. As an example of the quality of our data we show two spectra in the region $6225 - 6270$ Å in Fig. 2. To study the effects of different wavelength regions, seven stars were observed both in the $5770 - 5810$ Å and in the $6225 - 6270$ Å regions. ψ Cap was observed in both runs where the $5770 - 5810$ Å region was used.

3. Extraction of the broadening profiles and the Fourier Transform Method

With the Fourier Transform Method (FTM), differential rotation can be measured in stars with $v \sin i \gtrsim 10\,\mathrm{km\,s^{-1}}$ (for an introduction to the method see Reiners & Schmitt 2002a,b). For stars with lower rotational velocity other line broadening effects become dominant and the measurement of differential rotation is not reliable. For the slowest rotators with narrow spectral lines high resolution is required. To detect differential rotation on stars with $v \sin i < 20\,\mathrm{km\,s^{-1}}$, spectra with a resolution of $R \geq 100\,000$ are needed.

To measure the subtle effects of differential rotation on the blended spectral lines it is necessary to achieve extremely high S/N-ratios. Therefore we extract an overall broadening profile for each star using as many absorption lines as possible by carrying out a "Physical Least Squares Deconvolution" (PLSD) process: We constructed an unbroadened δ-template using a slowly rotating star of similar spectral type as a reference. Line positions are compared with data from the Vienna Atomic Line Database (Kupka et al. 1999) and only well determined lines are used. Central wavelengths were optimized on the reference spectrum to correct for convective wavelength shifts. With such a template as a starting point we fitted the convolution of the template and a broadening profile to the data by alternately optimizing the equivalent widths of the individual template lines and the shape of the broadening profile. The broadening profile was parameterized using Chebychev polynomials. 25 polynomials were used to allow for small-scale variations. For line profiles of stars rotating as slowly as our sample stars thermal broadening becomes important. Thus after the iteration we broadened the template lines according to the effective temperature of the star and the atomic weight of the absorbing atom. With that template we finally deconvolved the overall broadening profile.

In order to provide an impression of the quality of our broadening profiles, we convolved the final template with the final broadening profile. Some results can be seen in the top panel of Fig. 2 and in Figs. 10 (b, d, f). Solid lines indicate the results of the convolutions that are plotted over the error bars of the data. Especially in Fig. 2 the quality of the fit over the whole spectral region is apparent.

Our sample also contains a number of spectroscopic binaries and stars with peculiar profiles for which no broadening profiles could be derived. Those spectra have been discarded and no measurement of differential rotation was possible for them. For the slowest rotators ($v \sin i \lesssim 6\,\mathrm{km\,s^{-1}}$) no useful derivation of a broadening profile was possible either. Since no differential rotation can be derived for those stars anyway, we calculated the projected rotational velocity $v \sin i$ from a mean profile of the absorption lines due the heaviest ions with the smallest intrinsic widths. Each absorption line used is transformed into velocity space and the results are co-added.

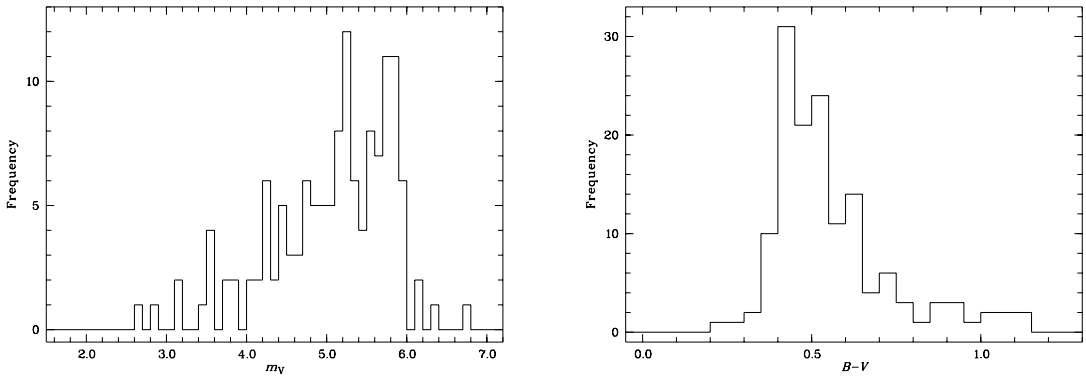

Fig. 1. Distributions of our primary data sample of 142 F-, G- and K-stars in apparent magnitude (m_V, left) and $B-V$ colour (right).

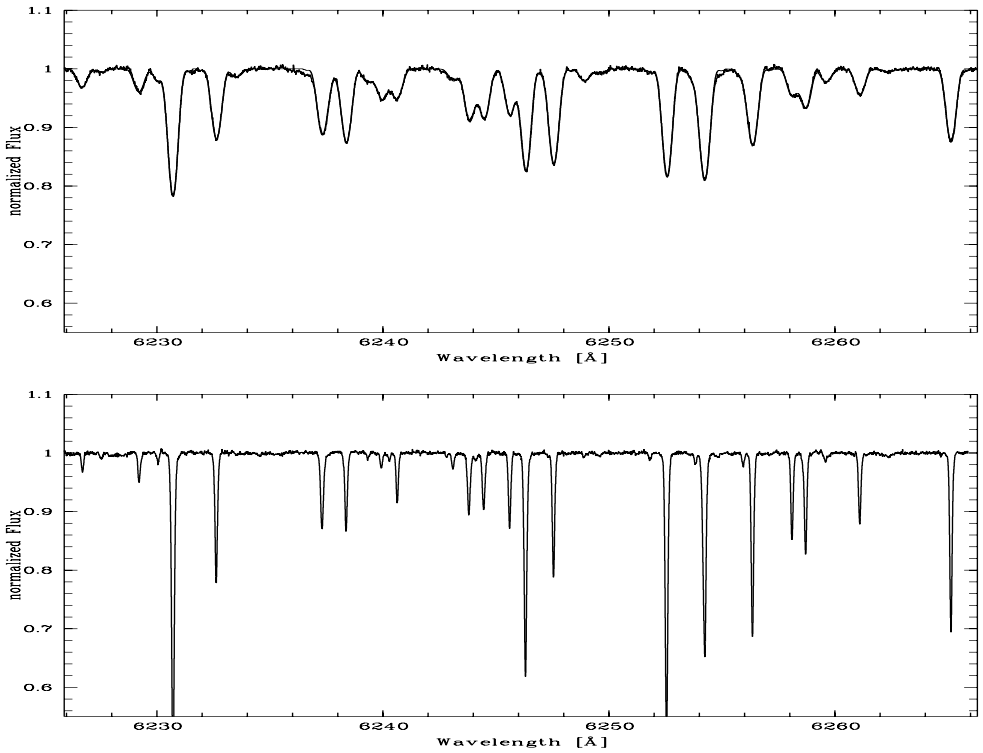

Fig. 2. Two spectra in the region 6225–6270 Å. Top panel: The "fast" rotator HD 89 449 ($v \sin i = 17.4\,\mathrm{km\,s^{-1}}$). The convolution of our derived broadening profile and the optimized line template is overplotted (cf. Sect. 3); bottom panel: Slow rotator HD 76 932 ($v \sin i = 2.6\,\mathrm{km\,s^{-1}}$). For the slow rotators no broadening profile was derived and only the data is plotted here.

The value of $v \sin i$ was then derived from that mean profile (see Sect. 4).

If the derivation of an overall broadening profile is successful, peculiarities like asymmetries or spectroscopic duplicity of the stars can easily be found given the obtained quality of the profile. For the detection of differential rotation with FTM profile symmetry is essential, since large-scale turbulence or photospheric distortions like spots can seriously disturb the signal of the underlying rotational broadening profile. Before Fourier transform apparently symmetric profiles of the fast rotators have been tested for asymmetry by mirroring the profiles at the center and

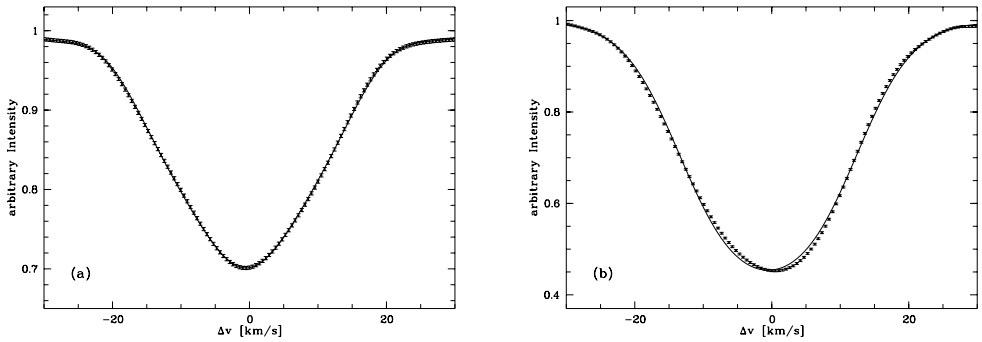

Fig. 3. Example of (a) a symmetric (HD 173 667) and (b) an asymmetric (HD 98 991) broadening profile. The symmetrized broadening profiles are plotted over the error bars of the data (see text).

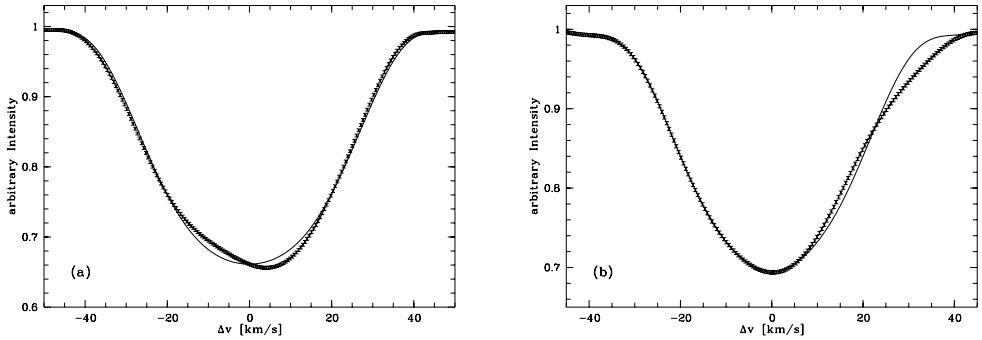

Fig. 4. Asymmetric mean profiles of (a) HD 118 646 and (b) HD 110 379. In (a) the line core is strongly asymmetric (the symmetrized broadening profiles is plotted over the data). In (b) the core is symmetric and the blue and red flank differ, here we mirrored the broadening profile at the line center and plotted the mirrored profile over the data.

taking the average of both prototypes. We qualified a profile as symmetric if the averaged profile falls completely within the error bars of the original line. Examples of symmetric and asymmetric profiles are shown in Figs. 3 and 4.

The symmetric broadening profiles are Fourier transformed and the first two zeros, q_1 and q_2, of the Fourier transform are measured. Both the projected rotational velocity $v \sin i$ and the differential rotation parameter α – assuming a solar-like rotation law – are determined by the zeros of the Fourier profiles. The absolute positions of the zeros are determined by the value of $v \sin i$ (see Sect. 4), and the rotational broadening law defines the ratio q_2/q_1 as shown in Reiners & Schmitt (2002a) (see Sect. 6).

For slowly rotating stars the signal vanishes in the noise and q_2 cannot be measured. In addition to the principal limit of detecting differential rotation with FTM to stars with projected rotational velocities of $v \sin i \gtrsim 10\,\mathrm{km\,s^{-1}}$ an additional threshold due to the limited S/N-ratio is inferred. Calculations of that limit can be found in Reiners & Schmitt (2002c), in our case the limit applies at about $v \sin i \gtrsim 12\,\mathrm{km\,s^{-1}}$.

No asymmetries are expected in the profiles from rotationally line broadening and for our determination of the rotational law only the real Fourier components can be used. Thus we averaged out small asymmetries in the profiles as explained above and used the averaged profile to calculate the Fourier transform. Simulations showed that the asymmetries we allow in our procedure lead to deviations in q_2/q_1 that are well contained within the calculated errors due to limited S/N-ratio.

In case of asymmetry we transformed the original unsymmetrized broadening profile and determined only the projected rotational velocity $v \sin i$, a procedure that is relatively stable against asymmetries within the lines. No value of q_2/q_1 was calculated for asymmetric profiles. For seriously blended spectra of, e.g., binaries we selected single lines and calculated $v \sin i$ directly from the spectra.

Note again that no modeling of the data was undertaken for each star – we derive the value of differential rotation from comparing the ratio q_2/q_1 with results from models shown in Reiners & Schmitt (2002a).

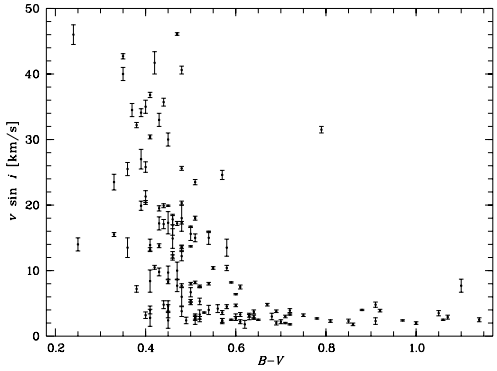

Fig. 5. Projected rotational velocities $v \sin i$ of the 142 stars of our primary sample. The exception from the slope consistent with magnetic braking at $B-V = 0.79$ is the RS CVn HD 155 555.

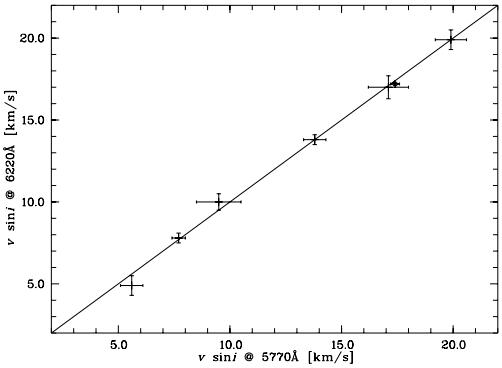

Fig. 6. Projected rotational velocities $v \sin i$ for the seven objects observed in the two regions between 5770 – 5810 Å and 6225 – 6270 Å. Good agreement between the two regions can be seen. The value at $v \sin i = 5\,\mathrm{km\,s^{-1}}$ is calculated only from q_1 and has a larger uncertainty.

4. Rotational velocities

The zeros σ_n of the Fourier transformed line profile from a rigidly rotating star with a linear limb darkening parameter ϵ scale with the projected rotational velocity $v \sin i$ (Dravins et al. 1990) as follows:

$$\sigma_n = q_n / v \sin i \quad (2)$$

$$q_1 = 0.610 + 0.062\epsilon + 0.027\epsilon^2 + 0.012\epsilon^3 + 0.004\epsilon^4 \quad (3)$$

$$q_2 = 1.117 + 0.048\epsilon + 0.029\epsilon^2 + 0.024\epsilon^3 + 0.012\epsilon^4 \quad (4)$$

Thus we determine the value of $v \sin i$ from the zero positions q_2 and q_1 of the Fourier transformed broadening profile. Our values of $v \sin i$ are calculated for a limb darkening parameter $\epsilon = 0.6$. For stars with a value of $v \sin i \lesssim 12\,\mathrm{km\,s^{-1}}$, the second zero q_2 cannot be measured since the signal vanishes in the noise at the relevant frequencies. In those cases $v \sin i$ was measured from the first zero only. For very low projected rotational velocities ($v \sin i \lesssim 3\,\mathrm{km\,s^{-1}}$) even determining the first zero q_1 can be difficult and measurements must be interpreted as upper limits.

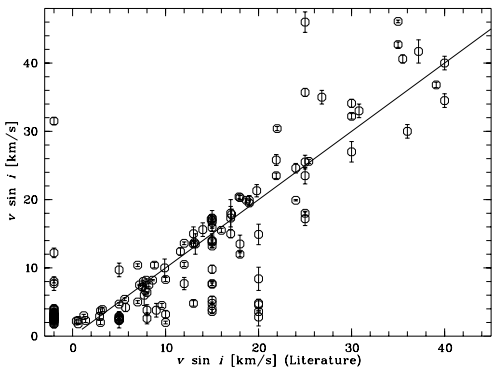

Fig. 7. Comparison of the calculated values of $v \sin i$ to the values in the literature (see text for references). Values of $v \sin i < 20\,\mathrm{km\,s^{-1}}$ are often upper limits in the other works and thus appear under the 1:1 line drawn for comparison. The 30 stars without values in the references are plotted at $v \sin i_{\mathrm{Lit.}} = -2\,\mathrm{km\,s^{-1}}$ for readability.

In case of rigid rotation, the calculation of $v \sin i$ by q_1 and q_2 lead to the same values of $v \sin i$. As shown in Reiners & Schmitt (2002a), for a star rotating differentially with the equator faster than the pole, q_1 becomes larger while q_2 becomes smaller. Thus, too small (large) a value of $v \sin i$ is calculated from q_1 (q_2) in the case of solar-like differential rotation. We took the mean of both results if both zeros were measured. Our simulations revealed that for a differentially rotating star this is a good approximation for the projected rotational velocity at the equator. In those cases we take as error on $v \sin i$ the maximum deviation to the specific values of $v \sin i$ calculated from q_1 and q_2 alone.

Our values of the projected rotational velocities $v \sin i$ are given in Table A.1 together with the stars' names and colours from Hoffleit & Warren (1991). If the measurements of $v \sin i$ are upper limits the values are marked with a "<". During our first observing run we also took a spectrum of the Sun by observing Jupiter's moon Ganymede. The spectrum was treated like the other spectra, and for the projected rotational velocity of the Sun we obtained a value of $v \sin i < 2.1\,\mathrm{km\,s^{-1}}$, consistent with the actual value of $1.8\,\mathrm{km\,s^{-1}}$.

The derived values of $v \sin i$ for the stars of our primary sample are shown vs. $B-V$ colour in Fig. 5. A decline in $v \sin i$ consistent with rotational braking is apparent around $B-V \approx 0.3$. The only exceptions at $B-V = 0.79$ is member of an RS CVn system. For seven stars of our sample we have spectra in both wavelength regions between 5770 – 5810 Å and 6225 – 6270 Å. A comparison of the derived values of $v \sin i$ is shown in Fig. 6; a good

Table 2. Stars with peculiar or asymmetric profiles

HD	M_V^a	$T_{\rm eff}^a$	PLSD	Comment
2726	2.57	7028		extremely weak lines, SB?
3302	3.01	6463	√	
8556	3.27	6565	√	
25570	2.68	6686	√	
40136	2.88	6943	√	
57749	0.18	6875		SB
58728	3.12	6451		SB (with different $v \sin i$'s)
98991	2.37	6463	√	
99285	2.04	6568	√	
104827	1.82	7535	√	center
110379	3.54	7683	√	flank
113848	2.82	6581	√	center
114642	2.69	6255	√	
118646	2.58	6618	√	center
123999	2.99	6118		SB
128898	3.12	7847	√	
144069			√	flank
153363	3.25	6697	√	
155555	3.89			fast RS CVn
156897	3.11	6645	√	
160032	2.98	6500	√	flank
160910	2.66	6615	√	
176303	2.59	5959	√	
186185	2.57	6390	√	center
199684	2.96	6695	√	
220729	3.01	6699	√	

[a] calculated from $uvby\beta$ photometry (see Sect. 7), data from Hauck & Mermilliod (1998)

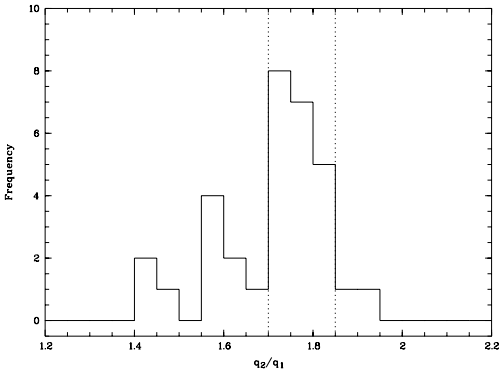

Fig. 8. Distribution of the ratio q_2/q_1 among the 32 analyzed profiles. The region between the dotted lines is occupied by solid rotators with arbitrary limb darkening coefficient according to a linear limb darkening law. $q_2/q_1 < 1.72$ indicates solar-like differential rotation, $q_2/q_1 > 1.83$ can be due to anti solar-like differential rotation or a polar spot.

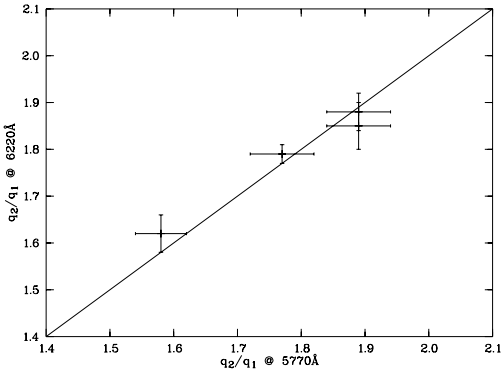

Fig. 9. Comparison of the measured values of q_2/q_1 for the four stars observed in two different wavelength regions between 5770 – 5810 Å and 6225 – 6270 Å for that q_2/q_1 could be measured. Within the observational errors the results from different wavelength regions are consistent with each other.

agreement within the error bars is obtained. A comparison to values of $v \sin i$ from the literature (Bernacca & Perinotto 1970–1973; Fekel 1997; Groot et al. 1996; Saar & Osten 1997; Uesugi & Fukuda 1982) is plotted in Fig. 7. 30 of our sample stars were not mentioned in one of those catalogues and are plotted at $v \sin i_{\rm Lit.} = -2\,{\rm km\,s^{-1}}$ for readability.

28 stars from the 30, for that no rotational velocities were known to us, have values of $v \sin i$ lower than $10\,{\rm km\,s^{-1}}$ and are thus not suited for a differential rotation analysis with FTM. Additionally most objects for which upper limits at about $10\,{\rm km\,s^{-1}}$ are cited in the literature turned out to have significantly lower values of $v \sin i$. In summary we have an overall number of 80 stars with $v \sin i < 10\,{\rm km\,s^{-1}}$ in our sample. For these stars no values of the differential rotation parameter α can be measured.

5. Evidence for differential rotation

Our data quality turned out to be adequate to push the noise down to a level sufficient to measure the second zero of the Fourier transform, q_2, on stars faster than $v \sin i = 12\,{\rm km^{-1}}$. Four stars fall in the region $10\,{\rm km\,s^{-1}} \leq v \sin i < 12\,{\rm km\,s^{-1}}$; 84 stars of our sample had too small a value of $v \sin i$ for a determination of differential rotation with FTM. Of the remaining stars five objects showed strong peculiarities (all five are binaries) and for them no mean profile could be derived with PLSD. 21 stars were sorted out due to asymmetries found after mirroring. Thus the ratio q_2/q_1 could be determined in 32 of the investigated 142 stars.

The 26 stars rotating faster than $v \sin i = 12\,{\rm km^{-1}}$ but not suited for FTM are given in Table 2. In column four we indicate if a mean profile was derived with PLSD, in column six we give a comment on the asymmetry. The comment "center" indicates that the mean profile has an asymmetric line core while the flanks appear symmetric, similar to the case shown in Fig. 4 (a), "flank" indicates that the flanks on the blue and the red side differ, similar

to the case shown in Fig. 4 (b). If no comment is given, the situation is similar to Fig. 3 (b), i.e., no specific signature of asymmetry is apparent.

Following Reiners & Schmitt (2002a), a ratio $q_2/q_1 < 1.72$ is a direct indication for solar-like differential rotation (equator faster than pole). $1.72 < q_2/q_1 < 1.83$ is typical for solid rotation with an arbitrary limb darkening parameter ϵ. A value of $q_2/q_1 > 1.83$ indicates anti solar-like differential rotation (pole faster than rotator) or a polar spot (Reiners & Schmitt 2002b).

The measured values of q_2/q_1 of the 32 stars are given in column seven of Table 3. In Fig. 8 the distribution of the measurements of q_2/q_1 among the 32 profiles is shown. The region consistent with rigid rotation of an unspotted star is indicated by dotted lines. The majority of our objects (20 of 32) lie within that region. Ten of the 32 objects show significant differential rotation with $q_2/q_1 < 1.72$, only two objects have $q_2/q_1 > 1.83$.

Four stars of the 32 were observed in both wavelength regions between $5770 - 5810$ Å and $6225 - 6270$ Å. The derived values of q_2/q_1 are compared in Fig. 9. For all four stars the derived values are compatible within the observational errors. Although both wavelength regions are relatively close to each other, this results demonstrates that the derived values of q_2/q_1 are not due to an effect specific for the utilized absorption lines but to an underlying universal line broadening.

For three stars, HD 89449, HD 121370 and HD 173667, we find extremely low values of q_2/q_1, and the strong deviation to the profiles expected from a rigid rotator can easily be seen even in the data domain. In Fig. 10 the profiles are shown in Fourier and data domain; in the left panels of Fig. 10 the Fourier transform of the broadening profiles derived with PLSD are shown with their error bars. Note that the second zero q_2 is visible in all cases. With dashed lines we overplotted the Fourier transform of a rigid rotator with the same value of $v \sin i$, $\epsilon = 0.6$ and a radial-tangential macroturbulence of $v_{\rm RT} = 4\,{\rm km\,s^{-1}}$. Note that we did not optimize the profile of the rigidly rotating case, nor did we determine values of turbulent velocities for the differential case. The amplitude of the Fourier transform depends on a variety of parameters and all photospheric velocities influence it. We think that it is always possible to find suitable values that produce the general slope of the Fourier transform. Differences in amplitude do not indicate bad fit quality.

On the other hand, the zeroes of a Fourier transform and especially the ratio q_2/q_1 is not affected by the "common" velocity fields and also limb darkening has only a limited effect (cf. Reiners & Schmitt 2002a). Differential rotation is the only known mechanism that can cause for ratios of $q_2/q_1 < 1.72$. Such small ratios are apparent in the three left plots of Fig. 10 and are in obvious contrast to the ratios of the rigid cases.

In the right column of Fig. 10 we plot the same cases in data domain. Note that directly the data, not the derived broadening profiles are shown. Over the error bars of the data we plotted as a solid line the convolutions of our derived templates with the derived broadening profiles. The consistency of the result of the convolution and the data is remarkable.

Even with the error bars of the spectra, that are quite large compared to that of the broadening profiles derived from the complete region of ~ 40 Å, the deviations of the rigidly rotating cases to the data are obvious. Again, it is not the incompatibilty in the wings or in the core that rules out rigid rotation, it is the overall shape of the profiles and especially the steepness of the flanks on both sides of the line. Such shapes cannot be induced by strong limb darkening ϵ or large turbulent velocities. In Figs. 10 (b, d, f) the effects of differential rotation are directly evident in the spectra.

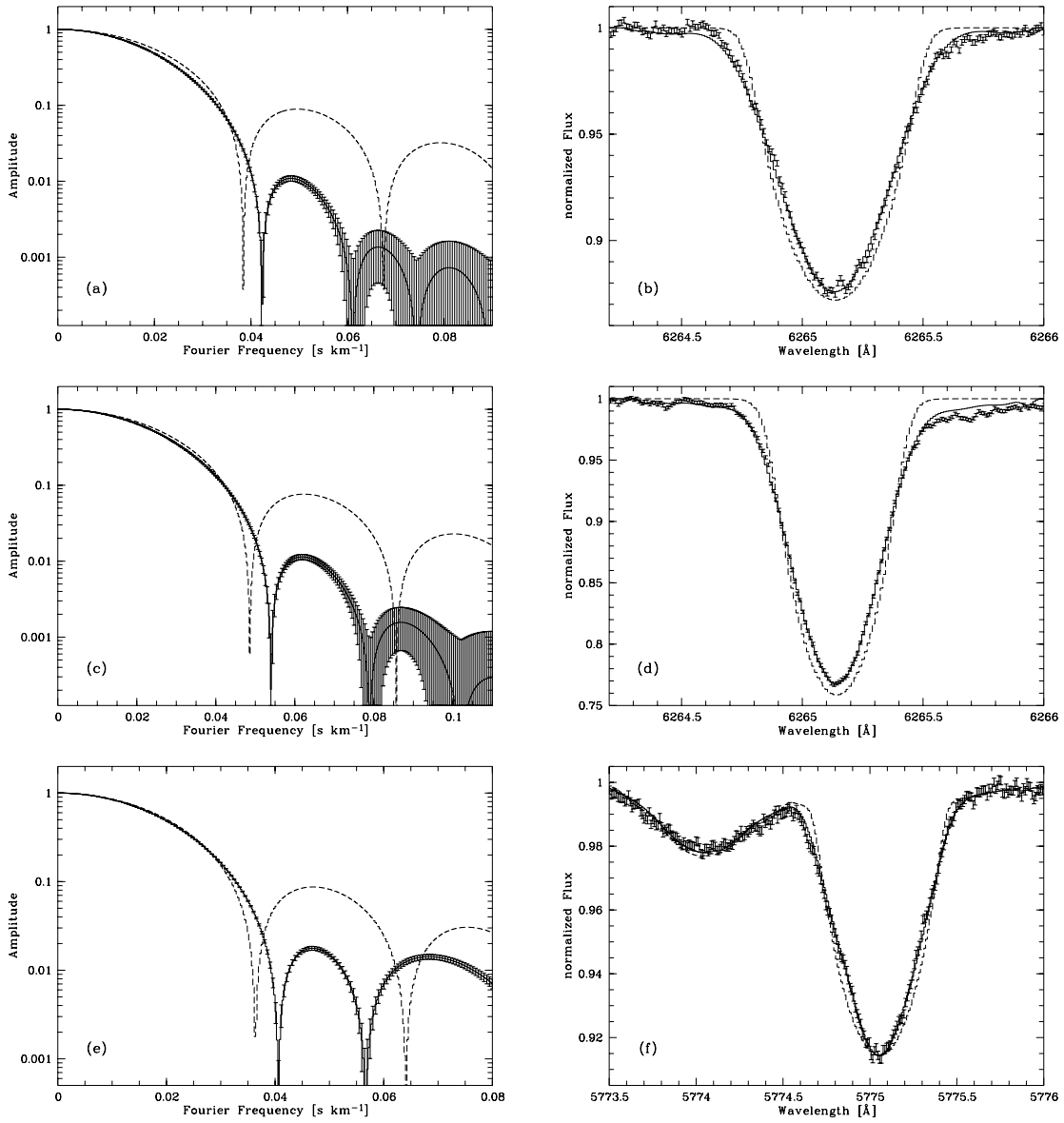

Fig. 10. Fourier spectra and small wavelength regions of the three stars with $q_2/q_1 < 1.5$. Left column: Fourier transforms of the broadening profiles derived with PLSD and their error bars. Right column: The original data plotted as error bars, overplotted with the results of the convolution of the appropriate template with the overall broadening profile (solid line, the Fourier transform of that profile is given in the left column). (a) and (b): HD 89 449, $q_2/q_1 = 1.44 \pm 0.04$; (c) and (d): HD 121 370, $q_2/q_1 = 1.46 \pm 0.03$; (e) and (f): HD 173 667, $q_2/q_1 = 1.40 \pm 0.02$. For comparison broadening profiles of rigid rotators are overplotted with dashed lines. The same values of $v \sin i$ as obtained for the individual stars are chosen, radial-rangential turbulence velocity of $v_{\rm RT} = 4\,{\rm km\,s^{-1}}$ and a linear limb darkening parameter of $\epsilon = 0.6$ are applied. Note that no optimization of the rigidly rotating case with, e.g., turbulence or limb darkening has been attempted (see text).

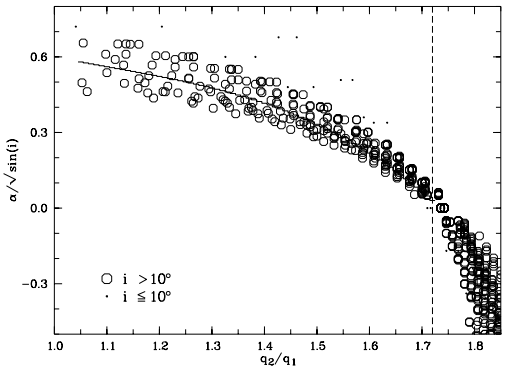

Fig. 11. Data points from our simulations; each point represents a calculated model. Differential rotation α and inclination angle i are given, and the ratio q_2/q_1 is measured from the simulated spectrum. For inclination angles $i > 10°$ the ratio $\alpha/\sqrt{\sin i}$ depends monotonically on q_2/q_1. The solid line represents Eq. (5), the dashed line is at $q_2/q_1 = 1.72$, the smallest ratio consistent with rigid rotation.

6. Deriving α

The more physical parameter to describe a star's differential rotation is the relative shear $\alpha = \Delta\Omega/\Omega_0$. Given the rotational period we can thus also obtain $\Delta\Omega$ from α, a value often assumed to be constant for differentially rotating stars with different rotational velocities. We already noted that a measured ratio of $q_2/q_1 < 1.72$ indicates differential rotation with the equator faster than the pole. In this section we show a direct connection between α and q_2/q_1.

In our simulations of line profiles from differentially rotating stars we calculated the ratios q_2/q_1 determined from the spectral lines of stars with given α in the range $-0.5 \le \alpha \le 1.0$ and $v \sin i = 10\,\mathrm{km\,s^{-1}}$ observed under an inclination angle i in the range $5° \le i \le 90°$ in steps of 5°. As shown in Fig. 6 of Reiners & Schmitt (2002a), the ratio q_2/q_1 depends nonlinearly on both α and i, thus it is only possible to derive a combined value of α and i from an observed ratio q_2/q_1.

In Fig. 11 we plot the ratio $\alpha/\sqrt{\sin i}$ vs. q_2/q_1 obtained from our simulations. Open circles mark data points with an inclination $i > 10°$, dots represent values from stars seen under an inclination angle i of 5° or 10°. Obviously, the ratio $\alpha/\sqrt{\sin i}$ is a good description of what is contained in the observable q_2/q_1 for inclination angles $i > 10°$. The probability to observe a star under an inlination $i \le 10°$ is $\sim 1.5\%$, on the other hand, for $i = 10°$ the projected rotational velocity becomes $0.17v$ and stars with $v \sin i > 10\,\mathrm{km\,s^{-1}}$ must have equatorial velocities of $v \gtrsim 60\,\mathrm{km\,s^{-1}}$. Therefore, in our sample of 32 stars we do not expect to have more than one of those cases and neglect possible inclinations $i \le 10°$ in the following.

Again, ratios of $1.72 < q_2/q_1 < 1.83$ are consistent with rigid rotation while $q_2/q_1 < 1.72$ indicates solar like differential rotation; the dashed line in Fig. 11 marks $q_2/q_1 = 1.72$. In the region $q_2/q_1 < 1.72$ the dependence of $\alpha/\sqrt{\sin i}$ on q_2/q_1 can be approximated by the polynomial

$$\frac{\alpha}{\sqrt{\sin i}} = 2.74 - 5.16x + 4.32x^2 - 1.30x^3, \quad x = \frac{q_2}{q_1}. \qquad (5)$$

Eq. (5) is shown with a solid line in Fig. 11. Maximum deviations around Eq. (5) are of the order of $\Delta(\alpha/\sqrt{\sin i}) = 0.1$ at $q_2/q_1 = 1.2$ and $\Delta(\alpha/\sqrt{\sin i}) = 0.05$ at $q_2/q_1 = 1.65$. The values of $\alpha/\sqrt{\sin i}$ derived from Eq. 5 are shown in column nine of Table 3. The uncertainty in $\alpha/\sqrt{\sin i}$ given in column ten of Table 3 is the combined error from the uncertainty $\delta\, q_2/q_1$ and the scatter in the $\alpha/\sqrt{\sin i}(q_2/q_1)$-relation in Eq. (5).

Ratios of $q_2/q_1 > 1.83$ can be due to anti-solar like differential rotation but are more likely due to a polar spot (cf. Reiners & Schmitt 2002b), thus we do not propose differential rotation for them. In the region $q_2/q_1 > 1.83$ the simulated data points can be fitted by

$$\frac{\alpha}{\sqrt{\sin i}} = 6.41 - 3.71x, \quad x = \frac{q_2}{q_1}. \qquad (6)$$

For $q_2/q_1 > 1.72$ we assign $\alpha = 0.0$ for the reasons mentioned above but give the largest amount of differential rotation consistent with our measurements as uncertainty in column ten of Table 3. Negative values of $\Delta\ \alpha/\sqrt{\sin i}$ indicate that only anti-solar like differential rotation is – besides a polar spot – consistent with the measured value of q_2/q_1.

7. Results

The obtained values q_2/q_1 and $\alpha/\sqrt{\sin i}$ for the 32 stars, as well as parameters from the literature are presented in Table 3. Ten stars with significant evidence for solar-like differential rotation have been found.

$B-V$ colours are taken from the Bright Star Catalogue (Hoffleit & Warren 1991). Values M_V and $T_{\rm eff}$ are calculated from $uvby\beta$ photometry using the program UVBYBETA published by Moon (1985); data are from Hauck & Mermilliod (1998). For $T_{\rm eff}$ a new calibration by Napiwotzki et al. (1993) based on the grids of Moon & Dworetsky (1985) was used, the statistical error of the temperature determination is about $\Delta T_{\rm eff} = 150\,\mathrm{K}$. Distances are derived from the Hipparcos parallaxes (ESA 1997). Sources for lithium abundances $\log\epsilon$(Li) are given in Table 3, upper boundaries of $\log\epsilon$(Li) are marked. The values of Ca II H and K emission $\log R'_{\rm HK}$ are calculated from the parameter $< S >$ from Baliunas et al. (1995) using the calibration given in Noyes et al. (1984). X-ray data are taken from Hünsch et al. (1998, 1999) except for HD 89 449.

To normalize the X-ray luminosity L_X to the bolometric luminosity $L_{\rm bol}$, the latter is calculated from M_V using the bolometric correction $B.C.$ given in Reed (1998), that is an empirical fit to the data given in Lang (1992). The bolometric correction was also used for the stellar radii; R is calculated from $M_{\rm bol}$ and $T_{\rm eff}$ with the calibration given in Cox (2000).

Table 3. Parameters for the 32 stars q_2/q_1 was derived for

HD	M_V[a]	$T_{\rm eff}$[a]	d[b][pc]	R[c] [$R_\odot$]	$P/\sin i$ [d]	$\frac{q_2}{q_1}$	$\delta\frac{q_2}{q_1}$	$\frac{\alpha}{\sqrt{\sin i}}$	$\delta\frac{\alpha}{\sqrt{\sin i}}$	$\log\epsilon$(Li)	$\log R'_{\rm HK}$[i]	$\log\frac{L_X}{L_{\rm bol}}$[j]
4089	2.75	6161	40.7	2.33	5.0	1.82	0.02	0.00	-0.42			-5.10
4247	3.08	6825	27.8	1.60	1.9	1.77	0.04	0.00	0.05			-5.08
17206	3.68	6371	14.0	1.40	2.8	1.70	0.02	0.07	0.08			-4.87
18256	2.93	6332	35.4	2.01	5.9	1.71	0.04	0.05	0.11	< 2.03[e]	-4.75	-5.66
22001	2.98	6601	21.4	1.80	6.9	1.83	0.07	0.00	-0.02			-5.98
23754	2.98	6518	17.9	1.84	6.8	1.87	0.05	0.00	-0.71			-6.91
25457	4.07	6333	19.2	1.19	3.3	1.71	0.02	0.05	0.08	2.95[h]		-4.15
25621	2.26	6091	34.6	2.99	9.1	1.73	0.03	0.00	0.11	3.01[e]		-5.11
30652	3.59	6408	8.0	1.44	4.2	1.78	0.03	0.00	0.01		-4.65	-5.06
35296	4.11	6060	14.7	1.29	4.1	1.75	0.02	0.00	0.05	2.87[h]	-4.38	-4.45
43386	3.50	6512	19.6	1.45	3.8	1.83	0.03	0.00	-0.49		-4.56	-5.06
70958	3.53	6230	27.2	1.58	1.7	1.75	0.01	0.00	0.03			-4.41
81997	3.28	6471	17.1	1.63	2.7	1.73	0.01	0.00	0.07	< 2.10[d]	-4.62	-5.06
89449	3.05	6398	21.2	1.86	5.4	1.44	0.04	0.39	0.11	< 1.10[d]	-4.77	-5.47[k]
89569	3.10	6290	35.8	1.89	7.8	1.57	0.02	0.26	0.09			-5.14
100563	3.61	6489	26.6	1.39	5.2	1.67	0.04	0.12	0.11	2.66[f]	-4.68	-4.95
105452	2.98	6839	14.8	1.67	3.6	1.59	0.02	0.23	0.09			-4.96
114378	3.82	6324	14.3	1.34	3.4	1.76	0.01	0.00	0.01		-4.53	-4.65
116568	3.20	6485	30.1	1.68	2.3	1.73	0.01	0.00	0.07			-5.27
120136	3.38	6437	15.6	1.58	5.1	1.57	0.04	0.26	0.11	< 0.60[g]	-4.75	-5.21
121370	2.36	6024	11.3	2.93	11.0	1.46	0.03	0.37	0.10	< 1.81[e]		-6.56
122066	2.18	6395	57.4	2.78	3.5	1.81	0.01	0.00	-0.34	2.50[e]		-5.04
124850	2.85	6075	21.4	2.29	7.7	1.91	0.04	0.00	-0.82	< 1.21[d]	-4.67	-4.77
136359	3.02	6296	41.7	1.95	4.9	1.78	0.01	0.00	-0.23	< 1.72[e]		-4.95
160915	3.58	6356	17.5	1.48	6.0	1.60	0.03	0.22	0.10	2.26[f]		
173667	2.78	6363	19.1	2.13	6.0	1.40	0.02	0.42	0.10	< 1.37[e]	-4.73	-5.32
175317	3.11	6563	32.0	1.71	5.1	1.58	0.04	0.24	0.11	< 0.46[e]		-5.39
197692	3.33	6587	14.7	1.53	1.9	1.62	0.02	0.19	0.08	< 1.18[f]		-5.09
199260	4.18	6213	21.0	1.18	4.4	1.79	0.03	0.00	-0.01			-4.68
210302	3.52	6465	18.7	1.46	5.4	1.72	0.04	0.03	0.11	2.67[e]		
213845	3.35	6551	22.7	1.54	2.2	1.71	0.02	0.05	0.08			-5.11
219693	2.82	6461	34.6	2.02	5.1	1.81	0.01	0.00	-0.34	2.50[e]		-5.41

[a] calculated from $uvby\beta$ photometry (see text), data from Hauck & Mermilliod (1998)
[b] parallax from ESA (1997)
[c] calculated from $T_{\rm eff}$ and $M_{\rm bol}$ with the calibration given in Cox (2000)
[d] Cutispoto et al. (2002)
[e] Balachandran (1990)
[f] Boesgaard & Tripicco (1986)
[g] Boesgaard & Lavery (1986)
[h] Chen et al. (2001)
[i] Baliunas et al. (1995), calibration from Noyes et al. (1984)
[j] Hünsch et al. (1998, 1999) except [k]
[k] *ROSAT* PSPC

7.1. Rotational velocities and periods in the HR-diagram

All (presumably single) stars of our primary sample are plotted in an HR-diagram in Fig. 12 (a). Stars with values of $v\,\sin i > 12\,{\rm km\,s^{-1}}$ are shown with full circles, stars with $v\,\sin i \le 12\,{\rm km\,s^{-1}}$ with open circles. The zero age main sequence (ZAMS) and evolutionary tracks for 1.2, 1.4 and $1.6\,M_\odot$ from Siess et al. (2000) are overplotted; the models with solar composition including overshooting were chosen. A drop of rotational velocity is apparent somewhere around spectral type F7 or 6200 K. This drop is well documented in many works (for a summary, cf. Gray 1988). As mentioned above, for measuring differential rotation data quality limits us to stars with projected rotational velocities larger than $12\,{\rm km\,s^{-1}}$, that is in our sample to stars of spectral type earlier than G1.

We derived rotational periods $P/\sin i$ for our sample stars from the measured values of $v\,\sin i$ and radii derived from $uvby\beta$-photometry. The different periods are plotted using different symbol sizes in the HR-D in Fig. 12 (b); larger symbols indicate longer rotational periods. The dis-

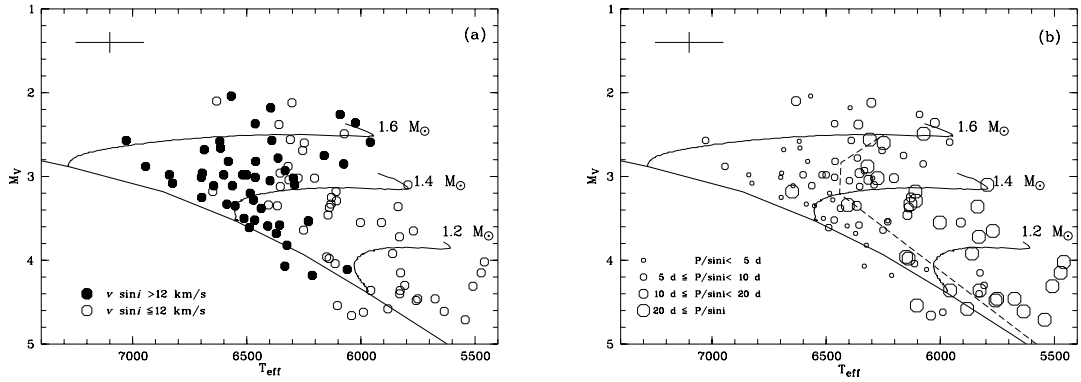

Fig. 12. HR-diagram of our sample stars. Absolute visual magnitudes $M_{\rm V}$ and effective temperatures $T_{\rm eff}$ are calculated from $uvby\beta$-photometry (see text). Typical error bars are given in the upper left corner, the zero age main sequence (ZAMS) and evolutionary tracks for 1.2, 1.4 and 1.6 $M_\odot$ from Siess et al. (2000) are overplotted. (a): Stars with $v \sin i > 12\,{\rm km\,s^{-1}}$ are plotted with full circles, slower rotators with open circles. (b) Rotational periods; larger symbols indicate longer rotational periods.

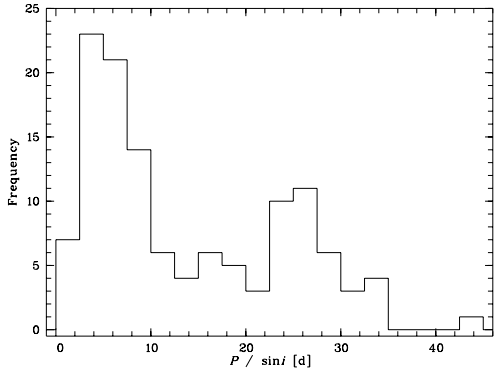

Fig. 13. Distribution of rotational periods $P/\sin i$ derived from the projected rotational velocities $v \sin i$ and stellar radii in our primary sample.

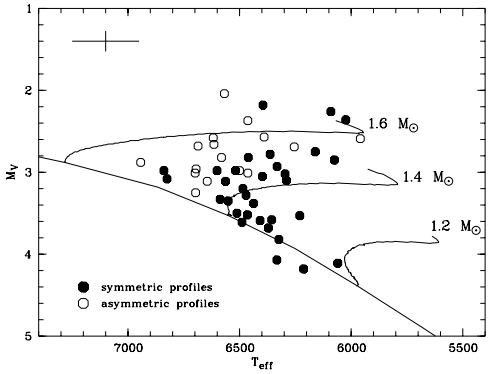

Fig. 14. HR-diagram as in Fig. 12. Only stars with $v \sin i > 12\,{\rm km\,s^{-1}}$ are plotted; stars with symmetric profiles as full circles, those with asymmetric profiles with open circles.

tribution of $P/\sin i$ in our sample is shown in Fig. 13. Some indication for a bimodal period distribution may be found. In Fig. 12 (b) we overplotted the isochrone at 2 Gyr according to Siess et al. (2000). Dividing our sample into groups of stars younger and older than 2 Gyr we find that 22 out of 52 "young" stars have rotational periods of $P/\sin i < 5$ d (42%), while only 3 out of 49 "old" stars (6%) fall into this group. Thus we find that a correlation between age in the HR-D and the projected rotational period $P/\sin i$ – as expected from rotational braking – is significant on a 4σ-level.

7.2. Profile symmetry of the fast rotators

In Fig. 14 we plot in an HR-diagram the 32 objects for that differential rotation was derived (filled circles) together with the stars that were discarded due to asymmetries in the spectral lines (open circles). The stars with asymmetric profiles tend to have higher masses and populate the upper left region of the HR-D, while the stars with symmetric profiles have lower masses and lie in the lower right part of the HR-D. The region populated by the stars with asymmetric profiles is directly neighboured to the "granulation boundary" found by Gray (1991). He found that stars above that boundary show asymmetries in the profiles an order of magnitude larger than those found in spectral lines of stars below the boundary. Thus it is not surprising that many single stars in that region show asymmetric profiles. Although the reason for the onset of larger asymmetries in that region is not well known, it appears that the 21 discarded stars are not randomly distributed in the HR-D, but that the profile asymmetries seem to be of physical origin.

The 32 stars with symmetric broadening profiles are the objects we can examine in our search for differential rotation. This subsample consists of stars of spectral type F0

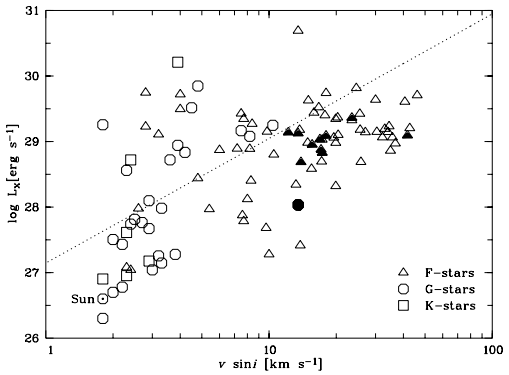

Fig. 15. X-ray luminosities L_X from *ROSAT* vs. our values of $v \sin i$ for all stars of our sample. Different spectral types are indicated by different symbols, filled symbols represent stars with evidence for solar like differential rotation. The least squares fit to *Einstein* data of stars from F7 to M5, given in Pallavicini et al. (1981), is overplotted.

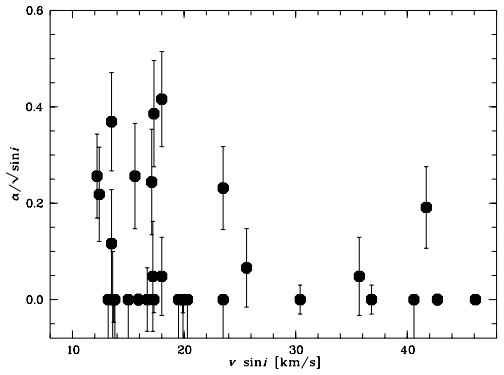

Fig. 16. Derived values of $\alpha/\sqrt{\sin i}$ vs. $v \sin i$ for the 32 of our sample stars where measurement of differential rotation was possible. Stars for that a ratio of q_2/q_1 is measured are interpreted as rigid rotators ($\alpha = 0.0$), possible anti-solar like differential rotation is ($\alpha < 0.0$) indicated by the error bars.

– G0 and effective temperatures between 6000 and 6900 K. From the evolutionary tracks in Fig. 14 we find that their masses cluster between 1.2 and 1.6 $M_\odot$ and that stars of widely varying ages are in the sample.

Of the 21 stars with asymmetric broadening profiles, twelve (60%) have values of $v \sin i > 20\,\mathrm{km\,s^{-1}}$, while that is only the case for 11 of the 32 stars (34%) with symmetric profiles. While this is not surprising since the rotational velocities of stars of earlier spectral types tend to have higher rotational velocities, we remark that sorting out stars with asymmetric profiles for the most part neglects the faster rotators. Thus a statistical interpretation of the velocity dependence of stellar parameters has to be carried out with great care.

7.3. Rotation and X-ray emission

The X-ray luminosities L_X observed with the *ROSAT* satellite are plotted against the values of $v \sin i$ for our sample stars. Different spectral types are indicated by different symbols, the stars with evidence for solar-like differential rotation are plotted with filled symbols. In agreement with Pallavicini et al. (1981), F-stars show only a weak correlation between X-ray luminosity and equatorial rotational velocity. Our sample of later spectral type stars, however, does not follow the correlation derived there. We overplotted their correlation between L_X and $v \sin i$ as dotted line in Fig. 15. Although our data do not necessarily contradict their correlation, the scatter among the stars later than G0 is substantially higher than in Fig. 5 of Pallavicini et al. (1981). Nevertheless, we confirm the existence of a velocity dependent lower envelope of X-ray luminosities at about an order of magniude lower than described by the correlation given in Pallavicini et al. (1981).

7.4. Differential rotation and $v \sin i$

In Fig. 16 we plot the amount of differential rotation $\alpha/\sqrt{\sin i}$ vs. the projected rotational velocity $v \sin i$ of the 32 stars where a measurement of differential rotation was possible. As pointed out in Sect. 6, rigid rotation is proposed for the stars with ratios of $q_2/q_1 \geq 1.72$. However, since anti-solar like differential rotation is consistent with larger ratios of q_2/q_1, some of the objects have large error bars in the direction of negative α. Stronger differential rotation appears to be more common in the slowly rotating stars (41% of the rigid rotators have values of $v \sin i > 20\,\mathrm{km\,s^{-1}}$ while that is the case for only 20% of the differentially rotating stars), but we might have sorted out specifically the differentially rotating stars while neglecting the stars with asymmetric broadening profiles. Evidence for differential rotation is also found on stars with higher rotational velocities. We find no upper boundary in $v \sin i$ for the onset of differential rotation.

In Fig. 17 (a) we show the 32 stars in an HR-D with symbols characterizing their rotational velocity and differential rotation. Triangles represent stars with $v \sin i > 15\,\mathrm{km\,s^{-1}}$, circles represent slower ones. Filled symbols stand for differential rotators while rigid rotators are shown with open symbols. In four cases we find positive values of $\alpha/\sqrt{\sin i}$ but with errors larger than the actual values of $\alpha/\sqrt{\sin i}$. These objects are marked with bold triangles to indicate that rigid rotation cannot be excluded for these stars.

Differential rotators are distributed over the whole region populated by our sample stars and no preferred region is apparent neither for differential nor for solid rotators. No correlation between (i) differential rotation and mass, and (ii) differential rotation and age is found.

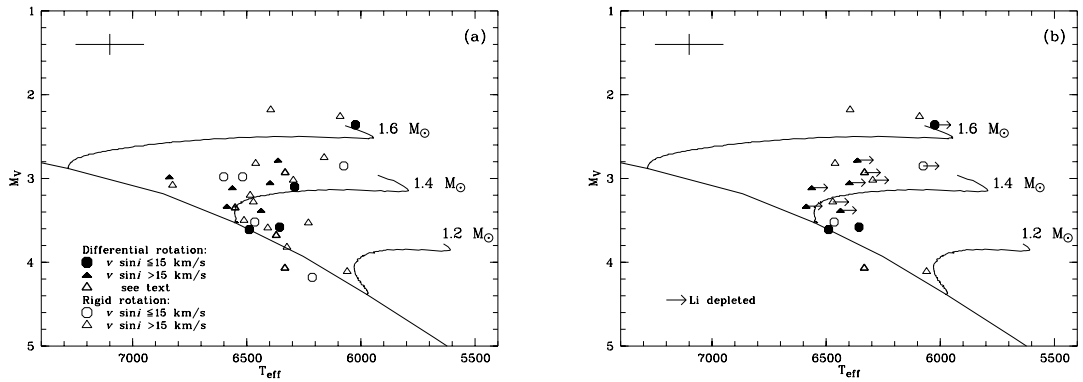

Fig. 17. H-R diagram of (a) the 32 stars with measured values of q_2/q_1. Slow rotation ($v \sin i < 15\,\mathrm{km\,s^{-1}}$) is indicated by circles, fast rotation by triangles. Full and open symbols represent stars with and without significant evidence for differential rotation, respectively. Four fast rotators with measured values of $\alpha/\sqrt{\sin i} > 0.0$ but error bars consistent with rigid rotation are symbolized with bold triangles; (b) same as (a) but only objects with available data on Li abundances are shown. "Li depletion" ($\log \epsilon\,(\mathrm{Li}) \leq 2.2$) is indicated by a right arrow while all other stars have $\log \epsilon\,(\mathrm{Li}) > 2.2$.

7.5. Li abundances

The correlation between differential rotation and Li abundances was studied by Reiners & Schmitt (2002d). They showed that for stars with projected rotational velocities $v \sin i > 15\,\mathrm{km\,s^{-1}}$ a correlation between Li abundace and evidence for differential rotation exists. Specifically, among the fast rotators ($v \sin i > 15\,\mathrm{km\,s^{-1}}$), the differentially rotating stars tend to be Li-depleted, while a large spread in Li abundance can be found among the rigidly rotating stars. The Li abundances of slow rotators are generally more spread out and differential rotation as well as Li-depletion seem to be more common in slowly rotating stars.

In Fig. 17 (b) the stars with measured differential rotation, for which Li abundances are available, are plotted in the same way as in Fig. 17 (a). Here we interpret stars for which no Li was detected and only an upper limit exists as Li-depleted, these objects are marked with a right arrow in Fig 17 (b). For objects without right arrows Li was detected, i.e., $\log \epsilon\,(\mathrm{Li}) > 2.2$ in our sample. In Fig. 17 (b) it is obvious that fast differentially rotating Li-depleted stars are not specifically evolved. Even some fast rigid rotators are at least of comparable age if not older. We think that Li-depletion in these relatively young stars is presumably a consequence of mixing processes connected with differential rotation (cp. Balachandran 1990).

7.6. Differential rotation and activity

In Fig. 18 we plot the dependence of differential rotation on the two most important indicators of stellar activity; Fig. 18 (a) shows the value of $\alpha/\sqrt{\sin i}$ vs. the chromospheric emission from Ca II H and K lines in terms of $\log R'_{\mathrm{HK}}$ (cf. Noyes et al. 1984), Fig. 18 (b) shows $\alpha/\sqrt{\sin i}$ vs. the X-ray luminosity normalized to the bolometric luminosity $\log L_{\mathrm{X}}/L_{\mathrm{bol}}$. In both figures we indicate available measurements of the Li abundance with different symbols. Full circles represent stars where Li measurements provide only upper limits; these stars are Li-depleted. Open circles stand for "Li rich" stars and an asterisk indicates that no Li measurement is available to our knowledge.

In Fig. 18 (a) a trend is apparent; while no differential rotation is found for stars with a value of $\log R'_{\mathrm{HK}} > -4.65$, $\alpha/\sqrt{\sin i} > 0$ is consistent with our results for all stars in the region $-4.8 < \log R'_{\mathrm{HK}} < -4.65$. No measurements for stars less active that $\log R'_{\mathrm{HK}} = -4.8$ are available in our sample. A similar trend appears in the dependence of $\alpha/\sqrt{\sin i}$ on $\log L_{\mathrm{X}}/L_{\mathrm{bol}}$ in Fig. 18 (b); while over the whole interval of X-ray luminosities rigid rotators are present, for a subgroup of stars in the region $-5.6 < \log L_{\mathrm{X}}/L_{\mathrm{bol}} < -4.6$, $\alpha/\sqrt{\sin i}$ may depend on the normalized X-ray flux.

Our data indicates that especially the chromospherically most active stars tend to be rigid rotators. Henry et al. (1996) place a transition region between active and incative stars at $\log R'_{\mathrm{HK}} = -4.75$. These authors believe that stars spend a third of their lifetime in the active stage and remain inactive after crossing the transition region. Our results are severely limited by the extent of coinciding measurements of differential rotation and activity indicators, and in particular nothing can be said about the rotation law of stars with $\log R'_{\mathrm{HK}} < -4.8$. Although the results from our small sample remain preliminary, stars in the active phase seem to be rigid rotators while those in the transition region do show evidence for differential rotation. On the basis of our data we cannot yet decide whether differential rotation is a property only of the inactive stars belonging to the transition region, or whether it is just a reflection of the properties of our sample.

What makes this even more interesting is the dependence of the ratio $\log(\omega_{\mathrm{cyc}}/\Omega)$ on $\log R'_{\mathrm{HK}}$, with ω_{cyc} de-

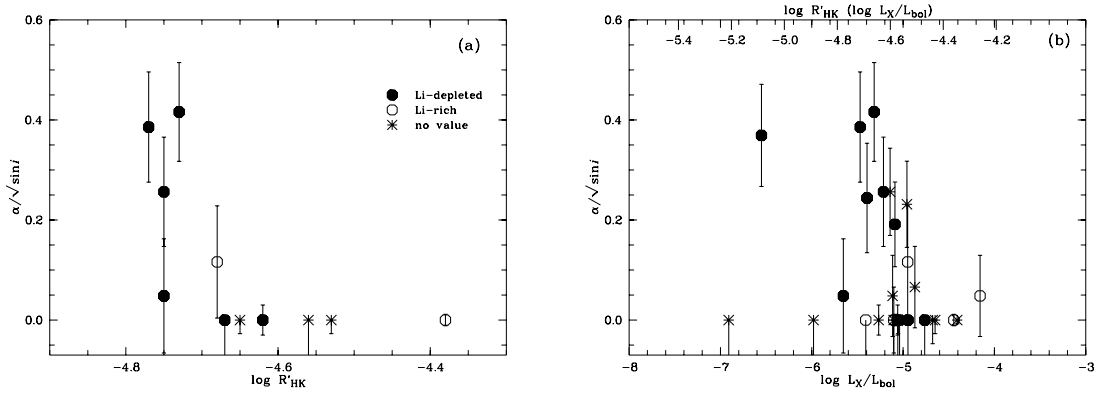

Fig. 18. Differential rotation in terms of $\alpha/\sqrt{\sin i}$ vs. activity indicators. (a) Chromospheric Ca II H and K emission $\log R'_{\rm HK}$; (b) X-ray luminosity $L_{\rm X}$ normalized to bolometric luminosity $L_{\rm bol}$. Available values of Li abundances are indicated with symbols. At the top panel of (b), $\log R'_{\rm HK}$ calculated from $\log L_{\rm X}/L_{\rm bol}$ according to the calibration of Sterzik & Schmitt (1997) is marked.

noting the dynamo cycle frequency and Ω the rotational frequency. Brandenburg et al. (1998) found two distinct branches of active and inactive stars in their Fig. 2 with a jump between them at values of $\log R'_{\rm HK} \simeq -4.75$. Our measurements favour the onset of differential rotation in the transition region, but, again, no statement is possible about the dominating group of inactive stars from the $\log R'_{\rm HK}$ values of our sample.

A possible way to overcome this problem is to search for similar regions in the X-ray data. Sterzik & Schmitt (1997) found a linear correlation between the chromospherically emission in terms of $\log R'_{\rm HK}$ and X-ray to bolometric luminosity $\log L_{\rm X}/L_{\rm bol}$. Naturally the scatter in such relations is quite large since values of $\log R'_{\rm HK}$ are mean values measured over years while $\log L_{\rm X}/L_{\rm bol}$ mostly comes from a snapshot. Nevertheless, according to the relation found by Sterzik & Schmitt (1997) the transition region at $\log R'_{\rm HK} \simeq -4.75$ should be found at $\log L_{\rm X}/L_{\rm bol} \simeq -5.6$. However, no indication for a similar transition in the values of $L_{\rm X}/L_{\rm bol}$ was actually apparent in their data.

In Fig. 18 (b) it appears that the region where differential rotation in our sample sets in, does not show up at a value of $\log L_{\rm X}/L_{\rm bol} \simeq -5.6$, but at around $\log L_{\rm X}/L_{\rm bol} \simeq -5.2$. At the top panel of Fig. 18 (b) we have indicated the values of $\log R'_{\rm HK}(\log L_{\rm X}/L_{\rm bol})$, i.e., the values of chromospheric activity derived from the X-ray to bolometric luminosity following the relation given in Sterzik & Schmitt (1997). Reading Fig. 18 (b) as a $\alpha/\sqrt{\sin i}$ vs. $\log R'_{\rm HK}$ plot a comparison to Fig. 18 (a) reveals a similar overall picture but with an offset in the direction of $\log R'_{\rm HK}$. It remains unclear whether the $\log R'_{\rm HK} - \log L_{\rm X}/L_{\rm bol}$ relation is systematically shifted for our subgroup of stars (e.g., differential rotators or stars in the transition region) or whether the offset simply is an effect due to our limited sample and the intrinsic scatter of the X-ray snapshots.

To conclude, the correlations of $\alpha/\sqrt{\sin i}$ to both activity indicators, $\log R'_{\rm HK}$ and $\log L_{\rm X}/L_{\rm bol}$, in our sample reveal a clustering of differential rotators in a relatively well defined stage of activity. Whether this clustering reflects the onset of differential rotation during a star's transfer from an active to an inactive stage cannot be answered from our sample.

7.7. $\Delta\Omega$ and ΔP

In this subsection we will investigate the dependence of the often used parameters $\Delta\Omega$ and ΔP on Ω and P, respectively. Given the radius R from their positions in the HR-D (Cox 2000), $\Delta\Omega$ and ΔP can easily be calculated from $\alpha = \Delta\Omega/\Omega$ and $P = 2\pi/\Omega$. We focus on the stars with significant evidence for differential rotation, i.e., we assume that a threshold divides the differential from the rigid rotation regime. Although we do not know what triggers the onset of differential rotation, we search for dependences only among the stars with significant evidence for differential rotation.

It is important to note that the uncertainties in the values of α inherent in FTM do not allow to detect differential rotation of the amount $\alpha \lesssim 10\%$ independent of the value of $v \sin i$. Thus we are not able to detect differential rotation rates as low as claimed for example from Doppler images for the K0 dwarf AB Dor ($\alpha = \Delta\Omega/\Omega \simeq 4.6\,10^{-3}$, Donati & Collier Cameron 1997). Simulations of the angular velocity dependence of differential rotation were carried out for a G2 and a K5 dwarf by Kitchatinov & Rüdiger (1999). Motivated by results from observational works they searched for a power law dependence of the form

$$\frac{\Delta\Omega}{\Omega} \propto \Omega^{-n'}. \qquad (7)$$

Kitchatinov & Rüdiger (1999) found that n' is not a constant but varies in the region $0.95 \lesssim n' \lesssim 1.56$ with a

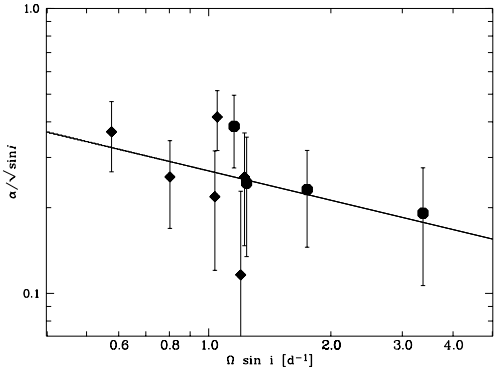

Fig. 19. Differential rotation $\alpha/\sqrt{\sin i}$ vs. angular velocity $\Omega \sin i$. Stars of later type ($B-V > 0.46$) are plotted with squares, early types with values of $B-V \leq 0.46$ with circles. The result of a formal regression analysis is plotted over the data.

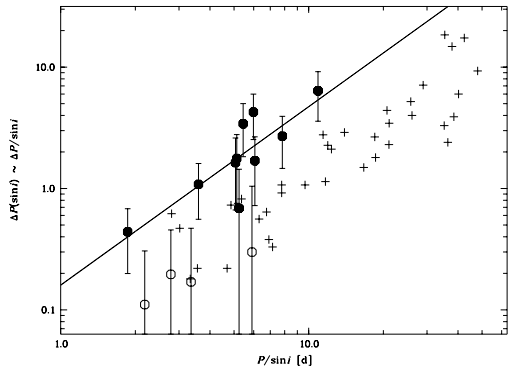

Fig. 20. Values of $\Delta P(\sin i) \simeq \Delta P/\sin i$ derived from Eq. (10) vs. $P/\sin i$ for the stars of our sample that show differential rotation. Open circles represent stars that are consistent with rigid rotation. The solid line is a fit to the values from stars not consistent with rigid rotation (full circles). Crosses represent data from Donahue et al. (1996).

mean value of $n' = 1.15$ for G2. Furthermore they show that the amount of α is significantly larger for the spectral type G2 than for K5 while the dependence on angular velocity is comparable for both spectral types. No simulations for F-stars were carried out but it seems not implausible to assume that for F-stars a similar angular velocity dependence remains valid.

Our values of $\alpha = \Delta\Omega/\Omega$ that are significantly larger than 0.0, i.e., $\alpha - \delta\alpha > 0.0$, are plotted against $\Omega \sin i$ in Fig. 19. A rough decrease in α with increasing $\Omega \sin i$ is apparent, although the scatter is quite large. A formal regression analysis to Eq. (7) yields

$$\frac{1}{\sqrt{\sin i}} \cdot \frac{\Delta\Omega}{\Omega} = (0.27 \pm 0.03)\,(\Omega \sin i)^{-0.34\pm0.26}. \quad (8)$$

Obviously, although the errors of the regression curve are large, our derived $n' = 0.34 \pm 0.26$ is inconsistent with the values predicted by Kitchatinov & Rüdiger (1999). As already pointed out in that work, such disagreement may be partly due to our sample's combined different spectral types. The highest angular velocities are mainly found for early F-stars (circles in Fig. 19), the lowest ones on late F-stars (squares in Fig. 19). Since models suggest that later spectral types have lower differential rotation rates, combining different spectral types would indeed reduce the slope n'.

The observational results Kitchatinov & Rüdiger (1999) compared their model to were derived from the chromosperic Ca II H and K lines. Donahue et al. (1996) search for differential rotation by measuring variations in seasonal rotational periods; assuming that active regions migrate over the stellar surface in analogy to the solar case, acceleration towards the equator would diminish the length of the rotational period during a stellar cycle. Donahue et al. (1996) searched for a period dependent range ΔP in the observed period of the form

$$\Delta P \propto P^{n''} \quad (9)$$

and found $\Delta P \propto < P >^{1.3\pm0.1}$. The authors point out that in analogy to the solar case active regions may not reach over all latitudes and the observed period change may reflect only a part of the period variation; thus absolute values of ΔP may in fact be higher. However, assuming comparable latitudes of activity for different spectral types, the value of $n'' = 1.3 \pm 0.1$ should be valid independent of the absolute values of ΔP.

For a direct comparison we derived values of ΔP for the stars of our sample using the equation

$$\Delta P = P\frac{\alpha}{1-\alpha}. \quad (10)$$

Since we measured only $v \sin i$ instead of the pure rotational velocity v, we only have the measured values $\alpha/\sqrt{\sin i}$ and $P/\sin i$ instead of α and P. The inclination dependence of $\Delta P(\sin i)$ is a bit more complicated. Evaluating Eq. (10) with the measured quantities including $v \sin i$, we obtain

$$\begin{aligned}\Delta P(\sin i) &= \frac{P}{\sin i}\frac{\alpha}{\sqrt{\sin i}(1-\frac{\alpha}{\sqrt{\sin i}})} \\ &= \frac{P}{\sin i}\frac{\alpha}{\sqrt{\sin i}-\alpha}.\end{aligned}$$

For sufficiently large inclination angles we approximate

$$\frac{\alpha}{\sqrt{\sin i}-\alpha} \simeq \frac{\alpha}{1-\alpha} \quad (11)$$

and are thus led to plot our measurements of $\Delta P(\sin i)$ vs. $P/\sin i$ in Fig. 20 (full circles). For comparison we overplotted the values of ΔP from Ca II H and K lines given in Donahue et al. (1996) (crosses). The open circles represent four of our measurements that are consistent with solid rotation but have a value of $\alpha > 0.0$. Regression analysis for the significant measurements of differential

rotation (excluding the four values consistent with rigid rotation) yields

$$\Delta\frac{P}{\sin i} = 10^{(-0.80\pm0.26)}\left(\frac{P}{\sin i}\right)^{(1.47\pm0.35)}. \quad (12)$$

Thus we found in our sample a value of $n'' = 1.47 \pm 0.35$ in very good agreement with $n'' = 1.3 \pm 0.1$ derived by Donahue et al. (1996). This agreement describes what is apparent in Fig. 20; although there is an offset between our data and that from Ca II H and K lines, the slopes of both datasets are comparable.

As mentioned above, the values of ΔP measured by period variations in Ca II H and K lines must be interpreted as lower limits since the differential character can be obtained only along the active latitudes. Let us assume that the offset between our values of ΔP and the values from Donahue et al. (1996) is due to the limited sensitivity in latitude of the photometric method. Let us further assume that active regions appear and migrate in analogy to the solar case and that the stellar rotational law is solar-like and of the form $\Omega(l) = \Omega_0(1 - \alpha\sin^2 l)$ with l being the latitude. Then we can estimate the highest latitudes where stellar active regions appear in the early phase of a stellar magnetic cycle (or where they induce photometric signatures in Ca II H and K). This highest latitude $l_{\max}$ can be calculated from

$$\sin^2 l_{\max} = \frac{\Omega}{X(\Omega - \Delta\Omega) + \Delta\Omega} \quad (13)$$

with the measured ratio of

$$X = \frac{\Delta P_{\text{this work}}}{\Delta P_{\text{Donahue et al.}}} = 2.7^{+2.3}_{-1.5}$$

and Eq. (8). For $\Omega > 0.5\,\mathrm{d}^{-1}$, Eq. (13) depends only slightly on the value of Ω. Neglecting possible inclination angles of $i < 90°$ in Eq. (8), we derive for all $\Omega > 0.5\,\mathrm{d}^{-1}$ a maximum latitude where active regions emerge on the stellar surfaces of

$$l_{\max} = (40^{+30}_{-10})°,$$

a value in surprisingly good agreement with the active regions from the Sun.

We want to emphasize that the interpretation of the offset between data from chromosheric Ca II H and K period variations and from our FTM analysis is somewhat speculative and that many uncertainties arise during the different derivations. Even some simplifications in our regression analysis, e.g., neglecting the stars with $\alpha = 0.0$, lack physical motivations and need further investigation by the examination of more objects. Nevertheless, the coincidence of the derived maximum active latitudes $l_{\max}$ with the solar case is an encouraging result that points towards a possible connection between differential rotation measurements from photometry and FTM.

To be complete we calculated the lap times $2\pi/\Delta\Omega$, i.e., the time the equatorial regions need to lap the pole. We plot them vs. the rotational period $P/\sin i$ in Fig. 21.

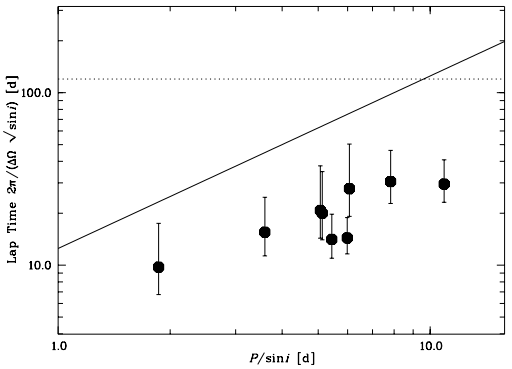

Fig. 21. Lap time $2\pi/(\Delta\Omega\sqrt{\sin i})$ plotted against $P/\sin i$. The solar value of $2\pi/\Delta\Omega \simeq 130$ d is indicated with a dashed line. Due to the limited sensitivity of FTM, lap times of that order can only be detected for the slowest rotators. The period dependent maximum value of the detectable lap time is shown with a solid line.

$2\pi/\Delta\Omega$ is often used as an indicator for dynamo efficieny. Results from Doppler imaging suggest that $2\pi/\Delta\Omega$ is a constant for stars of different rotational periods and close to the solar value of 130 d, e.g., ~ 110 d for AB Dor (Donati & Collier Cameron 1997).

The dotted line in Fig. 21 indicates the solar value of $2\pi/\Delta\Omega \simeq 130$ d. Our measured values from the stars with detected differential rotation are significantly lower than that value. We note again that with FTM detections of differential rotation imply $\alpha \gtrsim 10\%$; since $2\pi/\Delta\Omega = P/\alpha$, we are limited to a period dependent value of the maximum lap time that can be detected with FTM. That maximum lap time is indicated as a solid line in Fig. 21. Although we can thus neither confirm nor disprove the occurence of differential rotators with lap times similar to the solar value we actually found some stars with evidence for significantly lower values of $2\pi/\Delta\Omega$.

8. Summary

We measured the projected rotational velocities $v \sin i$ for a sample of 142 F-, G- and K-stars. For 32 stars of our sample the amount of differential rotation $\alpha = (\Omega_{\text{Equator}} - \Omega_{\text{Pole}})/\Omega_{\text{Equator}}$ has been derived. We demonstrated our technique with that overall broadening profiles with extremely high signal-to-noise ratios can be obtained and correlated our results with stellar parameters from the literature. The conclusions of our paper can be summarized as follows:

1. The distributions of the rotational velocities and the line profile asymmetries of our sample stars are in agreement with expectations from the rotation and granulation boundary in the HR-diagram.
2. Evidence for differential rotation has been obtained for stars between 12 and 45 $\mathrm{km\,s^{-1}}$. Although differential

rotation is more common in slowly rotating stars, no upper limit in $v \sin i$ is found for the occurence of differential rotation.

3. We found no correlations between differential rotation α and (i) mass or (ii) age. Fast rotating Li-depleted stars with evidence for differential rotation show no indication of high age. The interpretation that Li-depletion in fast rotators is connected with internal mixing is supported.
4. Some indications exist that differential rotation is not a common phenomenon in very active stars with $\log R'_{\rm HK} > -4.65$. While we have no data for inactive stars with $R'_{\rm HK} < -4.85$, stars populating the presumed transition region between an active and an inactive phase at $\log R'_{\rm HK} \approx -4.75$ show strong evidence for differential rotation.
5. Our data suggest a period dependence of differential rotation of the form $\Delta P/P = P^{(0.47\pm0.35)}$. Assuming that differences to results from CaII emission measurements are due to the limited sensitivity latitude of that data, we derive a maximum latitude for active regions in good agreement with the solar value.
6. Although using FTM we could not measure lap times $2\pi/\Delta\Omega$ of the order of the solar value of ~ 130 d, we found evidence for lap times significantly lower than that value. This finding contradicts the assumption that comparable lap times – maintaining comparable dynamo efficiencies – should be found on different stars.

Acknowledgements. A.R. acknowledges financial support from Deutsche Forschungsgemeinschaft DFG-SCHM 1032/10-1.

References

Barnes J.R., Collier Cameron A., James D.J., and Donati J.-F., 2000, MNRAS 314, 162
Balachandran S., 1990, ApJ, 354, 310
Baliunas S.L., et al., 1995, ApJ, 438, 269
Bernacca P.L., and Perinotto M., 1970–1973, Contrib. Oss. Asiago Nos., 239, 250, 294
Boesgaard A.M., and Tripicco M.J., 1986, ApJ, 303, 724
Boesgaard A.M., and Lavery R.J., 1986, ApJ, 309, 770
Brandenburg A., Saar S.H., and Turpin C.R., 1998, ApJ, 498, L51
Chen Y.Q., Nissen P.E., Benoni T., 2001, and Zhao. G., A&A, 371, 943
Cox A.N., ed., 2000, Allen's Astrophysical Quantities, AIP Press, Springer Verlag, New York
Cutispoto G., Pastori L., de Medeiros J.R., Tagliaferri G., and Andersen J., 2002, A&A, 384, 491
Donahue R.A., Saar S.H., and Baliunas S.L., 1996, ApJ, 466, 384
Donati J.-F., Cameron A., 1997, MNRAS, 291, 1
Dravins D., Lindegren L., Torkelsson U., 1990, A&A, 237, 137
ESA, 1997, The Hipparcos and Tycho Catalogues, ESA SP-1200
Fekel F.C., 1997, PASP, 109, 514
Groot P.J., Piters A.J.M., and van Paradijs J., 1996, A&AS, 118, 545
Gray D.F., 1973, ApJ, 184, 161
Gray D.F., 1977, ApJ, 211, 198
Gray D.F., 1982, ApJ, 258, 201
Gray D.F., 1988, Lectures on spectral-line analysis: F, G and K stars, The Publisher, Arva
Gray D.F., 1991, Dynamo action in evolved stars. In: Tuominen I., Moss D., Rüdiger G. (eds.), IAU Coll. 130, The Sun and Cool Stars: Activity, Magnetism, Dynamos. Springer, Berlin, p.336
Hall, D.S., 1991, in The Sun and Cool stars, activity, magnetism, dynamos, eds. I. Tuominen, D. Moss, and G. Rüdiger, Springer Verlag, New York, p.353
Hauck B., Mermilliod M., 1998, A&AS, 129, 431
Henry T.J., Soderblom D.R., Donahue R.A., and Baliunas S.L, 1996, ApJ, 111, 439
Hoffleit E.D., and Warren Jr. W.H., 1991, The Bright Star Catalogue, 5th Revised Ed.
Hünsch M., Schmitt J.H.M.M., and Voges W., 1998, A&AS, 132, 155
Hünsch M., Schmitt J.H.M.M., Sterzik M.F., and Voges W., 1998, A&AS, 135, 319
Kitchatinov L.L., and Rüdiger G., 1999, A&A, 344, 911
Kupka F., Piskunov N.E., Ryabchikova T.A., Stempels H.C., Weiss W.W., 1999, A&AS 138, 119
Lang, K.R., 1992, Astrophysical Data: Planets and Stars, Springer-Verlag Berlin Heidelberg New York
Moon T.T., 1985, Coom. Univ. London Obs. 78
Moon T.T., Dworetsky M.M., 1985, MNRAS, 217, 305
Napiwotzki R., Schönberger D., and Wenske V., 1993, A&A, 268, 653
Noyes R.W., Hartmann L.W., Baliunas S.L., Duncan D.K., and Vaughan A.H., 1984, ApJ, 279, 763
Pallavicini R., Golub L., Rosner R., Vaiana G.S., Ayres T., and Linsky J.L., ApJ, 248, 279
Reed B.C., 1998, J. R. Astron. Soc. Can., 92, 36
Reiners A., Schmitt J.H.M.M., Kürster M., 2001, A&A 376, L13
Reiners A., and Schmitt J.H.M.M., 2002a, A&A, 384, 555
Reiners A., and Schmitt J.H.M.M., 2002b, A&A, 388, 1120
Reiners A., and Schmitt J.H.M.M., 2002c, AN, in press
Reiners A., and Schmitt J.H.M.M., 2002d, A&A 393, L77
Saar S.H., and Osten R.A., 1997, MNRAS, 284, 803
Siess L., Dufour E., and Forestini M., 2000, A&A, 358, 593
Sterzik M.F., and Schmitt J.H.M.M., 1997, AJ, 114, 167
Uesugi A., and Fukuda I., 1982, Revised Catalogue of Rotational Velocities, Department of Astronomy, Kyito Univ., Japan
Wöhl H., 1983, in Solar and Stellar Magnetic Fields: Origin and Coronal Effects, ed. J.O. Stenflo, IAU Symp. 102, Reidel Dordrecht, p. 155

Appendix A: Table of projected rotational velocities

Table A.1. Projected rotational velocites of our sample stars.

HD	HR	Name	$B-V$[a]	$v \sin i$ [km s^{-1}]	$\Delta\, v \sin i$ [km s^{-1}]
		Sun	0.62	< 2.1	0.2
693	33	6 Cet	0.48	3.8	0.8
739	35	θ Scl	0.45	< 2.4	1.2
1581	77	ζ Tuc	0.57	< 2.3	0.4
2151	98	β Hyi	0.61	3.3	0.3
2726	120		0.36	13.5	1.5
3302	147	λ^2 Phe	0.46	17.8	0.8
4089	187	ρ Tuc	0.51	23.5	0.4
4247	197		0.35	42.7	0.4
4813	235	$19\,\phi^2$ Cet	0.51	< 2.6	0.8
8556	404		0.40	25.8	0.8
10700	509	$52\,\tau$ Cet	0.72	< 1.8	0.1
10800	512		0.62	< 1.8	0.6
13445	637		0.81	2.3	0.2
13555	646	$17\,\eta$ Ari	0.45	3.8	1.0
15798	740	$76\,\sigma$ Cet	0.45	4.6	0.8
16417	772	λ^2 For	0.65	< 2.5	0.1
16620	781	$83\,\epsilon$ Cet	0.44	4.8	0.6
16920	802	ζ Hor	0.41	4.0	0.6
17051	810	ι Hor	0.56	4.2	0.6
17206	818	$1\,\tau^1$ Eri	0.48	25.6	0.3
18256	869	$46\,\rho^3$ Ari	0.47	17.2	0.3
20010	963	α For	0.54	4.0	0.7
20766	1006	ζ^1 Ret	0.64	< 2.7	0.1
20794	1008		0.71	< 2.0	0.1
20807	1010	ζ^2 Ret	0.60	2.7	0.3
22001	1083	κ Ret	0.41	13.2	0.3
23249	1136	$23\,\delta$ Eri	0.91	< 2.3	0.5
23754	1173	$27\,\tau^6$ Eri	0.43	13.8	0.3
25457	1249		0.51	18.0	0.3
25570	1254		0.37	34.5	1.0
25621	1257		0.50	16.7	0.1
27442	1355	ϵ Ret	1.07	2.9	0.3
30652	1543	$1\,\pi^3$ Ori	0.48	17.3	0.2
33093	1665		0.60	4.7	0.2
33256	1673	68 Eri	0.45	9.7	1.0
35296	1780	111 Tau	0.54	15.9	0.1
38393	1983	$13\,\gamma$ Lep	0.48	7.7	0.3
39587	2047	$54\,\chi^1$ Ori	0.59	8.2	0.1
40136	2085	$16\,\eta$ Lep	0.33	15.5	0.3
43386	2241	74 Ori	0.43	19.5	0.4
57095			0.97	< 2.4	0.1
57749	2811		0.35	40.0	1.0
58728	2846	63 Gem	0.45	30.0	1.0
60532	2906		0.52	5.3	0.5
64096	3064	9 Pup	0.60	6.4	0.1
64235	3072		0.41	< 2.8	1.3
65907	3138		0.57	< 2.4	0.3
67228	3176	$10\,\mu^2$ Cnc	0.64	3.7	0.3
68255	3210	$16\,\zeta^2$ Cnc	0.53	3.6	0.1
68456	3220		0.43	9.8	0.6
70958	3297	1 Hya	0.47	46.1	0.2
72673	3384		0.78	2.7	0.1
73752	3430		0.72	3.3	0.1
76932	3578		0.52	2.6	0.4
80586	3709	27 Hya	0.91	4.8	0.4
81809	3750		0.64	2.9	0.3
81997	3759	$31\,\tau^1$ Hya	0.41	30.4	0.3
87783	3976		0.88	4.0	0.1
89449	4054	40 Leo	0.45	17.3	1.7

Table A.1. continued

HD	HR	Name	$B-V$[a]	$v \sin i$ [km s^{-1}]	$\Delta\, v \sin i$ [km s^{-1}]
89569	4061		0.48	12.2	0.7
91324	4134		0.50	8.0	0.2
91889	4158		0.52	3.3	0.7
94388	4251		0.48	6.0	1.5
98991	4395	13 λ Crt	0.43	17.2	1.0
99028	4399	78 ι Leo	0.42	10.5	0.3
99285	4408	81 Leo	0.39	34.1	0.6
100286	4443		0.54	8.0	0.2
100563	4455	89 Leo	0.48	13.5	0.4
102928	4544		1.05	3.5	0.4
104827	4602	2 Com	0.24	46.0	1.5
105452	4623	1 α Crv	0.33	23.5	1.2
109409	4788		0.68	3.0	0.5
110379	4825	29 γ Vir	0.36	25.5	1.0
112164	4903		0.63	3.0	0.5
113848	4946	39 Com	0.39	27.0	1.5
114378	4968	42 α Com	0.45	19.9	0.1
114642	4981	53 Vir	0.46	12.0	0.4
114971	4996		1.06	< 2.5	0.1
115383	5011	59 Vir	0.58	4.5	0.3
115617	5019	61 Vir	0.70	< 2.2	0.3
116568	5050	66 Vir	0.41	36.8	0.4
117176	5072	70 Vir	0.71	3.0	0.2
118646	5128		0.43	33.0	1.0
120136	5185	4 τ Boo	0.50	15.6	1.0
121370	5235	8 η Boo	0.58	13.5	1.3
121416	5239		1.14	< 2.5	0.3
122066	5257	48 Hya	0.48	40.6	0.6
123999	5304	12 Boo	0.54	15.0	1.0
124850	5338	99 ι Vir	0.51	15.0	0.6
125276	5356		0.51	2.8	0.4
128898	5463	α Cir	0.25	14.0	1.0
130819	5530	8 α^1 Lib	0.40	3.2	0.5
131156	5544	37 ξ Boo	0.72	3.9	0.3
136351	5698	ν^1 Lup	0.51	< 2.8	0.2
136352	5699	ν^2 Lup	0.63	3.1	0.2
136359	5700		0.48	20.3	0.3
137052	5723	31 ϵ Lib	0.45	8.3	0.3
138716	5777	37 Lib	1.00	< 2.0	0.2
139211	5803		0.50	5.0	0.2
141004	5868	27 λ Ser	0.60	2.9	0.5
141767	5891	κ TrA	1.10	7.7	1.0
142860	5933	41 γ Ser	0.47	10.0	1.3
143333	5954	49 Lib	0.51	8.2	0.2
144069	5977	ξ Sco	0.46	16.9	1.5
147675	6102	γ Aps	0.92	3.9	0.2
151769	6243	20 Oph	0.47	7.7	0.9
153363	6310	26 Oph	0.40	35.0	1.0
155555			0.79	31.5	0.5
156897	6445	40 ξ Oph	0.39	19.9	0.7
157950	6493		0.38	7.2	0.5
160032	6569	λ Ara	0.41	13.9	0.9
160691	6585	μ Ara	0.69	3.8	0.2
160910	6594		0.38	32.2	0.4
160915	6595	58 Oph	0.46	12.4	0.5
164764	6733	69 τ Oph	0.41	8.4	1.7
165185	6748		0.61	7.5	0.3
165499	6761	ι Pav	0.59	< 2.5	0.1
173667	7061	110 Her	0.48	18.0	2.0
175317	7126		0.44	17.1	0.7

Table A.1. continued

HD	HR	Name	$B-V$[a]	$v \sin i$ [km s^{-1}]	$\Delta\, v \sin i$ [km s^{-1}]
175986	7161		0.55	10.4	0.2
176303	7172	11 Aql	0.57	24.6	0.7
177474	7226	γ CrA	0.52	7.6	0.2
186185	7496		0.46	14.9	1.5
186203	7497	47 χ Aql	0.57	3.6	0.3
188512	7602	60 β Aql	0.85	< 2.3	0.3
190248	7665	δ Pav	0.75	3.2	0.2
191408	7703		0.86	< 1.8	0.2
197692	7936	16 ψ Cap	0.42	41.7	1.7
199260	8013		0.50	13.7	0.1
199684	8031		0.40	21.3	0.9
203608	8181	γ Pav	0.49	2.4	0.5
206301	8283	42 Cap	0.67	4.8	0.2
206860	8314		0.58	10.4	0.4
210302	8447	15 τ PsA	0.48	13.6	0.2
211415	8501		0.61	< 2.2	0.3
213845	8592	59 υ Aqr	0.44	35.7	0.6
215648	8665	46 ξ Peg	0.50	6.7	0.7
219482	8843		0.52	7.5	0.1
219693	8859	ϕ Gru	0.44	19.9	0.3
220729	8907	o Gru	0.40	20.4	0.3
222368	8969	17 ι Psc	0.50	5.4	0.2
224930	9088	85 Peg	0.69	< 2.0	0.3

[a] Hoffleit & Warren (1991)

Chapter 8

Summary and Outlook

8.1 Summary

The study on stellar rotation and differential rotation determined from line profiles was carried out in two steps; (i) the modelling of line profiles from differentially rotating stars in analogy to the solar case, and the question how stellar differential rotation can be determined from those. (ii) The observation and analysis of a large sample of F-, G-, and K-stars applying the studied methods.

Observational data are given in Sect. 7.1 in Tables 3 and A.1, the results of the modelling and from the observations can be summarized as follows:

For the modelling part (i)

1. The first two zeros of Fourier transformed absorption line profiles, q_1 and q_2, can be utilized for determining the amount of solar-like (the equator rotating faster than the pole) differential rotation in terms of the parameter α in Eq. (1.2).

2. The ratio q_2/q_1 is a well-defined, easily measurable tracer of solar-like differential rotation. Solar-like differential is the only known mechanism significantly diminishing the amount of q_2/q_1.

3. For the case of anti solar-like differential rotation, with the equator rotating slower than the polar regions, the amount of q_2/q_1 increases. The dependence on the value of α is only marginally. Thus the Fourier transform method is only slightly sensitive to anti solar-like differential rotation.

4. Using the Fourier transform method (FTM) turbulence velocity fields can be neglected on stars with projected rotational velocities of $v \sin i \geq 10\,\mathrm{km\,s^{-1}}$. For these stars the observed two zeros of the Fourier transformed profiles exclusively come from rotational broadening. In slower rotators zeros imprinted by turbulence broadening cannot safely be disentangled from the rotational zeros. No detection of differential rotation with FTM is possible in slower rotating stars.

5. Polar spots increase the value of q_2/q_1 similar to anti solar-like differential rotation. Anti solar-like differential rotation cannot unambigiously be detected, but using FTM it is also possible to search for signatures of polar spots on rigidly rotating stars.

6. Limb darkening always enlarges (or diminishes) all zero positions in a similar manner and only has a small influence on the value of q_2/q_1. Nevertheless, the uncertainty in limb darkening is one of the major error sources in the determination of differential rotation.

7. Asymmetric line profiles are likely dominated by stellar surface features (spots). Differential rotation should not be derived from them. In symmetric profiles starspots and active regions can mimick solar-like differential rotation only if arranged in some very special configurations. In most cases obvious signatures are visible in the spectra. The probability to mistake surface features as differential rotation in symmetric line profiles is extremely small.

For the observational part (ii)

1. The values of the differential rotation parameter α derived from a multi-parameter χ^2-fit modelling the stellar atmosphere of the F5 dwarf ψ Cap were compared to results obtained using FTM. Both analyses yielded identical results for the derived values of α. This consistency check confirmed the applicability of FTM and showed the redundancy of a complete atmospheric fit.

2. High resolution ($R \geq 220\,000$), high signal-to-noise ($S/N \geq 500$) spectra were taken for 142 field stars of spectral types F, G and K. Data quality allowed the determination of differential rotation on stars rotating faster than $v \sin i = 12\,\mathrm{km\,s^{-1}}$.

3. 84 stars have a value of $v \sin i$ that is below the threshold of $12\,\mathrm{km\,s^{-1}}$. In 21 stars with $v \sin i \geq$

$12\,\mathrm{km\,s^{-1}}$ the rotational broadening profile is dominated by stellar surface features or spectral binarity; the value of α could not be determined on these objects.

4. Differential rotation in terms of α was measured in 32 stars of spectral types F and G.

5. Significant evidence for solar-like differential rotation with $\alpha > 0$ was found in ten of the 32 stars.

6. The majority of the differentially rotating stars have projected rotational velocities less than $20\,\mathrm{km\,s^{-1}}$. Some stars with $\alpha > 0$ are rotating relatively fast with the fastest one having a value of $v \sin i = 42\,\mathrm{km\,s^{-1}}$.

7. Lap times of the order of 10 d – significantly less than the solar one – have been found. This contradicts the assumption that all differentially rotating solar-like stars harbour stellar dynamos with comparable lap times.

8. Evidence for a correlation between differential rotation and Li-depletion is apparent; differentially rotating stars with $\alpha > 0$ and values of $v \sin i > 15\,\mathrm{km\,s^{-1}}$ tend to be Li-depleted.

9. Dependencies of differential rotation on angular velocity or rotation period were derived; they are $\alpha \sim \Omega^{(-0.34\pm0.26)}$ or $\Delta P/P \sim P^{(0.47\pm0.35)}$, respectively. This is consistent with results from CaII H & K photometry.

10. Some indications for an onset of differential rotation at specific stages of activity exist. Significant correlations between differential rotation and further stellar parameters have not been found.

8.2 Outlook

With the potential of determining stellar differential rotation for larger samples of stars, a key ingredient of stellar magnetic dynamos becomes measurable. Thus the main ingredients believed to drive stellar magnetic activity are accessible and can be studied for stars of different masses and ages.

To derive a clear picture of the underlying physics searching for correlations between crucial parameters like activity, temperature dependence, magnetic braking etc., the sample studied during this work is too small. Among the main questions to be answered for a deeper understanding of what drives stellar activity are the following:

- How stricly holds the period dependence? Evidences for a period-dependent amount of differential rotation were found in the cited studies of Donahue et al. (1996) and in Hall (1991), in theoretical estimations (Kitchatinov & Rüdiger, 1999) and in this work. Some results are compatible but others are not. An attempt to explain the different results from this work and theory was explained in Sect. 7.1.7. To answer this question a sample with more stars of different spectral types must be taken into account.

- It is definitely expected that the amount of differential rotation depends on the depth of the convection zone and thus of spectral type. Temperature also scales with spectral type and affects the surface structure by itself. No temperature dependence could be found in this work, a study of a larger sample with more stars of various temperatures will certainly improve this situation.

- Is there a correlation between differential rotation and activity? Due to measurements of CaII H & K fluxes, cool stars are occasionally sorted into two groups of activity, divided by the rather historical "Vaughan-Preston gap" (Vaughan & Preston, 1980). Recent studies about rotation periods P_{rot} and magnetic cycle periods P_{cyc} suggest two distinct branches of the correlation between CaII index $\log R'_{\mathrm{HK}}$ and the ratio $P_{\mathrm{rot}}/P_{\mathrm{cyc}}$ for active and inactive stars (Brandenburg et al., 1998). An evolutionary jump between the two branches coincides with the Vaughan-Preston gap. In Sect. 7.1.7 an onset of differential rotation around this region might be indicated, but the amount of data available clearly is insufficient to draw a definite conclusion.

There is only one way to answer these questions: Observe more objects! With the telescopes and instruments used in this work, stars with apparent magnitudes of $m_{\mathrm{V}} < 7$ provide enough photons to reach the desired data quality in a reasonable amount of time, i.e., in less than an hour.

During two additional observing runs in February and April 2002, a total of 145 stars, most of them with rotational velocities of $v \sin i > 40\,\mathrm{km\,s^{-1}}$, were observed with the spectrographs FOCES at the DSAZ[1] and with FEROS at ESO[2]. Since the demands on data quality are less for slower rotating stars, determining the value of α should be possible for a large number of these relatively fast rotators. In Fig. 8.1 the distribution of stars

[1] Deutsch Spanisches Astronomiezentrum, Calar Alto, Spain
[2] European Southern Observatory, Chile

with given apparent magnitude m_V and rotational velocities of $v \sin i > 10\,\mathrm{km\,s^{-1}}$ as measured before this work are shown. The filled region indicates the sample of stars observed during the five observing runs granted to this project. Among the stars with known rotational velocities roughly 50% have been observed. In order to significantly improve the number of stars for which α can be measured, it is thus necessary to go to fainter stars. Achieving the required data quality for fainter stars is not yet feasible, but it may hopefully be a matter of time until larger telescopes and better instruments can provide the required data quality even for observations of much fainter stars.

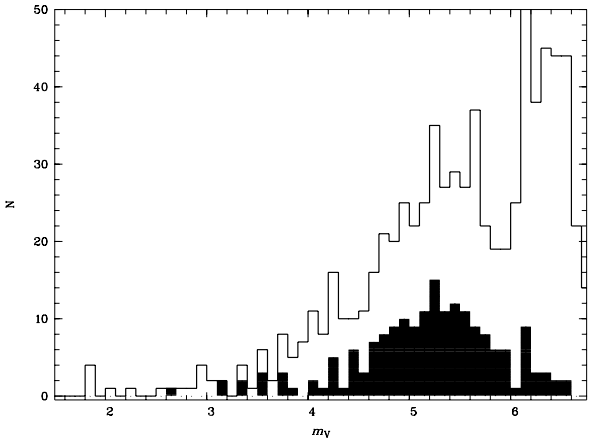

Figure 8.1: Distribution of stars with rotational velocities of $v \sin i > 10\,\mathrm{km\,s^{-1}}$ as measured before this work. The filled region indicates the sample of stars observed in this project.

There is one topic – mentioned in Chapter 6 – that can be adressed directly; it is the question of internal mixing in differential rotators. All "fast" rotators ($v \sin i > 15\,\mathrm{km\,s^{-1}}$) with available Li abundances and measured signatures of solar-like differential rotation appeared Li-depleted. In the studies mentioned in Chapter 6 the connection between Li abundance and rotational velocity is explained; the situation is shown in Fig. 8.2. Measured values of Li abundance $\log \epsilon$(Li) as given in the literature are plotted vs. the projected rotational velocity $v \sin i$ (values for stars not contained in our sample are from the literature, stars without known values of $v \sin i$ are plotted at $v \sin i = -2\,\mathrm{km\,s^{-1}}$). Stars for which only an upper limit in Li abundance was found are indicated with a downward arrow. Data according to stars with evidence for solar-like differential rotation as measured in this work are indicated by a red cross, those consistent with rigid rotation by a blue cross. It is apparent that among the slow rotators a large scatter in Li abundance occurs while fast rotators predominantly are Li rich. Only a handful of objects happen to fall below the dashed line indicating the lower envelope of the main scatter in Li abundance with rotation. It has been suggested by some authors that an internal mixing process – probably due to differential rotation – depletes Li at the stellar surface. This hypothesis is supported by the results of this work and is presented in Chapter 6; in terms of Fig. 8.2 it means that no blue cross lies below the dashed line. It would thus be most promising to determine the values of the differential rotation parameter α for stars with measured Li abundances below that threshold; if the hypothesis is correct, all those stars are expected to be differential rotators. Some of these objects have been observed during the FOCES and FEROS observing runs, and they are indicated with green circles in Fig. 8.2.

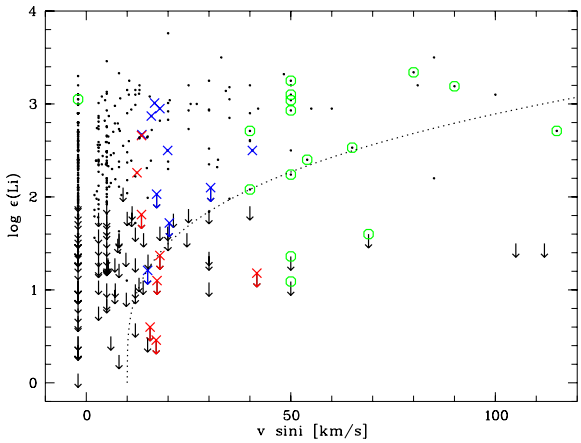

Figure 8.2: Li abundances $\log \epsilon$(Li) vs. $v \sin i$. Downward arrows indicate that Li abundances are only upper limits. Marked with red crosses are stars for which solar-like differential rotation was derived for in this study, blue crosses are for stars consistent with rigid rotation. Stars observed in a follow-up project with the instruments FOCES and FEROS are indicated with green circles.

The question of internal mixing may be answered by observations of stars we have Li abundances for. An additional parameter crucial for our understanding of stellar evolution is stellar age. Since no certain indicators for stellar ages do exist for field stars, it is often the position in the H-R diagram that is used to determine the age of a star. This method is rather imprecise and no homogenous sample of objects can be examined using field stars. One solution is to observe stars that are members of stellar clusters; all members of a cluster are believed to have formed under the same initial conditions and are of the same age representing a very homogenous sample. Modern instruments (mounted at large aperture telescopes) often supply multi-fibre spectrographs where many high-quality spectra can be obtained in a limited field – like a globular cluster – in only a single exposure. Observing samples of stars in a handful of different stellar cluster with varying ages, a

time-dependent study on differential rotation in stars of different spectral types but well-defined physical properties can be achieved. A study of the evolution of differential rotation with respect to other properties like rotational velocity and chromospheric activity may be possible with such a sample.

References

Brandenburg A., Saar S.H., and Turpin C.R., 1998, ApJ, 498, L51

Donahue R.A., Saar S.H., and Baliunas S.L., 1996, ApJ, 466, 384

Hall, D.S., 1991, in The Sun and Cool stars, activity, magnetism, dynamos, eds. I. Tuominen, D. Moss, and G. Rüdiger, Springer Verlag, New York, p.353

Kitchatinov L.L., and Rüdiger G., 1999, A&A, 344, 911

Vaughan A.H., and Preston G.W., 1980, PASP 92, 385

Acknowledgements

During the course of this work many individuals earned my deep thankfulness. For this I switch back to german.

An dieser Stelle soll allen gedankt sein, die diese Arbeit ermöglicht haben und die Zeit so angenehm werden liessen; dazu wechsle ich wieder ins Deutsche.

Dank sei gesagt:

- **Jürgen Harry Max Michael Schmitt**. Die ursprüngliche Idee zu dieser Arbeit kam natürlich von ihm, sein Stil seine Doktoranden zu betreuen, gab mir die Freiheit, mich zu entfalten und von seiner Erfahrung zu profitieren. Für kollegiale Zusammenarbeit und den wissenschaftlichen sowie persönlichen Rückhalt sei hier besonders gedankt.
- **Uwe Wolter, Marc Hempel** und **Thomas Berghöfer** für sehr fruchtbare und überaus angenehme Bürogemeinschaften, ihr Interesse an meiner Arbeit und vor allem für alles darüber hinaus.
- **Jan-Uwe Ness, Hans Hagen** und **Dieter Engels** für ihre wertvollen Hilfestellungen und jederzeit offene Ohren.
- Der ganzen **Arbeitsgruppe** für die angenehme und aufgeschlossene Atmosphäre und jede Menge hilfreicher Diskussionen.
- **Anette Reiners**, die meinen Reise- und Arbeitszeiten immer Verständnis entgegenbringt und es sogar spannend findet, wie sich die Sonne dreht. Und sowieso!
- Meinen **Eltern**, für ihre nach wie vor uneingeschränkte Unterstützung in allem.

Und natürlich danke ich der DFG für ihre Förderung unter der Nummer DFG-SCHM 1032/10-1.